UNIVERSITY OF MISKOLC
FACULTY OF MECHANICAL ENGINEERING AND INFORMATICS

INFLUENCE OF MANUFACTURING PARAMETERS ON PLA AND PLA–WOOD COMPOSITE MATERIALS: STATISTICAL, MACHINE LEARNING, AND BIOLOGICAL EVALUATION FOR BIOMEDICAL APPLICATIONS

PHD THESES

Prepared by

Md Mazedur Rahman
Engineering of … (BSc),
Engineering of … (MSc)

ISTVÁN SÁLYI DOCTORAL SCHOOL OF MECHANICAL ENGINEERING SCIENCES
TOPIC FIELD OF DESIGN OF MACHINES AND STRUCTURES
TOPIC GROUP OF PRODUCT DEVELOPMENT AND DESIGN

Head of Doctoral School

Dr. Gabriella Bognár
DSc, Full Professor

Head of Topic Group

Dr. Gabriella Bognár
Scientific Supervisor

Dr. SZÁVAI Szabolcs

Miskolc
2026

CONTENTS

SUPERVISOR'S RECOMMENDATIONS

Date

Supervisor

LIST OF SYMBOLS AND ABBREVIATIONS

SYMBOLS	
ABS	*Acrylonitrile Butadiene Styrene*
AM	*Additive Manufacturing*
ANOVA	*Analysis of Variance*
BCC	*Body-Centered Cubic*
CAD	*Computer-Aided Design*
CO_2	*Carbon Dioxide*
DOE	*Design of Experiments*
FCC	*Face-Centered Cubic*
FDM	*Fused Deposition Modeling*
FEM	*Finite Element Method*
FFF	*Fused Filament Fabrication*
MAE	*Mean Absolute Error*
ML	*Machine Learning*
MPa	*Machine Learning*
PLA	*Polylactic Acid*
RMSE	*Root Mean Squared Error*
RSM	*Response Surface Methodology*

SYMBOLS	
R^2	Coefficient of Determination
S/N	*Signal-to-Noise Ratio*
SC	*Simple Cubic*
SEM	*Scanning Electron Microscopy*
mg/mL	*Milligram per Milliliter*
µm	*Micrometer*

1. INTRODUCTION

Additive manufacturing (AM) is one of the most sustainable advanced manufacturing techniques, primarily depositing materials layer by layer to produce parts with improved characteristics such as better surface finish, lower manufacturing costs, reduced material waste, and desirable mechanical properties [1]. Therefore, this technique is currently adopted across multiple industries, including aerospace, construction, automotive, and biomedical sectors. [1].Moreover, the fabricated parts require a shorter manufacturing process compared to traditional or conventional manufacturing methods, including a wider scope for adopting various raw materials. In AM, additional benefits include the ability to produce intricate geometries, reduced carbon emissions, and potential energy savings[2].

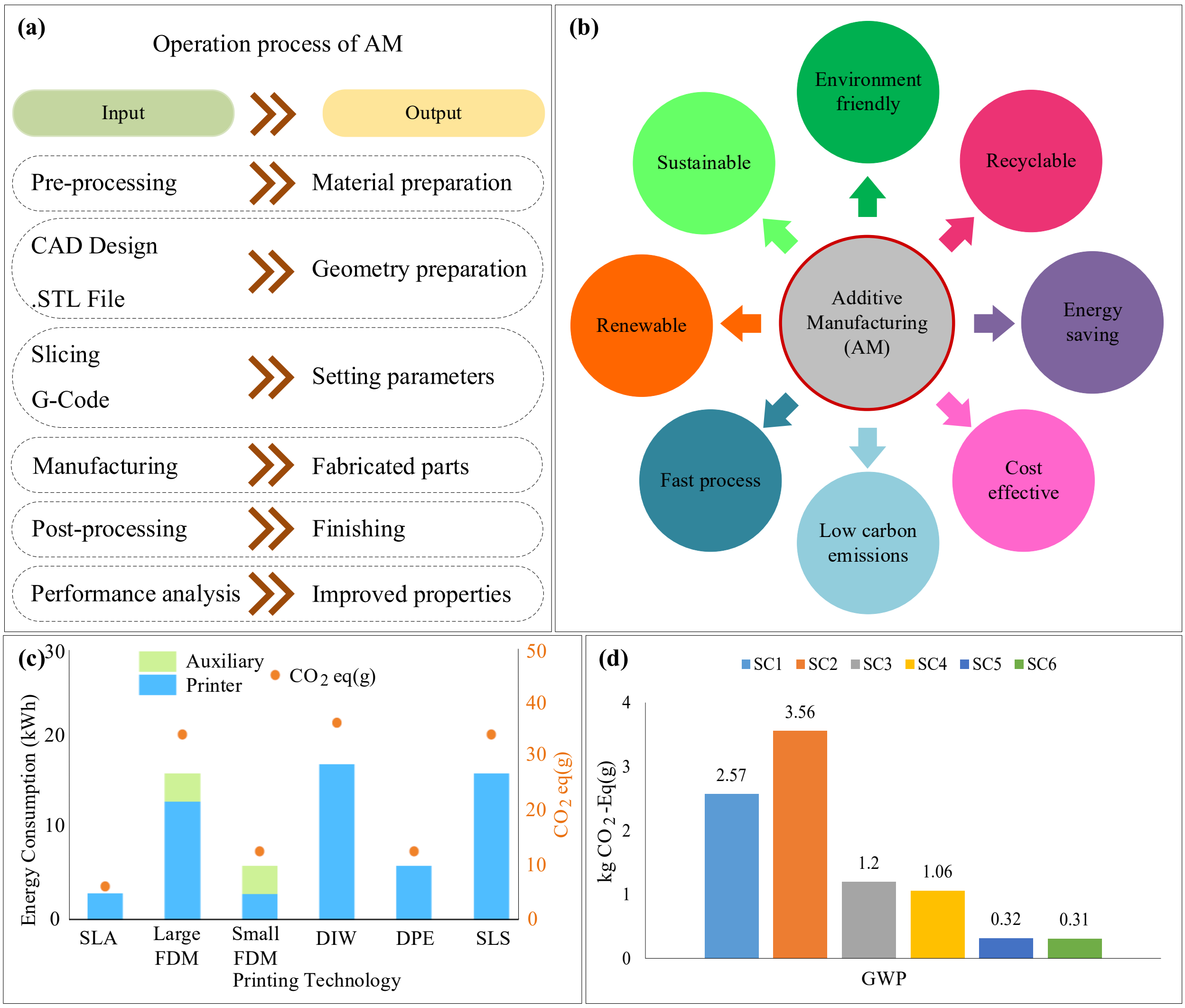

Figure 1: (a) Manufacturing processes of additive manufacturing (AM) methods; (b) benefits of AM methods [1], (c) energy consumption of different AM methods [3], (d) comparison of carbon dioxide emissions among different manufacturing methods [4].

Moreover, AM possesses several other highly demanded industrial features, including recyclability, renewability, biodegradability, cost-effectiveness, prolonged service life and environmental friendliness, making it superior to conventional manufacturing processes [5]. In particular to aerospace and automotive industries, the main goal is to reduce the weight of the materials with increased the machine and material overall efficiency which can be achieved through the AM or 3D/4D printing techniques [6]. However, in the biomedical industry, AM plays a significant role in designing prototypes of complex structures, which assists both researchers and industries in decision-making processes and, in some cases, is applied directly in real-life scenarios such as bio implantations [7]. Based on the type of raw materials or reinforcement materials and manufacturing processes, the AM or 3D printing methods are classified as material extrusion (ME), vat polymerization (VP), material jetting (MJ), sheet lamination (SL), powder bed fusion (PBF), direct energy deposition (DED), binder jetting (BJ), Cold Spray Additive Manufacturing, and additive friction stir deposition [7]. In most cases, the manufacturing process follows a similar process flow. Initially, a 3D CAD model is created using specialized design software [8]. The model is then converted into an STL file format, which defines the surface geometry of the part. This STL file is subsequently imported into slicing software, where it is digitally divided into layers and the corresponding G-code is generated. The slicing software also enables the configuration of key manufacturing parameters such as layer thickness, print speed, and infill density. Finally, the generated G-code is transferred to the 3D printing machine, which fabricates the component layer by layer to produce the final part. The manufacturing processes of additive manufacturing (AM) methods are illustrated in **Figures** 1(a) and 1(b). In contrast, **Figures** 1(c) and 1(d) depict the energy consumption and carbon dioxide emissions associated with various AM methods and conventional manufacturing techniques.

Considering these outstanding advantages, the adoption of AM or 3D/4D printing has significantly increased in modern industries. One study reported that the market size of the U.S. AM industry was approximately USD 3.56 million in 2022, and it is projected to grow at a compound annual growth rate (CAGR) of 21.3% from 2023 to 2030. Furthermore, the analysis revealed that this method supports the production of software, hardware, and related services, with hardware alone accounting for more than 64.1% of the total revenue share in 2022[9]. However, a recent study highlighted that the market revenue of additive manufacturing (AM) in the U.S. market was USD 17.99 billion in 2024, and it is projected to increase linearly to USD 110.13 billion, with a compound annual growth rate (CAGR) of 19.83%, as depicted in **Figures** 2 (a) and 2 (b). The study further indicated the market share by region as follows: North America – 36.14%, Europe – 30.40%, Asia-Pacific – 26.41%, Latin America – 5.02%, and the Middle East and Africa – 2.03%[10], as shown in **Figure** 2(c). **Figure** 2(d) presents the market share distribution of different types of 3D printers, including industrial and desktop systems. In addition, the adoption of AM or 3D printing contributes to reducing carbon dioxide emissions, which are typically produced through conventional manufacturing processes. For example, one study highlighted that AM can reduce carbon dioxide emissions by up to 70% in the building and construction industries. Notably, the AM market has shown significant growth in healthcare and biomedical industries. According to the study, the market value of AM in the U.S. healthcare sector was USD 7.4 billion in 2022 and is expected to reach approximately USD 27.3 billion by 2030[11]. The analysis further indicated that the market's CAGR would be 18.1%, with key applications in medical implants, prosthetics, wearable devices, tissue engineering, dental applications, and other related fields, as depicted in **Figure** 3 (a).

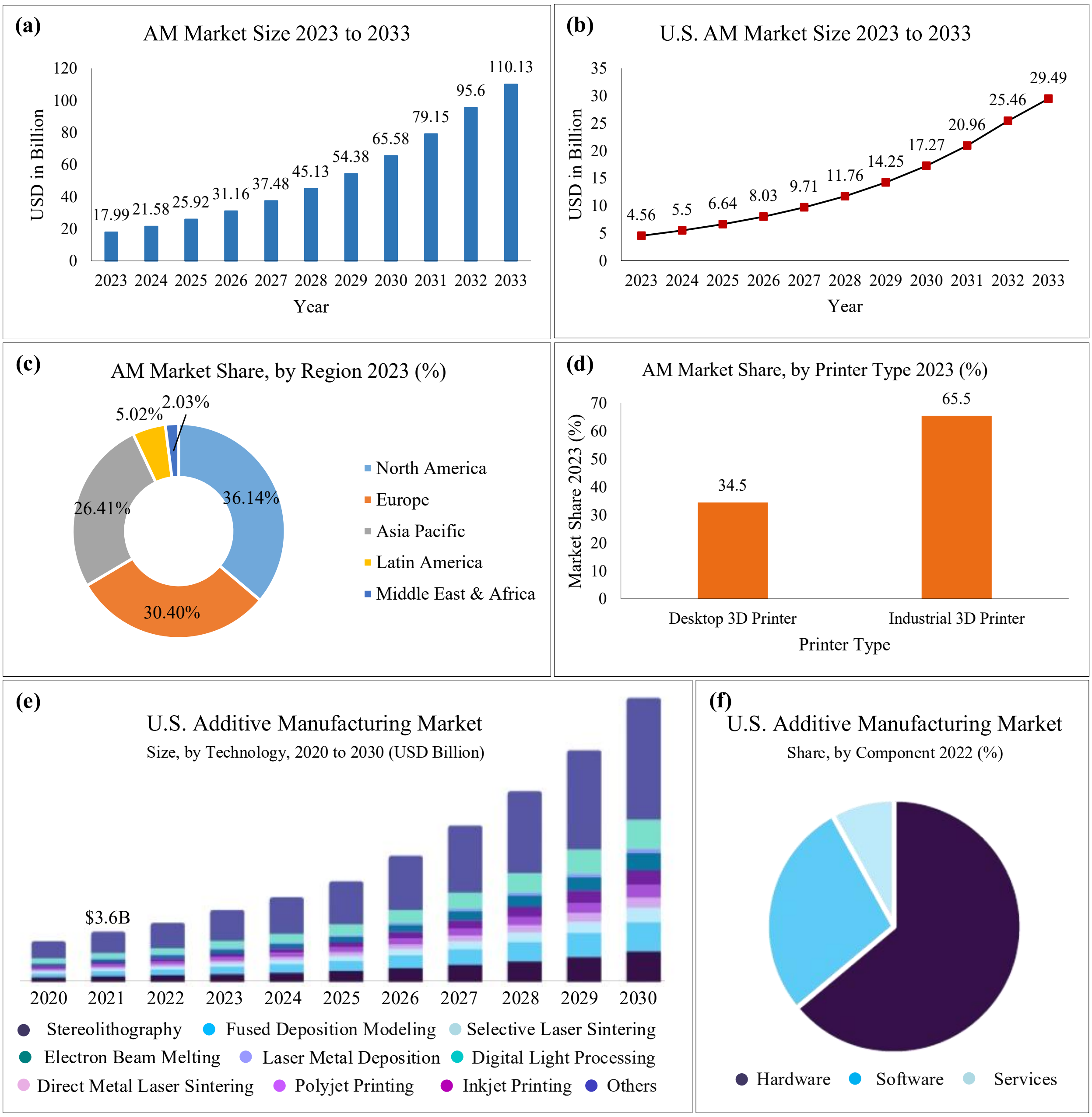

Figure 2: (a–b) Analysis of the U.S. additive manufacturing (AM) market size; (c) regional distribution of the AM market share in 2023; (d) AM market share in 2023 based on different types of 3D printers[10], (e) projected U.S. AM market trends based on different manufacturing methods, and (f) U.S. market shares of AM-fabricated hardware, software, and services [12].

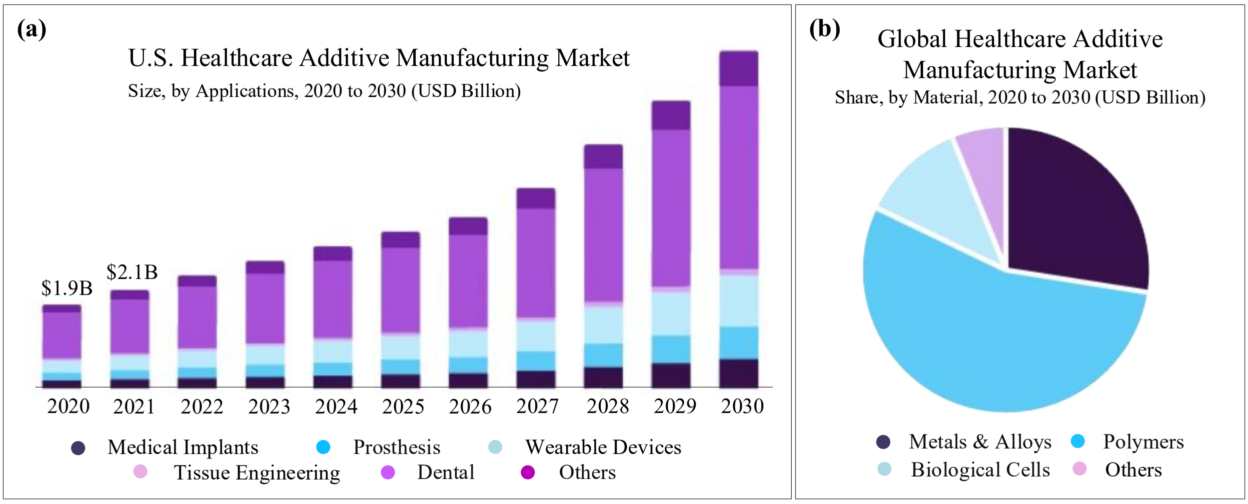

Figure 3: (a) U.S. additive manufacturing (AM) market size in biomedical industries and (b) global market size of AM-fabricated metals, polymers, and biological cells based on different material types [11].

Moreover, the study demonstrated that the market value of polymers in AM is considerably higher compared to metals, biological cells, and other materials, presented in **Figure** 3 (b). Reducing carbon dioxide emissions and energy consumption in manufacturing processes has become one of the major priorities of modern industries, as most manufacturing operations are directly or indirectly associated with carbon emissions throughout their production stages [1]. In the aviation industry alone, approximately 3% of global greenhouse gas emissions originate from this sector, and this figure is expected to increase by 300–500% by 2050. However, this can be drastically reduced through the adoption of 3D/4D printing technologies in various applications[13] . Compared to traditional manufacturing processes, additive manufacturing (AM) or 3D/4D printing can produce the desired components with significantly lower carbon emissions and energy consumption. A comparative study analyzed the environmental impacts of a 3D-printed part versus a conventionally manufactured one [4]. The findings revealed that replacing conventional manufacturing machines with industrial-scale 3D printers can reduce global warming potential by about 88%, decrease carbon emissions by 94%, and improve energy efficiency and material utilization through waste reduction and enhanced performance. Similarly, another study compared different 3D printing methods used in pharmaceutical applications and found that most 3D printers produced less than 120 g CO_2-eq per 10 units—substantially lower than conventionally manufactured alternatives [3]. Furthermore, specific examples of carbon emission reductions have been reported in the construction industry. One investigation found that adopting 3D printing technology could potentially reduce carbon emissions by approximately 16.16% compared to conventional manufacturing processes in construction [14]. Regarding energy consumption, it varies depending on the 3D printing process and selected parameters, although it generally remains more efficient than traditional methods. For instance, a study on fused deposition modeling (FDM) revealed that higher layer thickness, higher printing speeds, and lower bed temperatures significantly reduced total energy consumption. The study further concluded that bed temperature alone accounted for 60–70% of the total energy use in FDM 3D printing [15].

Lattices are a class of cellular structures intentionally designed with voids to enhance the overall efficiency of materials by reducing weight, decreasing manufacturing costs, and maintaining desired mechanical performance compared to conventional solid structures used in various domains [16,17]. Although the primary objective of lattice structures is to improve load-bearing capacity in different applications, it is important to note that variations in lattice geometry, material type, and fabrication processes can result in different mechanical and functional responses. The selection of lattice configuration and material type largely depends on the intended application. In biomedical applications, materials such as ceramics, metals, polymers, hydrogels, and their composites or hybrid composites are widely employed for the fabrication of lattice structures [18]. Lattices are generally classified based on their porosity characteristics and unit cell orientation [18]. Specifically, in tissue engineering and bone scaffold applications, unit cell–based lattice structures are predominantly adopted due to their ability to mimic natural bone architecture. Among all available fabrication techniques, additively manufactured lattice structures are considered more suitable for biomedical applications because of their superior design flexibility, smooth surface finish, and simplified material handling compared to conventionally manufactured counterparts [19]. However, there are several limitations associated with additively manufactured lattice structures. These include insufficient mechanical strength, the need for extensive post-processing, potential material toxicity, and the requirement for complex equipment and support structures during fabrication [20]. Moreover, not all materials used in AM are approved under global standards such as those established by the U.S. Food and Drug Administration (FDA). In evaluating the performance of lattice structures, key parameters such as compressive strength, biocompatibility, biocorrosion, and biodegradation are critically assessed before their consideration for real-life biomedical applications such as bio implantations[20]. In biomedical tissue engineering applications, scaffolds are defined as three-dimensional frameworks that facilitate cell attachment, proliferation, and migration, while maintaining biocompatibility and supporting tissue regeneration and integration in vivo [21]. The main distinction between a scaffold and a lattice structure lies in their primary functions: the lattice represents the architectural component within the scaffold that plays a crucial role in tailoring its mechanical properties, including porosity, permeability, and bio-integration performance [22]. In essence, the lattice provides the engineering support, whereas the scaffold delivers the biological functionality. In scaffold design, biological performance is strongly influenced by the surface area-to-volume ratio and the geometric configuration of the internal lattice structure, which collectively determine the extent of cell–material interactions and biological responses [23]. In particular, bone tissue scaffolds are designed to enhance patient recovery by reducing pain, restoring functional capacity, and promoting new bone and cell growth within damaged regions [24]. It is important to note that the mechanical performance of a scaffold such as its load-bearing strength—is not directly responsible for cell proliferation or tissue generation. Instead, its primary role is to provide structural support to withstand physiological loads, thereby maintaining mechanical stability until new tissue formation occurs. Consequently, mechanical characterization often precedes biological assessment in scaffold evaluation, particularly for applications focused on bone and tissue engineering.

Composite materials are defined as materials in which certain fibers or particles are reinforced within a specific matrix in a particular proportion. In the case of hybrid composite materials, the types of reinforcing fibers can vary and are often more diverse than those used in traditional composites. The primary objective of developing composite materials is to achieve a combination of desirable mechanical and functional properties, such as improved load-carrying capacity, high strength, and enhanced strength-to-weight ratio [1] . In biomedical applications, composite materials are widely utilized for bone replacement, spinal and joint implants, and various other medical applications [25]. Hybrid composites, in particular, are often more advanced than conventional composites, offering superior mechanical and biological performance. In some cases, hybrid composites have demonstrated elastic modulus and strength values comparable to those of natural bone, as reported in recent studies [26]. Both conventional and hybrid composites can be fabricated from a wide range of materials—such as polymers, natural fibers, metals, ceramics, minerals, and hydrogels—depending on the specific application and intended purpose. The primary focus in biomedical fabrication lies in achieving biocompatibility and other favorable biological responses necessary for successful bio implantation. In addition to traditional additive manufacturing (AM) processes, recent research has explored innovative approaches, such as incorporating nanomaterials into fabricated parts. For example, one study fabricated a lattice scaffold from extracted cellulose reinforced with nano-hydroxyapatite (n-HAP) using an extrusion-based AM method and reported excellent biological responses, suggesting its potential for tissue engineering applications [27]. Despite these promising outcomes, several challenges can arise during the fabrication and application of AM-based lattice composite bioimplants. Improper composite formulation may lead to poor cell adhesion and impaired osseointegration, resulting in weak bonding between the lattice and surrounding tissues [28]. Furthermore, stress-shielding effects may occur if the AM-fabricated composites are composed of excessively strong or dense materials. Long-term complications can also develop after implantation, such as wear, corrosion, fibrous encapsulation, inflammation, and reduced fracture toughness. Over time, these issues may lead to cracking or failure of the implant, necessitating revision surgery. Such complications can result in prolonged recovery times, increased medical costs, and, in severe cases, fatal outcomes [28]. To overcome these challenges, further biomechanical and biological performance evaluations are required through extensive experimental trials before real-life applications or bio implantations are undertaken[29].

In material extrusion, Fused Deposition Modelling (FDM) or Fused Filament Fabrication (FFF) has become increasingly popular for fabricating lattice composite structures due to its low manufacturing cost, simpler processing, wide range of available biopolymers and composite filaments, and its environmentally friendly and energy-efficient nature[8]. Before fabricating lattice composite scaffolds, the filaments are first produced as composite formulations. For example, an extruder—either twin-screw or single-screw—is used to fabricate the filaments, where a hopper feeds the filament matrix pellets along with the desired composite powders or pellets[1,30]. Among the extrusion processes, nanoparticles are added to enhance the mechanical properties and achieve the desired performance of the lattice composite scaffolds [31]. After obtaining the filaments, they are fed into an FDM 3D printer to further fabricate the lattice composites.

FDM can be applied in multiple areas of the biomedical industry, particularly in bone defect repair, bone regeneration, osteogenesis, tissue engineering, and other related applications. For example, this research used polyetheretherketone (PEEK) incorporated with calcium hydroxyapatite (cHAp) to fabricate a lattice composite scaffold, which showed significant in vitro results and was further proposed for potential applications in bone defect repair through implantation [31]. Similarly, this study fabricated a polylactic acid (PLA) composite incorporating magnesium (Mg) and nano-hydroxyapatite (n-HA) and investigated the in vitro and in vivo outcomes of FDM-printed composite scaffolds. In the in vitro experiments, the biocompatibility, osteogenic properties, and angiogenic capabilities were evaluated, while the in vivo studies explored the underlying pathways of osteogenesis and angiogenesis. The results indicated that the 10% Mg composite exhibited optimal osteogenic properties, whereas the 20% Mg composite showed superior angiogenic effects. In terms of mechanical performance, the highest compressive modulus (200–210 MPa) was achieved at 10% Mg content. Although the addition of Mg slightly reduced the overall modulus, the study concluded that the proposed composite scaffold is a promising candidate for treating critical-size trabecular bone defects, as it demonstrated favorable outcomes in animal trials [32]. Similar observations of Mg particles were found in this study. In addition to mechanical properties, the water contact angle of the porous composite scaffold was also compared in this study [33]. The investigations revealed that, compared to PLA-Gr, the PLA-Gr-Mg scaffold performed better in terms of water contact angle — decreasing from 109° to 86.7°. The water contact angle plays a significant role in tissue engineering applications. As the water contact angle decreases, the scaffold surface becomes more hydrophilic rather than hydrophobic, which enhances the scaffold's wettability and degradability. The investigations further revealed that the proposed porous scaffold, PLA-Gr-Mg, exhibited a more suitable immersion time compared to PLA-Gr.

To enhance the biological performance of scaffolds, various surface modification techniques have been developed. In this study, poly(ε-caprolactone) (PCL) was mixed with 10 wt% β-tricalcium phosphate (β-TCP) powder, and two monomers—allylamine (AA) and 1,2-diaminocyclohexane (DACH)—were employed for plasma surface treatment. Compared to the untreated FDM-printed scaffold, which exhibited a water contact angle of 70.3° ± 7.5°, the plasma-treated scaffolds showed significantly lower contact angles ranging from 16.9° to 19.6°. This reduction indicates increased surface hydrophilicity, which in turn enhanced cell adhesion and proliferation on the scaffold surface[34]. A hybrid manufacturing approach was employed in this study. The polycaprolactone–hydroxyapatite (PCL–HA) composite was primarily fabricated using fused deposition modeling (FDM) to create the lower bone layer, providing the scaffold with structural strength and osteoconductivity. This FDM-printed layer was then transferred to a digital light processing (DLP) system, a form of vat photopolymerization (VP), to print the upper GelMA–IL-4 hydrogel layer, which enhanced the scaffold's biological functionality and imparted anti-inflammatory properties—particularly beneficial for osteochondral tissue regeneration [35]. The PCL–HA scaffold exhibited a compressive modulus of 73 ± 1 MPa, meeting the stiffness range required for spongy bone (55–480 MPa). Moreover, after integrating the GelMA hydrogel with the PCL–HA base, cell proliferation exceeded 97%, and in vivo tests over 16 weeks demonstrated that the composite scaffold restored near-normal cartilage strength, achieving a compressive modulus of 4.7 ± 0.6 MPa, which is comparable to that of native cartilage (5.9 ± 0.7 MPa). The incorporation of nanoparticles or powders can significantly enhance both the biological and mechanical properties of composite scaffolds [35]. In this study, an exceptional ceramic-based nanoparticle—Baghdadite—was incorporated into a polycaprolactone (PCL) matrix using the FDM 3D printing process to fabricate reinforced composite scaffolds for bone tissue engineering. The investigation revealed that the highest compressive strength (7.86 ± 1.07 MPa) and elastic modulus (0.42 ± 0.09 MPa) were obtained when the nanoparticle content was 30%, while the lowest values were observed in scaffolds without nanoparticles. Furthermore, in terms of biological performance—including degradation rate after four weeks, cell proliferation, and cell adhesion—the 30% Baghdadite–PCL composite exhibited the best outcomes, followed by the 15% and pure PCL scaffolds. A similar observation was also reported in this study, where the composite scaffold exhibited 97% cell viability after incorporating multifunctional bioactive glass into PLA [36]. Based on the excellent cell viability and other favorable biological properties such as cell attachment and proliferation, the material was further proposed for potential applications, particularly in bone tissue engineering.

2. LITERATURE REVEIW

To fabricate lattice composites, numerous additive manufacturing (AM) techniques have been adopted in recent years, as they enable the efficient production of complex geometries compared to conventional manufacturing processes. AM technologies are generally classified into powder bed fusion, vat polymerization, binder jetting, material extrusion, directed energy deposition, material jetting, and sheet lamination. Among these methods, material extrusion is widely used in current composite and lattice applications due to its low energy consumption, reduced carbon emissions, and compatibility with recyclability, renewability, and biodegradability principles [30]. The filaments or extrusion materials used in FDM are made of plastic. Generally, plastics are produced from chemical-based products such as petroleum, which may cause serious issue to human health. Moreover, most plastics are non-biodegradable [30]. Thus, the demand to design and fabricate biodegradable, recyclable, and sustainable filament is crucial. Polylactic Acid (PLA) is suitable for the prospect of sustainability, which is mainly made from starch and collected from natural resources (sugar, potatoes, wheat, corn, etc.) [37]. Moreover, PLA exhibits better mechanical properties, biocompatibility, and low immunogenicity and is thus suitable for multiple applications, including biomedical [38], bone scaffolding [39], tissue engineering [40], additive manufacturing or 3D printing [41], sustainable packaging [42], textile [43], structural [44], automotive [45], tissue engineering [46], drug delivery [46] technical items [47], etc. However, there are some drawbacks in PLA filament, such as poor elongation at break, lower toughness, less water absorption capability, poor melting strength, etc.[37]. Also, the use of 3D-printed PLA materials in load-bearing structures are still limited [48].

Compared to conventional or solid block structures, lattice structures are widely adopted in modern and advanced applications due to their lightweight nature, reduced material requirements, high strength-to-weight ratio, and excellent energy absorption capabilities[19]. Depending on the intended application, lattices are specifically designed with controlled and intentional voids to reduce structural weight while maintaining mechanical performance [8]. In biomedical industries, these intricate lattice structures are particularly utilized in bone tissue engineering and other tissue engineering applications. In this field, lattice scaffolds primarily support cell proliferation, migration, and enhanced biological affinity in body fluid environments. Specifically for bone applications, conventional solid structures are often associated with stress shielding, a phenomenon that can weaken the surrounding bone tissue over time due to mismatched stiffness between the implant and natural bone. To address this issue, replacing conventional solid implants with lattice structures can provide appropriate porosity and tailored stiffness, promoting better bone integration and reducing the risk of implant failure. Considering these advantages, the adoption of lattice scaffolds in bone and tissue engineering applications has increased significantly compared to conventional solid or block structures[49]. Based on strut orientation and geometric configuration, lattice structures are categorized into various types, such as simple cubic (SC), cubic, face-centered cubic (FCC), body-centered cubic (BCC), and their multiple variations. Among these, the simple cubic structure has recently been widely adopted because its design and fabrication processes are relatively straightforward and it can provide favorable mechanical and biological properties compared to other lattice structures, particularly for biomedical applications[50].

FEM tools such as ANSYS, ABAQUS are widely adopted by current researchers and industry before actual experiments to understand and predict the results to avoid uncertain errors in experiments[51]. Since FEM is a cost-effective method, various FEM methods are used by current researchers to design lattice structures and calculate mechanical properties. However a slight deviation in outcomes can be observed during FEM analysis compared to real experimentations[52]. Apart from this, FEM analysis for AM parts analysis has a limitation such as it cannot consider the manufacturing parameters during the simulation[51]. A current study investigated experimentally (SLM) and also through FEM showed that relative density and unit cell topology has a significant role in the overall performance and properties, for example while the relative density increased in the lattice the modulus of elasticity and yield strength increased significantly. This study also further conducted a comparison between three different unit cells, where the number of unit cells were 1,8 and 27. However, the number of cells did not affect the overall outcomes[50].

In biomedical applications, material extrusion–based FDM is widely adopted for rapid prototyping and real-life applications, including bone tissue engineering, general tissue engineering, and dental applications. For example, one study fabricated a PLA–stainless steel composite and reported suitable mechanical properties, proposing its potential as a next-generation biomedical material [53]. In the field of lattice scaffolds, FDM has also gained significant attention. One study fabricated an FDM-printed hydrogel shell lattice scaffold for tissue engineering applications Similarly, FDM-printed PLA/$MgTiO_3$ composite TPMS lattice scaffolds have been designed for biomedical applications, with the fabricated scaffolds proposed for use in tissue engineering and regenerative medicine [54]. In addition, functional materials have been incorporated into lattice scaffolds using the FDM method. For instance, one study used FDM to fabricate a PLA/PCL blend incorporating 4.4% halloysite nanotubes (HNTs) into a lattice scaffold and reported suitable mechanical and biological properties, including cytocompatibility and cell adhesion [55]. The study further proposed the scaffold's application in bone replacement and regeneration. A similar investigation fabricated lattice scaffolds from polyether-ether-ketone (PEEK), carbon fiber–reinforced PEEK (CFR/PEEK), nylon, and titanium (Ti) using FDM, demonstrating outstanding in vitro performance for orthopedic repair applications [56]. Furthermore, FDM-printed polymeric composite lattice scaffolds can also be applied in dental applications. This research demonstrated improved biocompatibility and suggested that such scaffolds could serve as a potential alternative to conventional metallic materials [57].

For any type of lattice structure, geometric parameters such as strut diameter, strut volume fraction, and the repeating unit cell are critical factors, in addition to the unit cell topology itself. These parameters can significantly influence—and even markedly alter—the mechanical responses under investigation. For example, this research conducted a comparison between different strut diameter (0.5-1.5 mm), strut length (12-18 mm), repeating unit (3×3×3) and (6×6×6). The study revealed that a higher number of repeating units (6 × 6 × 6) with a strut diameter of 1.5 mm provided superior compressive properties compared with structures having fewer repeating units (3 × 3 × 3) [58]. However, the complexity of these structures arises because the repeating unit size, strut diameter, and strut length are not always identical, making it challenging to establish a standardized experimental procedure. This variation occurs because strut geometry, orientation, and connectivity differ depending on the lattice type, leading to changes in structural configuration and mechanical responses. An earlier study investigated the effects of unit cell size and strut volume fraction, revealing that variations in these parameters significantly increased or decreased compressive strength, elastic modulus, and other mechanical properties as their values changed [59]. However, the study established certain linear relationships, showing that an increase in lattice volume fraction led to higher compressive modulus and strength. This behavior is primarily attributed to increased stress concentration and load-bearing capacity around the pores. Conversely, an increase in unit cell size resulted in a reduction of the overall mechanical properties of the structure [59].

Composite materials have gained significant attention in modern high-tech industries and advanced applications due to their superior mechanical properties, low weight, and multifunctional capabilities compared with single-constituent or conventional materials [60]. Composite materials can be fabricated using different types of reinforcements, such as metals, polymers, ceramics, and natural fibers. Among these, polymeric composites are widely adopted because they provide satisfactory mechanical strength, durability, and prolonged service life. However, the major drawbacks of polymeric composites include the release of certain volatile compounds, extremely long degradation times, and their contribution to carbon emissions, which significantly affect ecosystems, pollute the environment, and accelerate global warming [61]. In recent years, natural fiber–reinforced composites (NFRCs) have gained significant attention due to their ability to provide satisfactory mechanical properties and performance, including adequate strength, wide availability, recyclability, biodegradability, and low manufacturing cost. Most importantly, NFRCs align well with circular economy principles when compared with conventional synthetic or polymeric composites Moreover, NFRCs are capable of mitigating the presence of volatile organic compounds commonly found in conventional polymer-based composites. In addition to these advantages, the use of natural fibers contributes to reduced carbon emissions and helps address climate change concerns, which are key industrial demands of the 21st century [1]. Consequently, the market size and production rates of NFRCs are increasing significantly as replacements for conventional or polymeric materials, with applications in biomedical, building and construction, automotive, aerospace, and related industries. Natural fibers are primarily classified based on their sources; for example, plant fibers include wood, jute, bamboo, and PLAF, while animal fibers include sheep wool and others. Among these, plant fibers and their particles are extensively adopted in the composite industry due to their low preprocessing requirements, reduced fabrication complexity, and minimal post-processing needs [61,62]. Compared to synthetic fibers, natural fiber–reinforced composites (NFRCs) have attracted significant attention in biomedical applications due to their favorable mechanical and biological properties [63]. Based on their sources and chemical compositions, NFRCs are generally classified into plant-based and animal-based natural fibers. Plant-based natural fibers, such as wood, are primarily composed of cellulose, hemicellulose, and lignin, which contribute to their satisfactory physical, mechanical, and biological properties when used in body fluid environments, particularly in tissue engineering applications [64]. Although animal-based natural fibers are widely utilized in biomedical applications, plant-based natural fibers in various forms—such as cellulose, nanocellulose, and cellulose fibrils—have been extensively adopted in different biomedical fields, including wound healing, tissue engineering, and bone tissue engineering. Their popularity is mainly due to their ease of fabrication, less complications in pre and post processing, non-toxicity, good biocompatibility, and ability to support cell proliferation, along with their desirable performance in biological fluid environments [65]. For example, one study fabricated cartilage tissue using a nanocellulose–alginate bioink through 3D bioprinting. In addition to suitable mechanical properties, the investigation reported that the cellulose-based cartilage exhibited non-toxicity with 73% and 86% cell viability after 1 and 7 days of culture, respectively [66]. In another study, a cassava bagasse–based cellulose composite combined with gelatin was proposed for tissue engineering applications. The results demonstrated suitable mechanical performance with tensile strength ranging from 5.1 to 7.3 MPa and Young's modulus between 258 and 333 MPa, along with favorable thermal properties [67]. A cellulose and chitin nanofibril–based scaffold was also developed in another investigation, which demonstrated promising biological properties including cell proliferation and attachment in human liver cells (HepG2 and HepaRG). The in vitro results showed improved cytocompatibility, and human mesenchymal stem cell cultures exhibited enhanced cell attachment, indicating potential for bone tissue engineering and regenerative applications [68]. Similarly, cellulose nanofiber (CNF)-based hydrogel composite scaffolds were developed for tissue engineering applications and demonstrated favorable biological properties [69]. The results indicated that cell proliferation significantly increased between 2 and 7 days of culture, suggesting that the scaffold supports sustained cell growth in human adipose-derived stem cells (hASCs) [69]. In another study, a cellulose-based hydrogel composite scaffold was developed for tissue engineering, where cell viability ranged from 75% to 96% after 24 hours of incubation in L929 fibroblast cells, confirming its cytocompatibility [70].

Particularly focusing on 3D printing, several recent studies have fabricated cellulose-based scaffolds for tissue engineering applications. For instance, one study designed a scaffold composed of nanocellulose blended with PCL and hydroxyapatite using material extrusion–based printing, which demonstrated approximately 90% cell viability in MG-63 osteoblast cells. Fluorescence microscopy further confirmed strong cell adhesion on the scaffold surface, indicating its suitability for bone tissue engineering applications [71]. In another investigation, a polyurethane–cellulose composite scaffold was fabricated using 3D printing, which exhibited improved degradation behavior, shape stability, and surface characteristics compared to pure polyurethane, suggesting its potential for tissue engineering applications [72]. Similarly, a cellulose-based 3D-printed nanomembrane was developed for biomedical wound healing applications. In vivo evaluations demonstrated its effectiveness in treating ulcers and other skin-related complications, highlighting its potential for clinical wound healing applications [73].

In FDM printing, manufacturing parameters play a crucial role in determining the mechanical properties of the fabricated structures. However, these parameters are not always identical for every composite or single-constituent material. Material properties can vary significantly depending on the geometry, processing parameters, and material composition used in the fabrication process [8,30]. Among the various manufacturing parameters, layer height is considered one of the most critical factors, as it represents the distance between two deposited layers during printing [8,30]. Generally, a lower layer height tends to produce better mechanical strength compared to a thicker layer height. In many cases, optimal outcomes are obtained at lower layer heights (e.g., 0.1 mm) compared to higher layer heights ranging from 0.15 to 0.30 mm. This trend is particularly evident in lattice-type structures as well [8,30,74]. The primary reason for this behavior is that a smaller layer height promotes improved interlayer bonding and fusion while reducing voids and unintended gaps between layers, which ultimately enhances the mechanical performance of the printed structure. For instance, one study reported the highest tensile strength of 32 MPa for FDM-printed PLA when the layer height was set to 0.1 mm [75]. Similarly, in lattice structures, the highest compressive strength value of 14.57 MPa was obtained for PLA when printed with a 0.1 mm layer height[76].

In FDM printing machines, nozzle temperature is also an important parameter that determines how the material is heated and melted before being extruded through the nozzle to form the desired part [30]. In lattice structures, nozzle temperature significantly affects the mechanical and structural properties of the printed components. For instance, one study reported a tensile strength of 50.16 MPa and an elastic modulus of 4340.38 MPa when the nozzle temperature was set to 230 °C [48]. Further investigation comparing different nozzle temperatures revealed that for PLA lattice structures, increasing the temperature from 200 °C to 230 °C improved the tensile strength and elastic modulus by 4.3% to 11.06%. However, when the temperature increased further from 230 °C to 240 °C, the tensile strength decreased by 1.02% of lattice structures. Therefore, excessively high temperatures are sometimes unsuitable for polymeric materials used in lattice structures, as they can induce manufacturing defects such as over-extrusion, material degradation, irregular shapes, and void formation, which significantly reduce the overall performance of the lattice structures [30,48,77]. A similar observation was reported for PLA fluorite lattice structures, where optimization results showed that the highest compressive strength of 12.22 MPa was obtained at a nozzle temperature of 205 °C within the investigated range of 205–225 °C [78]. In biomedical applications, the properties of lattice scaffold structures are also strongly influenced by nozzle temperature. One study conducted a comparative analysis of manufacturing parameters, including layer height and nozzle temperature, and found that nozzle temperature significantly affected fatigue resistance. The optimal temperature was identified as 190 °C, at which the scaffold demonstrated the highest fatigue resistance [79].

Similar to layer height and nozzle temperature, infill density is another important parameter that can significantly influence the overall performance of FDM-fabricated parts. Infill density refers to the proportion of material used to fill the internal structure of a printed part [80]. The internal infill can be produced in different patterns; however, the infill percentage generally has a greater influence on mechanical properties than the infill pattern itself [81]. Typically, the infill percentage ranges from 20% to 100%, depending on the required strength and material usage [80,81]. Previous studies have shown that infill density has a significant effect on the mechanical performance of materials such as PLA and PLA/carbon fiber (PLA/CF) composites. For example, one study reported that as the infill percentage increased from 20% to 80%, the compressive modulus increased significantly, reaching the highest value of 1087.19 MPa at 80% infill density [82]. Similarly, another investigation examined the effect of infill density on BCC lattice structures using an optimization approach. Among the tested infill percentages of 50%, 75%, and 100%, the highest compressive strength of 15.01 MPa for PLA was obtained at 100% infill density [76]. In another study on cellular-based FDM-printed PLA lattice structures, it was observed that increasing the infill percentage from 70% to 100% (an increase of 30%) resulted in a 26.6% improvement in mechanical strength [83]. Therefore, regardless of the material or structural design, careful selection of infill density is essential to achieve optimal mechanical performance in FDM-fabricated components.

Printing speed is another crucial parameter that reflects the movement rate of the nozzle while depositing material from one layer to another to form the structure. It is also directly related to the fabrication time required to produce a 3D-printed part [84]. Generally, lower printing speeds require longer printing times, whereas higher speeds reduce the overall fabrication time. However, in many cases, lower printing speeds are preferred to achieve better mechanical properties. For example, one study compared the effects of printing speeds of 30, 50, and 70 mm/s on the mechanical properties of FDM-printed wood/PLA composites. The results revealed that the lowest printing speed of 30 mm/s produced the best mechanical performance, with a tensile strength of 19.8 ± 0.8 MPa, modulus of rigidity of 34.0 ± 1.5 MPa, and compressive strength of 31.8 ± 0.6 MPa, compared to parts printed at 50 and 70 mm/s[84]. Similarly, another investigation reported that as the printing speed increased from 30 mm/s to 60 mm/s, the mechanical strength decreased linearly, and the optimal printing speed was found to be 30 mm/s [85]. However, in lattice structures, a different phenomenon has been observed. For instance, one study investigated the effect of printing speed on PLA-fabricated octet truss lattice structures and found that as the printing speed increased from 30 mm/s to 90 mm/s, the mechanical strength also increased. The optimal printing speed in this case was 90 mm/s [86]. A similar observation was reported for PLA-based simple cubic lattice structures, where the highest compressive strength 4.613 MPa was obtained at a printing speed of 50 mm/s, compared to other tested speeds of 30, 40, and 60 mm/s [8]. Therefore, it can be clearly observed that the effect of printing speed is not always consistent or linear. Instead, it largely depends on factors such as geometry, structural design, and the mechanical properties required for the fabricated parts.

Artificial intelligence (AI) and machine learning (ML) are advanced predictive techniques that have been widely adopted in modern industries to estimate mechanical performance and material properties with high accuracy, reducing the complexity associated with traditional statistical and theoretical computation methods [87]. Numerous machine learning models have recently been applied in the composite materials industry[1]. Among these, classical ML models such as linear regression, decision trees, random forests, and support vector machines are commonly used. In contrast, ensemble methods including XGBoost, CatBoost, and LightGBM are particularly effective for handling complex datasets and capturing nonlinear relationships. Furthermore, neural networks and deep learning approaches are increasingly employed in dense-network and multimodal frameworks for advanced predictive investigations[1]. Prediction accuracy is commonly evaluated using performance metrics such as R^2, MAE, MSE, RMSE, and MAPE.

In the context of composite material performance and property prediction, ML models have been extensively adopted. Artificial neural network (ANN) models have been used to predict the influence of FDM process parameters—such as infill density and printing orientation—on polyamide–carbon fiber and polyamide–glass fiber composites. These studies reported high prediction accuracy, with R^2 values approaching 0.99 for tensile strength and elastic modulus prediction, outperforming conventional statistical methods[88] Similarly, XGBoost models applied to FDM-printed natural fiber-reinforced composites (NFRCs) achieved R^2 values in the range of 0.99–1.00 for predicting tensile, flexural, and impact properties, surpassing linear regression and SVM models[89]. However, a multi-objective optimization framework was developed in this research for FDM-printed carbon-fiber-reinforced nylon composites using different AI models. The ANN model outperformed linear regression, achieving an R^2 value of approximately 0.99 in predicting tensile and impact strength, while the PSI–VIKOR method was used to determine the optimal manufacturing parameters [90].

For triply periodic minimal surface (TPMS) lattices, a machine learning framework has been developed for FDM-printed PLA-based lattice structures. Comparative studies among different ML models revealed that random forest and decision tree models outperformed others, achieving R^2 values of 0.99–1.00 with RMSE values between 0.08 and 0.12, outperforming CNN and

Bayesian regression models [91]. An another study, an auxetic foam-type lattice structure was designed, and its mechanical performance was predicted based on lattice type, cell size, and wall thickness using various ML models. Among these, ANN achieved the best performance, outperforming linear regression, random forest, and decision tree models, with an R^2 value of 0.93 and low prediction errors. The results indicated that cell size and wall thickness were the most influential parameters governing mechanical behavior[92].

Despite the growing interest in ML-based prediction of lattice composite performance, studies focusing specifically on lattice-reinforced composites remain limited. To predict the flexural properties of FDM-printed Kevlar-reinforced ABS lattice composites, several ML models—including linear regression, ANN, random forest, and SVM—were applied to TPMS lattice geometries such as gyroid and diamond. The results demonstrated that the random forest model achieved the best prediction performance, with $R^2 = 0.93$, RMSE = 0.09, and MAE = 0.07 [87]. Similarly, an AI-integrated framework was employed to investigate the performance of TPMS lattice structures fabricated via FDM from PLA/HAP/GO composites, considering parameters such as strut thickness, porosity, and cell geometry. The study reported approximately 20% improvement in energy absorption and 15% enhancement in thermo-mechanical properties compared to traditional designs. In this framework, AI primarily functioned to correlate structural parameters with mechanical properties and to guide lattice optimization, ultimately demonstrating suitability for bone scaffold applications [93].

To understand the biological performance of any biomaterial, in vitro and in vivo evaluations are typically conducted. However, before these biological studies, several physical and physiochemical evaluations are also performed, such as water absorption, thickness swelling ratio, and contact angle measurements. These evaluations help to understand the surface characteristics and interaction of the material with aqueous environments. These properties are closely related to the wettability of the scaffold surface, which plays an important role in promoting cell adhesion, cell proliferation, cell migration, and protein adsorption [94]. For example, it has been reported that when the contact angle is less than 90°, the surface is considered hydrophilic, indicating a higher affinity toward water or biological fluids, which is beneficial for scaffold–cell interactions in tissue engineering applications [95]. In addition, water absorption and thickness swelling are also important parameters for tissue engineering materials because they reflect the hydrophilic or hydrophobic nature of the scaffold, which can influence its interaction with biological fluids and ultimately affect its biological performance [95].

From the existing literature, only a limited number of studies have investigated the effects of strut diameter and filament type on the mechanical properties of lattice structures. Although extensive research has been conducted on FDM-printed PLA components—focusing on parameters such as layer height, nozzle temperature, printing speed, bed temperature, and infill density—their influence on lattice structures remains insufficiently explored [48,83,96–98] Furthermore, no comprehensive study has been identified that optimizes printing parameters specifically for achieving superior mechanical performance in PLA-based lattice designs. In addition, natural fiber–reinforced composites (NFRCs) have emerged as sustainable alternatives to conventional polymer composites. Simultaneously, artificial intelligence and machine learning techniques have demonstrated strong potential in optimizing manufacturing parameters and enhancing the prediction accuracy of mechanical behavior. However, only a limited number of studies have applied AI-based approaches to investigate the properties of NFRC lattice structures, highlighting a significant research gap.

Moreover, the influence of manufacturing parameters on FDM-fabricated biocomposite lattice scaffold structures and their resulting mechanical, physical, and biological properties remains largely unexplored. To the best of the authors' knowledge, very few studies have examined the combined effects of these parameters on both material performance and biological response, particularly in the context of tissue engineering applications.

Therefore, the main objective of this study is to investigate the effects of manufacturing parameters on the mechanical, physical, and biological properties of PLA and PLA-wood composite lattice structures using statistical approaches. Additionally, scanning electron microscopy (SEM) analysis is performed to correlate the microstructural characteristics with the observed material performance, providing deeper insight into the influence of processing parameters. This thesis addresses the following key research questions:

1. How do different lattice types, filament materials, and strut diameters affect the compressive properties?
2. Which FDM printing parameters significantly influence the compressive properties of PLA lattice structures?
3. How can optimized PLA lattice structures be utilized for biomedical applications?
4. How do FDM manufacturing parameters influence the physical and mechanical properties of wood–PLA composite lattice structures?
5. How do optimized parameters of wood–PLA composite lattices affect cell viability at different concentration levels?

In **Section 3**, the overall methodology is presented in detail, including the design, fabrication, experimental procedures, and standard testing methods. **Section 4** demonstrates and compares the finite element method (FEM), experimental analysis, statistical methods, scanning electron microscopy (SEM), microscopic analysis, and machine learning approaches to enhance the mechanical, physical, and biological properties. Additionally, the applicability of this research is discussed in this section. **Section 5** summarizes the obtained results. Finally, **Section 6** highlights the future perspectives and limitations of this thesis.

3.RESEARCH METHODOLOGY

In this section, the overall methodology for the lattice composite is presented, covering the design, fabrication, and experimental processes. The method includes finite element method (FEM) analysis, modeling, fabrication, data analysis, machine learning, and other related processes. Moreover, the necessary precautions, along with the biological evaluations, are discussed in detail in accordance with ASTM and ISO standards.

3.1 Research methodology for FEM investigations on different lattice structures

To optimize and understand the performance of different strut diameters, filament types, and lattice structures, finite element method (FEM) analysis was first conducted. Three different polymeric materials such as PLA, ABS and nylon filaments are considered to calculate the compressive behavior of different lattices and their struts. The isotropic properties of all filaments are listed in Table 1. The material properties of the considered polymeric materials are taken from the literature[99,100].

Table 1: Isotropic material properties of PLA,ABS, and nylon.

Material	Young's modulus (GPa)	Poisson's ratio	Density (g/cm3)
PLA	3.5	0.38	1.25
Nylon 618	2.95	0.36	1.10
ABS	0.862	0.35	0.78

A design of experiment (DOE) was developed using a software called Minitab-19 to investigate the compressive behavior on three different lattice structures, filaments and strut diameters. The design is based on Taguchi L9 orthogonal array. The DOE has been presented in Table 2.

Table 2: Design of the experiment in L9 orthogonal array.

Factor	Name	Level values	Column	Level
A	Strut diameter	1.0 1.5 2.0	1	3
B	Filament type	PLA ABS Nylon	2	3
C	Lattice type	SC SC-BCC FCC	3	3

The validity of this work is checked by comparing with the literature [50], where two types of simple cubic (SC) unit cells (1,27 cell numbers) with Ti-6Al-4V alloy material are considered. The material properties are defined as elastic-plastic in behavior by the Johnson-Cook material model. However, it should be noted that the increment steps are 15 for the analysis. From the analysis and comparison, it is evident that the results obtained by FEM and other literature outcomes are compatible with each other. The stress-strain curve with comparison is presented in **Figure 4** (a) and Figure 4 (b) below.

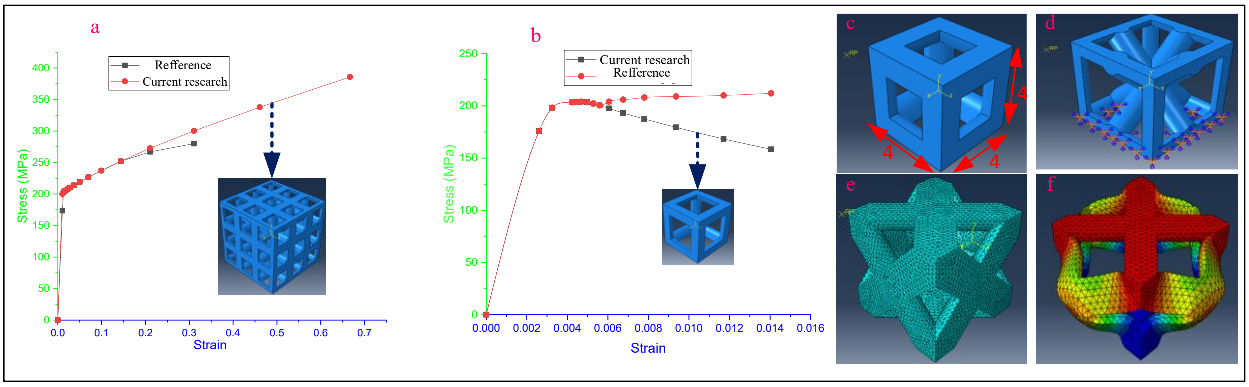

Figure 4: (a) Stress-strain curve comparison with current research outcomes and other literature outcomes[50]for unit cell 27, (b) Stress-strain curve comparison with current research outcomes and other literature outcomes[50] for unit cell 1, (c) SC lattice at 2 mm strut diameter, (d) SC-BCC lattice at 1.0 mm strut diameter with implemented boundary conditions, (e) FCC lattice structure at 1.5 mm strut diameter with tetrahedral mesh, (f) FCC lattice structure's deformation pattern after compression test.

First, the lattice unit cell has been designed according to DOE's strut diameter. Since, the number of unit cell does not play a significant role in computing the mechanical properties [50], therefore, we considered a unit cell in this study. The overall dimension in the unit cell is 4 mm x 4 mm x 4 mm. After that, the material properties are assigned to the unit cell and a tetrahedral mesh is created in the unit cell. The boundary and loading conditions need to be defined in the lattice cell before conducting the compression test. Hence, three sets are created at the bottom, top and a reference point of the lattice structure to define the boundary and loading conditions.

However, the reference point is defined at the (0,4,5) point to create a gap between the loading point and the lattice structure. Later on, the bottom section is fixed in all directions and load is generated from the Y direction of the reference point. An earlier study found that different compression speeds have a significant role in the outcomes[101], therefore in this study the compression speed is considered as 1.5 mm/min which is suitable for polymer type materials[76]. The incrementation in the loading step is 15. Before submitting the simulation, a constraint equation has been created which is defined in the top sets and reference point set. The force-displacement curve has been plotted from the reference point. The finite element set up is demonstrated in **Figure 4** (c-f).

3.2 Research method for PLA simple cubic lattice scaffold investigations

The material used in this research is a commercial PLA filament with a diameter of 1.75 mm. The material was purchased from Creality (Shenzhen, P.R. China). Compared to other lattice structures such as body centered cubic, and face centered cubic, simple cubic lattice structure provides better mechanical performance[50]. Therefore, this research considers a simple cubic lattice structure. Firstly, a CAD model is designed in a commercial CAD software with a dimension of 36.0 mm × 36.0 mm × 30.21 mm to conduct the compression test (according to ASTM D695) [102] and evaluate the mechanical properties.

The design of the experiment (DOE) has been performed through Minitab 19. For Taguchi selection, 4 level design has been opted, considering four significant printing parameters such as layer height, printing temperatures, printing speed, and bed temperatures. The levels were chosen based on the manufacturer's instruction and existing literature. Finally, the L_{16} orthogonal array has been employed to design the DOE. DOE is presented in detail in Table 3.

Table 3: Taguchi L_{16} Experimental design (DOE)

DOE SL.	Layer height (mm)	Printing temperature (°C)	Printing speed (mm/s)	Bed temperature (°C)
E-1	0.1	195	30	50
E-2	0.1	200	40	55
E-3	0.1	205	50	60
E-4	0.1	210	60	65
E-5	0.15	195	40	60
E-6	0.15	200	30	65
E-7	0.15	205	60	50
E-8	0.15	210	50	55
E-9	0.2	195	50	65
E-10	0.2	200	60	60
E-11	0.2	205	30	55
E-12	0.2	210	40	50
E-13	0.25	195	60	55
E-14	0.25	200	50	50
E-15	0.25	205	40	65
E-16	0.25	210	30	60

To fabricate the design on the FDM 3D printing machine, the model has been introduced with an available slicer software named Creality Slicer. After combining all the input parameters from the DOE into the slicing software, the software provides a predicted production time with a G-code. Later on, the obtained G-code was inserted into the FDM printing machine using a memory card. During fabrication, some crucial factors, such as the dimension of the lattice structure and strut diameter, have been scrutinized. In addition, PLA filament can be significantly affected by moisture content and humidity [103,104]; therefore, this study considers some precautions, such as using a polyethylene bag to put the sample after fabrication, and checking the dimension measurements against CAD modeling for printing accuracy., as shown in **Figure 5** (b) . However, other parameters, like the infill density of 100%, shell thickness of 1.2mm, flow rate of 100%, and the nozzle size of 0.4mm are kept constant during printing.

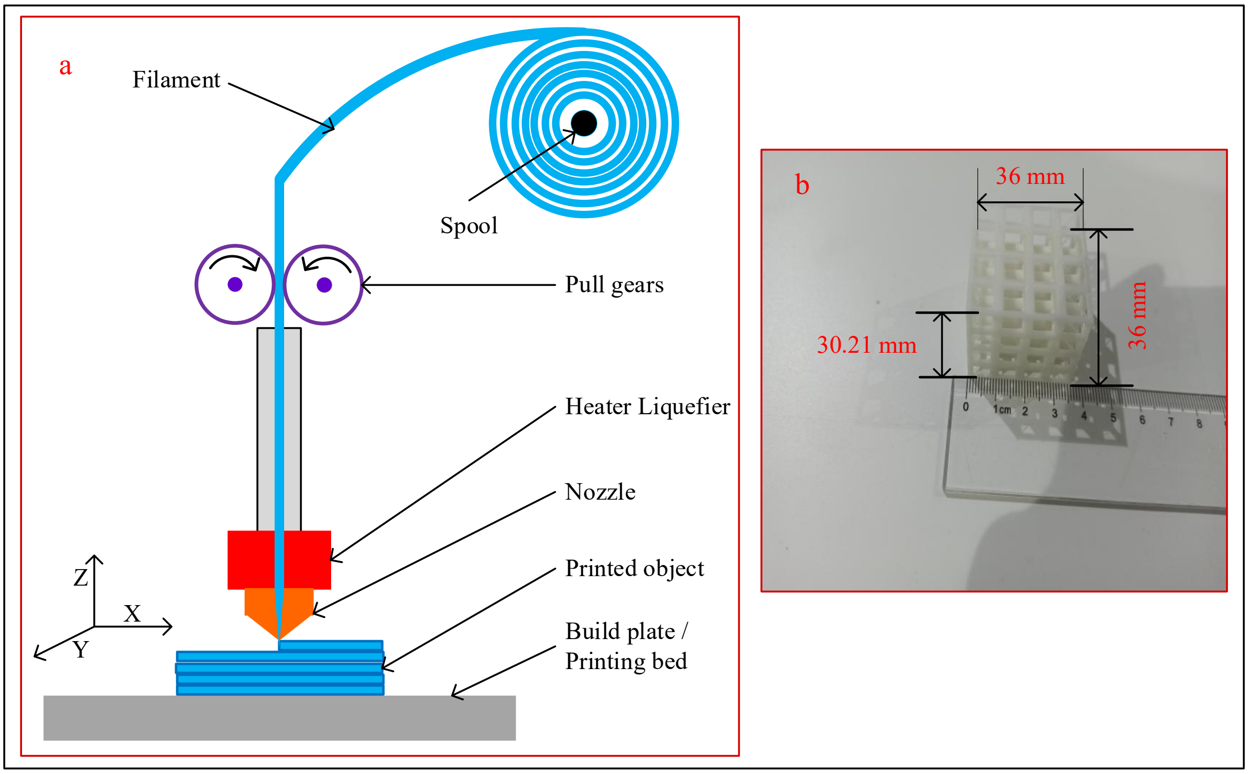

Figure 5 (a) A schematic process of lattice cube printing on FDM 3D printer, **(b)** lattice dimension measurement.

The compression test has been conducted (according to ASTM-D695) on a SENS universal testing machine (model CMT-6000) with a compression speed of 2 mm/min and a 10 KN load cell. An earlier study found that different compression speeds can remarkably influence mechanical properties [97]. To achieve better outcomes, this study considered 2mm/min speed, which has been obtained from other literatures of PLA materials[48,99,105] . Likewise, to get accurate results, five samples are tested of each consideration (from DOE). The preload between platens and samples is 0-5N for all tests. The accuracy of this universal testing machine is ±0.5%.

On the other hand, SEM test has been conducted on a JSM7800F (origin-Japan) machine. First, the sample is cut with scissors, and a specific size is taken from different regions of the sample. After that, the sample was attached to the sample plate by using conductive glue. Before conducting the test, all samples were dried and sputtered with gold in a sputtering machine. Each sample sputtered 4 times (a total of 120 seconds). It is important to note that the conductive glue and spraying gold are used to increase the conductivity of the sample surface. The thickness of the coating was approximately 2-3 nanometers (nm). Later on, the sample plate was placed in the sample chamber. Finally, SEM photos of different samples have been collected at 5.0 Kilo Volt (KV) and secondary electron mode with different magnifications.

3.3 Research method for wood-PLA simple cubic lattice scaffold investigations

3.3.1. Wood-PLA lattice scaffold fabrication, mechanical, physical and biological process

In this research, also a wood–PLA composite containing 10% wood particles was used. The wood–PLA filament was commercially purchased from Qidi, a manufacturer of filaments for FDM 3D printing [106]. Although various types of commercial wood–PLA filaments are available, a 10% wood content was selected for this study because this proportions are more suitable for NFRCs based composite. A comparative study evaluated the effect of wood content ranging from 0% to 50% in PLA composites, focusing on tensile strength [107]. The results revealed that the highest tensile strength (57 MPa) was obtained at 10% wood content. As the wood proportion increased, both tensile strength and elastic modulus decreased linearly. This reduction may be attributed to increased brittleness at higher wood loadings, leading to earlier collapse or failure of the material. Furthermore, the lowest tensile strength (30 MPa) was observed at 50% wood content. However, in terms of dimensional stability, the 10% wood–PLA composite exhibits slight deviations in moisture absorption and thickness swelling ratio compared with pure PLA [78]. Nevertheless, due to the relatively low wood content, the dimensional changes in the printed parts remain limited and do not significantly affect their structural stability. The density of the considered wood–PLA filament for this study ranged from 1.22 to 1.24 g/cm³ [106].

The design of the experiment was developed using the statistical analysis software Design-Expert (Version 13). Four critical input parameters were considered: layer height, nozzle temperature, printing speed, and infill density. Previous studies have indicated that, for NFRC-based composites, lower layer heights, lower nozzle temperatures, and moderate to high infill densities are generally more suitable for FDM-fabricated parts[30]. However, these variables do not always produce consistent outcomes, as the results may vary depending on the geometry and structural configuration of the printed components. Therefore, the selected parameter ranges were determined based on existing literature and the manufacturer's recommended settings [30,106]. A Central Composite Design (CCD) was employed to structure the experimental plan. The design consisted of 30 experimental runs, including 24 unique design points and 6 replicates at the center points. The detailed design matrix is presented in **Table 4.**

Table 4: Experimental design matrix for the wood–PLA lattice composite prepared using Central Composite Design (CCD).

Input variables	Low level	High level
Layer height (mm)	0.1 mm	0.3 mm
Printing speed (mm/s)	40 mm/s	60 mm/s
Nozzle temperature (°C)	195°C	215°C
Infill density (%)	70%	100%

Apart from these variables, several additional printing parameters were kept constant throughout the investigation, as previous studies have indicated that they do not have a significant influence on the measured outcomes. These fixed parameters are listed in **Table 5.**

Table 5: Constant process parameters used in the FDM 3D printing machine.

Constant parameters	Values
Infill pattern	Cubic
Travel speed	100 mm/s
Build plate temperature	60 °C
Fan speed	100%
Z offset	0.0 mm
Top layers and bottom layers	4
Travel speed	100%

The samples for the wood-PLA lattice scaffold were designed similarly like PLA lattice. The specimens were fabricated using an FDM (Fused Deposition Modeling) 3D printer (QIDI brand, model QIDI Max 4) with a build volume of 390 × 390 × 340 mm^3 and a nozzle size of 0.4 mm. During fabrication, nozzle clogging was encountered due to the use of natural fiber-reinforced wood–PLA filament. To mitigate this issue, the nozzle was thoroughly cleaned before and after each fabrication process**.** **Figure 6(a)** illustrates the FDM fabrication process, while **Figure 6(b)** presents the fabricated wood–PLA composite lattice structure.

The primary objective of this research was to investigate the compressive behavior of the wood–PLA composite lattice. Compression testing was performed using an MTS 322 test frame with a maximum load capacity of 100 kN. The loading rate can significantly influence the mechanical response of lattice structures. To ensure consistency and avoid unintended variations in the results, a crosshead speed of 2 mm/min was selected, following previously reported studies [108,109]. Furthermore, to improve the accuracy and reliability of the experimental results, the compression displacement was limited to 22 mm. Beyond this displacement, the lattice structure exhibited densification behavior, effectively transforming into a sandwich-like compact structure and demonstrating artificially elevated compressive strength. Therefore, restricting the compression bar travel ensured that the results reflected the intrinsic compressive performance of the lattice structure prior to full densification. The compression test setup is illustrated in **Figure 6(c).**

Finally, to compare the mechanical performance within the designed DOE framework, the fracture regions of the wood–PLA lattice composites were examined using a microscope, as shown in **Figure 6(d).** The microscope used in this study was a Zeiss Stemi 2000-C model. The fractured surfaces were analyzed at different magnifications to evaluate the failure modes and crack propagation characteristics.

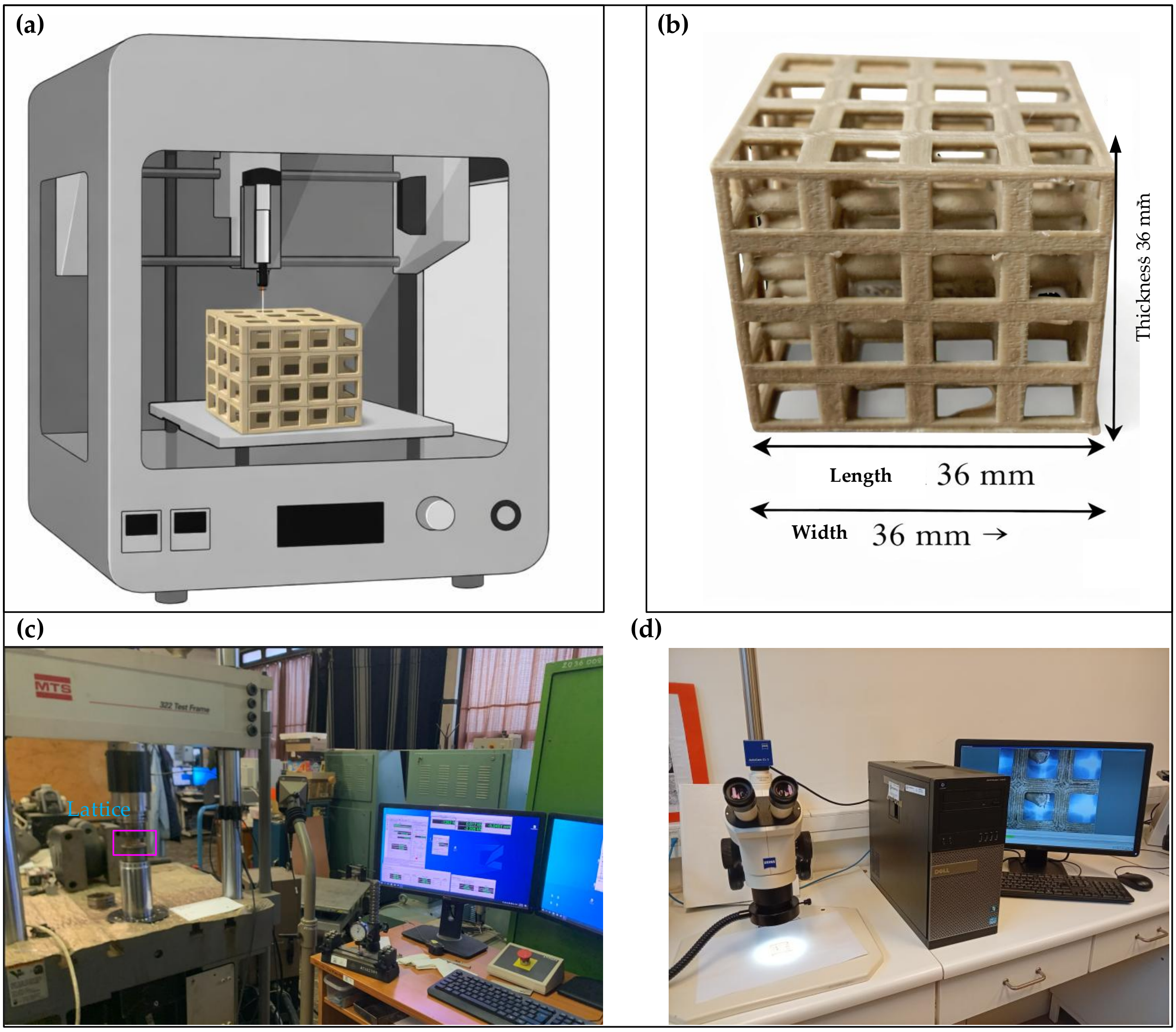

Figure 6: (a) Fabrication process of the FDM 3D-printed wood–PLA composite lattice; (b) fabricated lattice structure with dimensions; (c) compression test setup using the MTS 322 Test Frame universal testing machine; (d) microscopic examination setup using the Zeiss Stemi 2000-C.

After conducting the compression test, the load–displacement curve was obtained for each experimental design. The load values were then converted into stress by dividing by the surface area. The total surface area was 1296 mm². However, the void section was excluded by subtracting 577 mm² from the original area. Therefore, the effective cross-sectional area of the lattice was taken as 719 mm², which was used to calculate the stress of the wood–PLA composite lattice. The effective cross-sectional area mainly represents the mechanical properties of lattice-type structures, as reported in earlier studies [8,110,111].

To evaluate and understand the compressive behavior of the wood–PLA lattice composite, two key responses were considered: compressive strength and compressive modulus. These responses were determined for each DOE specimen based on its corresponding stress–strain curve. Previous studies have shown that higher values of compressive strength and compressive modulus indicate a stronger and stiffer material or structure compared to those with lower values[8]. The compressive strength and compressive modulus reported in this study represent the average of three experiments, conducted to minimize experimental errors and improve the accuracy and reliability of the overall investigation.

Water absorption and thickness swelling tests were conducted following ASTM D570, with slight modifications due to the lattice geometry of the specimens, similar to the procedure reported in the literature [112]. The lattice samples were immersed in distilled water, and the changes in mass and thickness were recorded after 24 h and 48 h of immersion as depicted in **Figure** 7 (a) and (b). To ensure accurate thickness swelling measurements, a reference point was marked on the specimen using a permanent marker so that the same location could be measured after 24 h and 48 h. For the surface wettability analysis, the static contact angle was measured using the sessile drop method according to ISO 19403-2:2024, similar to the approach described in previous research [113]. A 10 µL droplet of distilled water was deposited on the surface of the lattice specimens due to their thin-wall structure. After 30 s, the droplet images were captured using a microscopic imaging system illustrated in **Figure 7** (c). The captured images were analyzed using KSV CAM software (version 2008) to determine the contact angle. The baseline was carefully fitted to the sample surface to obtain accurate measurements. For each specimen, three contact angle measurements were taken at different locations, and the average value was reported. Prior to testing, the samples were dried and conditioned at 23 °C and handled carefully during the measurements to ensure reliable and consistent results.

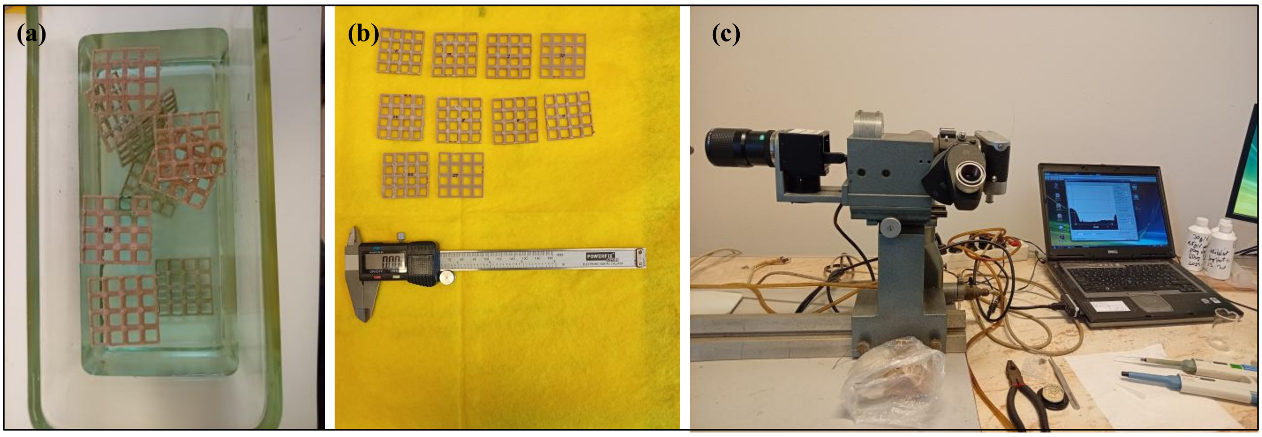

Figure 7: (a) Prepared lattice samples for the water absorption experiment, (b) water absorption and thickness swelling measurements (%) after 24 h and 48 h, and (c) experimental setup for the contact angle measurement.

Scanning electron microscopy (SEM) analysis was performed using a ZEISS EVO 10 MA SEM equipped with an EDAX Genesis Apex2 energy-dispersive X-ray spectroscopy (EDS) detector. The fracture regions and selected parts of the lattice structures were carefully considered, cut, and mounted onto the sample holder using conductive carbon cement. Prior to observation, a thin conductive gold coating was applied using a sputter coater to prevent surface charging during imaging. SEM examinations were conducted under high vacuum conditions with an accelerating voltage of 10 kV for the original surfaces and 20 kV for the fracture surfaces. The beam current was maintained at 0.4 nA during the analysis.

In order to assess the cytocompatibility of the 3D-printed wood–PLA lattice structures, a cell viability test using the Neutral Red uptake assay was performed. The human buccal carcinoma cell line TR-146 (ECACC No: 10032305, passage number 25) was seeded into a 96-well plate at a density of 1×10^4 cells per well in Dulbecco’s Modified Eagle Medium (DMEM) supplemented with cell culture additives (10% (v/v) fetal bovine serum (FBS), 3.7 g/L sodium hydrogen carbonate, 1% (v/v) non-essential amino acid solution, 100 IU/mL penicillin, and 100 µg/mL streptomycin sulphate). The cells were incubated for 7 days at 37 ± 1 °C in a humidified atmosphere containing 5% CO_2 to allow cell attachment and growth. Fragments of the 3D-printed structures were incubated in cell culture medium for 7 days at 37 ± 1 °C to prepare the material extracts. Three extract concentrations (16.6 mg/mL, 50 mg/mL, and 100 mg/mL) were prepared, and 200 µL of each extract-containing medium was added to the cells in the 96-well plate (12 wells per treatment group) after removing the original culture medium. The cells were exposed to the extracts for 24 h. After the treatment period, the medium was removed and 200 µL of Neutral Red solution (33.3 µg/mL Neutral Red dye in culture medium) was added to each well, followed by incubation for 2 h. Subsequently, the dye-containing medium was removed and 100 µL of a desorption solution consisting of isopropanol and 1 M hydrochloric acid (25:1) was added to each well to dissolve the incorporated dye. The absorbance of the extracted dye was measured at 540 nm using a Thermo Fisher Multiskan Go microplate reader (Thermo Fisher Scientific, USA). Wells without cells were used as blanks. The cell viability values were expressed as mean ± standard deviation (SD) relative to the untreated control cells containing only culture medium [114].

3.3.2. Machine Learning Modelling

In this research, machine learning (ML) models were employed as an efficient predictive tool to reduce reliance on destructive experimental testing and computationally expensive, time-consuming numerical simulations. Traditional experimental and finite element analyses, although accurate, require significant material preparation, testing time, and computational resources. By learning the relationship between printing parameters and the corresponding compressive strength and compressive modulus response from a limited set of experimental data, the developed ML models enable rapid and reliable prediction for new configurations.

The dataset constructed for machine learning prediction for this study was derived from 24 unique specimen configurations, each tracked via a unique specimen ID. The experimental stress-strain data for each specimen was uniformly sampled to yield 500 discrete points per curve. Consequently, a comprehensive dataset comprising 12,000 rows and 6 columns was generated. For the development of the predictive model, stress was defined as the target feature, while layer height, printing speed, nozzle temperature, infill density, and strain served as the input features. **Table 6** represents the dataset used for this study.

Table 6. Dataset for Machine Learning modelling

Specimen_ID	**Layer height, mm**	**Printing speed, mm/s**	**Nozzle temperature (℃)**	**Infill density (%)**	**Strain**	**Stress**
1	0.2	50	185	85	0	0.018539
1	0.2	50	185	85	0.000159	0.019113
1	0.2	50	185	85	0.000318	0.019687
.	.	.	.	.	.	.
.	.	.	.	.	.	.
.	.	.	.	.	.	.
.	.	.	.	.	.	.
24	0.3	40	215	70	0.081526	2.617483
24	0.3	40	215	70	0.081689	2.614002

The models utilized in this work are based on ensemble learning techniques. The fundamental principle of ensemble learning is to employ more than one learner and integrate their predictions to form a single model that is stronger and more accurate than any individual learner. By combining multiple models, ensemble learning improves predictive performance, robustness, and generalization capability. This framework includes several methodologies, among which bagging and boosting are the most prominent. Boosting is a major ensemble learning technique and is regarded as one of the most powerful learning methods, forming the foundation of advanced algorithms such as XGBoost, LightGBM, and CatBoost [115]. In this research only the XGBoost model is used.

Extreme Gradient Boosting (XGBoost) is a scalable implementation of gradient tree boosting that constructs new models sequentially to correct the pseudo-residuals of the previously built ensemble [116]. The high performance of XGBoost arises from both algorithmic and system-level improvements. At the algorithmic level, XGBoost enhances traditional gradient boosting by incorporating a regularized learning objective that includes both L_1 and L_2 penalties, which penalize model complexity and reduce overfitting. **Figure 8** illustrates the algorithm of XGBoost.

Another important feature of XGBoost is its sparsity-aware split-finding algorithm, which allows efficient handling of sparse data and missing values by learning optimal default paths during tree construction. From a system-level perspective, XGBoost is designed for scalability and computational efficiency through techniques such as cache-aware access patterns and out-of-core computation for datasets that exceed system memory capacity. These improvements enable XGBoost to achieve high predictive accuracy while maintaining fast training and evaluation performance [117].

To ensure a fair evaluation and prevent data leakage, the dataset was divided into an 80% training set and a 20% testing set. Instead of a standard random split, the data was strictly grouped by Specimen_ID. This grouping is crucial for physical testing data, as it ensures that all data points belonging to a single 3D-printed specimen remain entirely within either the training or the testing set. This approach forces the model to predict the behavior of truly unseen physical specimens, rather than just memorizing fragments of a stress-strain curve it has already been exposed to.

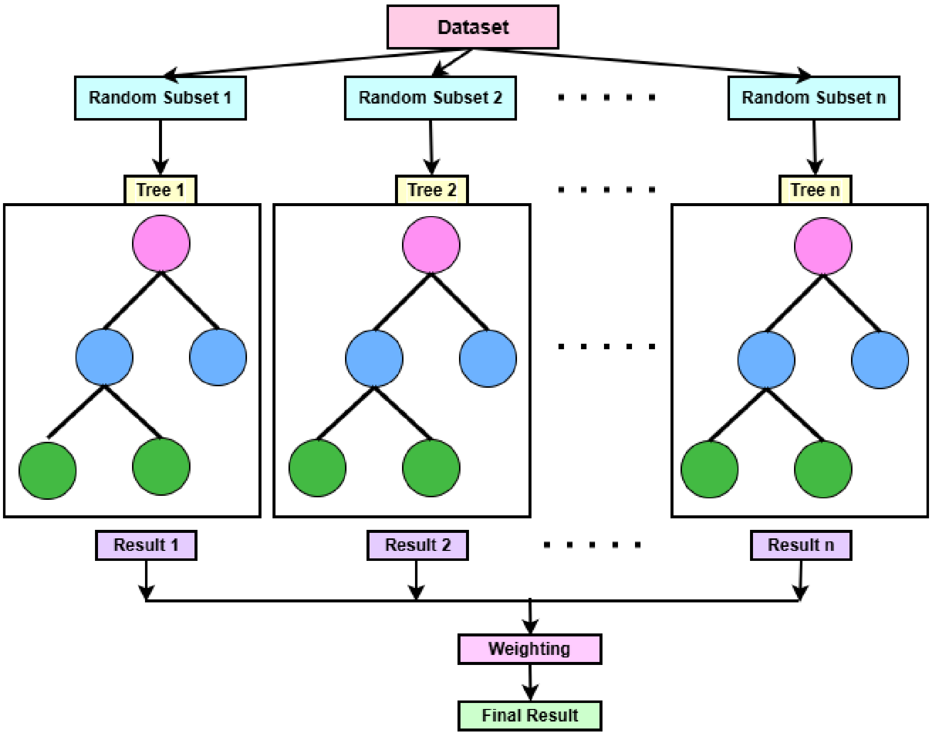

Figure 8: XGBoost Algorithm.

The machine learning models were trained on the 80% subset using 5-fold cross-validation. A fixed random seed was applied throughout this process to guarantee reproducible results and minimize random sampling bias. Finally, the model's performance and predictive accuracy were quantified using three standard regression metrics: the Coefficient of

Determination (R^2), Root Mean Square Error (RMSE), and Mean Absolute Error (MAE). Model performance is evaluated using three standard regression metrics, as described below.

Root mean squared error (RMSE) measures the square root of the average squared differences between predicted and observed values, thereby assigning greater weight to larger prediction errors and emphasizing model sensitivity to significant deviations. Eq. (1) represents the numerical formulation of RMSE.

$$RMSE = \sqrt{\frac{1}{n}\sum_{i=1}^{n} (y_i - \hat{y}_i)^2} \tag{1}$$

Mean absolute error (MAE) computes the average absolute difference between predicted and observed values, providing an intuitive and easily interpretable measure of overall model prediction accuracy. Eq. (2) is the numerical equation of MAE.

$$MAE = \frac{1}{n}\sum_{i=1}^{n} |y_i - \hat{y}_i| \tag{2}$$

Coefficient of determination (R^2) quantifies the proportion of variance in the observed data explained by the model, where a value of 1 represents a perfect prediction. The numerical formula of R^2 is given in Eq. (3).

$$R^2 = 1 - \frac{\sum_{i=1}^{n} (y_i - \hat{y}_i)^2}{\sum_{i=1}^{n} (y_i - \bar{y})^2} \tag{3}$$

This multi-metric evaluation framework ensures that each model is optimized not only for minimizing absolute and squared prediction errors but also for accurately capturing the variance in the experimental stress response across different DOE experiments.

The performance of modern machine learning (ML) systems is fundamentally governed by two distinct classes of variables: model parameters, which are learned directly from data during training, and hyperparameters, which are external configuration variables that define the learning process, model complexity, and optimization behavior[118]. Unlike model parameters, hyperparameters are not updated automatically during training and must be specified prior to model fitting. Inappropriate hyperparameter selection may therefore lead to underfitting, overfitting, or unstable learning behavior.

The systematic process of identifying optimal hyperparameter configurations is referred to as hyperparameter tuning or hyperparameter optimization [119]. In ensemble-based learning algorithms, hyperparameters such as tree depth, learning rate, number of estimators, sampling ratios, and regularization coefficients strongly influence the bias–variance trade-off and overall generalization performance. Consequently, careful optimization of these hyperparameters is essential, particularly when working with experimentally derived datasets of limited size.

Several strategies exist for hyperparameter optimization, including manual tuning, Grid Search, Randomized Search, and Bayesian optimization. Among these approaches, Randomized Search has been shown to be more efficient than Grid Search for high-dimensional hyperparameter spaces, as it explores a broader range of configurations while requiring significantly fewer evaluations [120]. Rather than exhaustively testing all parameter combinations, Randomized Search samples hyperparameter values from predefined distributions, enabling effective exploration of the search space with reduced computational cost.

In this study, Randomized Search based hyperparameter tuning was applied uniformly in the XGBoost model to ensure consistency and fair comparison. For each model, a total of 500 random hyperparameter configurations (n_iter = 500) were evaluated using 5-fold cross-validation (cv = 5). Model performance during tuning was assessed using the negative Root Mean Squared Error (neg_root_mean_squared_error) as the optimization criterion, ensuring direct minimization of prediction error. To improve computational efficiency, parallel processing was enabled using n_jobs = -1, allowing utilization of all available processing cores. A fixed random state (random_state = 42) was employed to ensure reproducibility of the optimization results, while verbose = 1 was used to monitor the tuning progress.

The optimized hyperparameter sets obtained from this procedure were subsequently used to train the final models. The selected hyperparameters and their corresponding search ranges for each model are summarized in the following **Table 7.** This standardized and systematic tuning strategy ensures that all models operate under near-optimal conditions and enables a reliable performance comparison across different ensemble learning techniques.

Table 7: Hyperparameter tuning ranges and optimal values for XGBoost

Machine Learning Technique	Hyperparameters	Range Tested
XG Boost	Learning Rate	0.01 - 0.19
	Max Depth	3 - 10
	Subsample	0.4-0.6
	Colsample Bytree	0.4-0.6
	N Estimators	50-300

In summary, to ensure accurate predictions on unseen data, the input dataset is grouped based on specimen ID and split into an 80/20 training-to-testing ratio. An XGBoost base model is trained first, followed by a hyperparameter-tuned model. After evaluating the comparisons, the highest predictive accuracy is found in the base model. Consequently, this base model is deployed to predict the continuous stress-strain curves for the unseen data. Finally, the compressive modulus and compressive stress are extracted from these predicted curves and evaluated against the actual experimental data. Figure 9 represents the workflow for machine learning modelling for the present study.

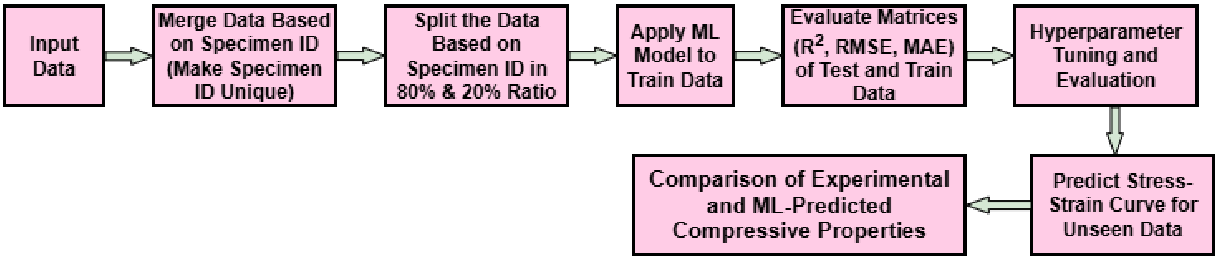

Figure 9. Workflow for machine learning modelling.

3.4. Chapter summary

This chapter first presents the modeling and finite element method (FEM) analysis processes of different lattice structures, which are demonstrated and analyzed using the L9 orthogonal array. Next, the investigation process for PLA-based filament simple cubic lattice structures is discussed, with particular emphasis on the effects of manufacturing parameters on the compressive behavior of these structures through the Taguchi L16 method. Subsequently, the standard measurement procedures for wood–PLA composite simple cubic lattice structures used in this study are described in order to investigate, for example, the effectiveness of manufacturing parameters through the response surface methodology (RSM) and central composite design (CCD) method. In addition to compressive properties, the standard procedures for evaluating physical properties such as water absorption, thickness swelling, contact angle, microscopic analysis, and scanning electron microscopy (SEM) analysis are also discussed in this chapter. Furthermore, the machine learning modeling and prediction processes are presented. Finally, the cell protocol measurement process is described, along with the different concentration levels and methods used.

4.RESULTS AND DISCUSSIONS

4.1. Different lattice structures and filaments effectiveness on the compressive behavior

4.1.2. Stress-strain curve analysis

After conducting the FEM analysis the force-displacement curves are obtained. The surface area is required to construct the stress-strain curve from the force-displacement curve, therefore, the surface area (A) is calculated from the lattice structure using a Python script. **Figure 10** is representing the stress-strain curve. From the stress-strain curves, it is evident that most of the DOEs exhibit the same trend.

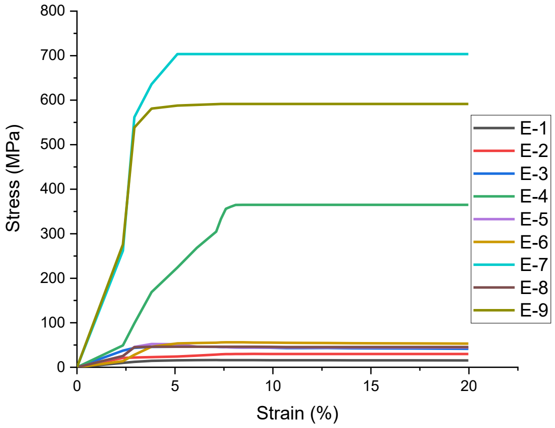

Figure 10: Stress-strain curve analysis at all DOEs.

Furthermore, two outcomes such as modulus of elasticity (E), effective strength (ES) are calculated from the stress-strain curves for all DOEs. Since, surface area is a significant factor for calculating mechanical properties from stress-strain curve, therefore, this study also considered surface area as an outcome. The obtained outcomes presented in Table III. The higher and lower outcomes in all considered outcomes are marked with a (*) sign. From Table III, it is apparent that the higher and lower values in E and ES are found in the same DOE, which reflects a co-relationship between E and ES. However, it is also evident that the surface area may vary even though the dimension for all lattice structures is identical (4mm x 4mm x 4mm).

Table 8: Overall outcomes in considered outcomes.

DOE SL.	**Strut diameter**	**Filament type**	**Lattice type**	**E (GPa)**	**ES (MPa)**	**A (mm^2)**
1	1	PLA	SC	0.421	16.19	7*
2	1	ABS	SC-BCC	0.224*	29.71*	7.21
3	1	Nylon	FCC	0.397	46.28	9.314
4	1.5	PLA	SC-BCC	2.094	360.64	10.2
5	1.5	ABS	FCC	0.269	52.2	13.74*
6	1.5	Nylon	SC	0.593	56.25	9.75

7	2	PLA	FCC	2.793*	703.67*	14.63
8	2	ABS	SC	0.271	46.27	12
9	2	Nylon	SC-BCC	2.944*	591.55*	12.807

4.1.3. Main effect plot analysis

In this study, the main effect plot analysis is performed on the designed DOE's in Fig. 5. Since the Taguchi method has a limitation of designing the experiment in categoric formation, therefore, the design is conducted as numeric formation where filament type 1 is for PLA, 2 is for ABS and 3 is for Nylon. Likewise, in lattice structure SC, SC-BCC and FCC are denoted by 1,2,3 respectively in main effect plot analysis **Figure 11**. As illustrated in the main effect plot analysis curve, it can be observed that with the increase of the strut diameter modulus of elasticity, effective strength increased drastically with the similar trend. Among all filaments, PLA filament provides higher outcomes in modulus of elasticity and effective strength. However, Nylon provides moderate outcomes while ABS provides lower outcomes in modulus of elasticity and effective strength. This indicates that PLA filament has better stiffness compared to nylon and ABS. Moreover, SC-BCC provides better performance in modulus of elasticity and effective strength. Furthermore, FCC exhibits moderate outcomes compared to SC. In terms of surface area, the surface area increases as the strut diameter increases (a similar increasing trend compared to the modulus of elasticity and effective strength). Additionally, filament type does not have any significant role on the surface area, while different lattice structures can provide different surface area.

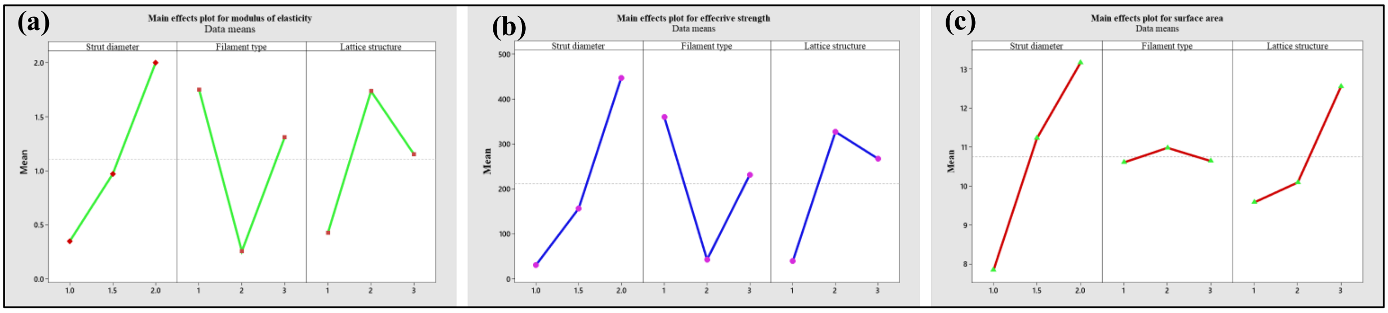

Figure 11: Main effect plot analysis of considered outcomes and factors.

4.1.4.ANOVA analysis

In this research, analysis of variance (ANOVA) is done to calculate the percentage of contribution on the considered factors and outcomes and to measure the significance level on the considered parameters. The confidence level in this analysis is set to 95%, which means that if a factor's p-value is less than or equal of 0.05 for a particular outcome, then that factor will be considered significant for that particular outcome. In **Table 9**, the percentage of contribution (POC) of each factor to their responses along with P-values are presented. P-values (which are less than 0.05) is marked with (*) sign. From **Table 9**, it is apparent that strut diameter is the most crucial parameter for E, ES and A with POC being 39.84%,46.80% and 72.54% and P-value of 0.042,0.066 and 0.021 respectively. However, filament type also has a significant role in the lattice structure's outcomes which can contribute about 33.85%, 26.19% and 0.43% to E, ES, and A, respectively. Although different lattice types did not show any P-value less than of 0.05, however, it could significantly affect ES and A with POC 23.66% and 25.37%, respectively.

Table 9: POC and P-values of considered factors and their responses.

Factors	Modulus of elasticity (E)		Effective strength (ES)		Surface area (A)	
	POC	P-value	POC	P-value	POC	P-value
Strut diameter	39.84%	0.042*	46.80%	0.066	72.54%	0.021
Filament type	33.85%	0.049*	26.19%	0.111	0.43%	0.787
Lattice type	1.73%	0.066	23.66%	0.112	25.37%	0.058

4.1.5. Chapter summary

This chapters analyzes the impact of strut diameters on the mechanical properties of three different lattice structures along with three different polymeric filaments. The analysis is generated in FEM software Abaqus. Furthermore, the obtained outcomes from FEM are analyzed in a data analysis software. Since fabrication and real experimentation is a time-consuming task, this investigation will help future researchers and the FDM industry to understand the mechanical performance of polymeric lattice structures. In addition, this investigation revealed that different structures and strut diameters can crucially affect the overall mechanical performance which can be considered before conducting actual experimentation. Moreover, investigation also revealed that, among three filaments (PLA, ABS and Nylon), PLA exhibits better mechanical properties than ABS and Nylon. However, considering surface area and design suitability SC lattice is suitable with moderate effective strength.

4.2. Effect of manufacturing parameters on the PLA-based SC lattice

4.2.1. Stress-strain curve analysis in PLA-based SC lattice

After conducting the compression test (based on DOE), the obtained results (load and displacement) are plotted in **Figure 12** (a) and a comparison of the structures' mechanical performance from the initial stage to ultimate failure is highlighted, similar to the literature [121]. From the load vs displacement curve, stress and strain for each DOE are calculated and presented in **Figure 12** (b). This load-displacement and stress-strain curves are generated from an average of 5 samples (close to the average result plotted on the curve). The stress-strain curve from **Figure 12** (b) shows that all DOEs have provided a similar trend as expected from the lattice structure. For example, the fracture strain in all DOEs ranges from 0.53 to 0.60. Likewise, the stress-strain curve exhibits a similar trend in all DOE.

Experimental phenomena observed during the test are presented in **Figure 13** which also demonstrates the layer wise collapse of the lattice structure. The serrate shapes in the load-displacement curve **Figure 12** (a) indicate the initial buckling in **Figure 13**(b). Then collapsed in the 1st, 2nd, and 3rd layers can be seen in **Figure 13** (c), **Figure 13** (d), and **Figure 13** (e). Finally, the ultimate failure is shown in **Figure 13** (f). Similar results are also observed in the literature for lattice structure [97]. This study also suggests the possible reason for this discontinuous graph during the compression test.

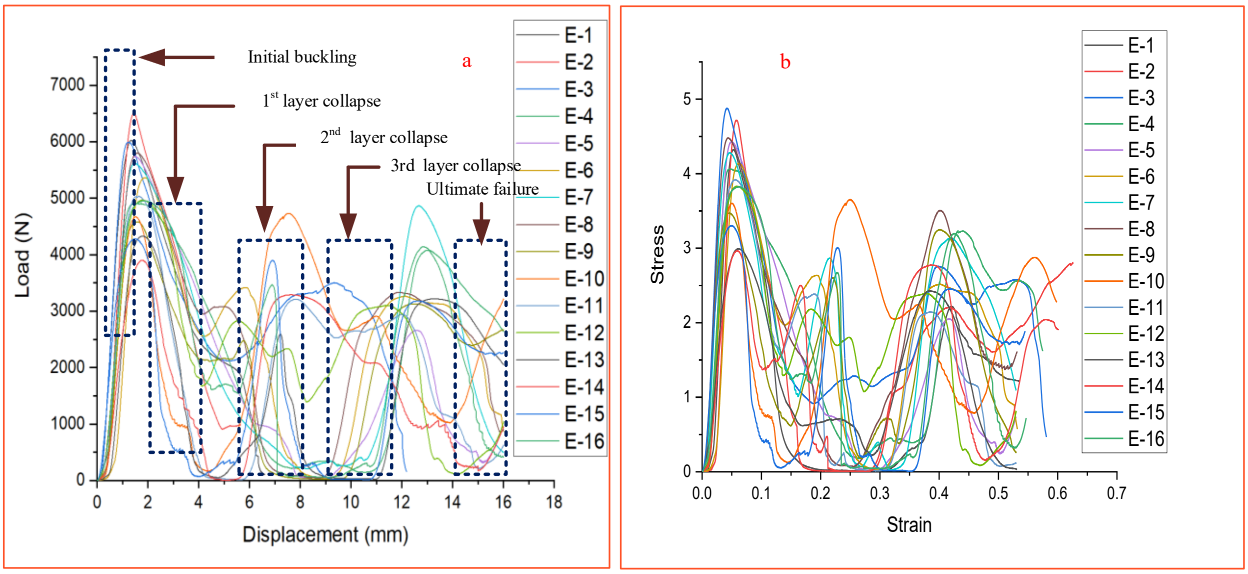

Figure 12: (a) load vs displacement curve, **(b)** stress vs strain curve for all DOE.

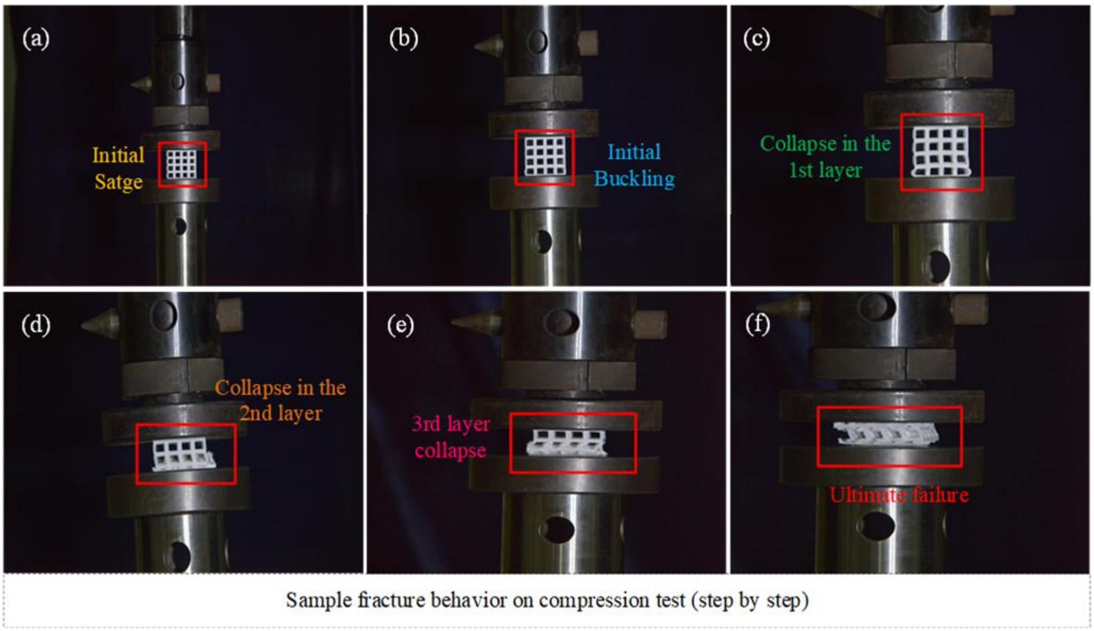

Sample fracture behavior on compression test (step by step)

Figure : 13 Deformation patterns in lattice structure.

The mechanical properties are calculated from the stress strain curve for all DOE and the outcomes are–enlisted in Table 10. In general, higher outcomes in modulus of elasticity and compressive strength reflect the better stiffness of the material. Interestingly, this study indicates that the modulus of elasticity and compressive strength has a direct correlation. For this research, the maximum modulus of elasticity and compressive strength is found at DOE (E-3) for 0.1 mm layer height, 205°C, 50 mm/s printing speed, and 60°C bed temperature. In contrast, the minimum modulus of elasticity and compressive strength is obtained at DOE (E-14) in the combination of 0.25 mm layer height, 200°C, 50 mm/s printing speed, and 50°C bed temperature. By contrast, the maximum fracture strain is observed at DOE (E-2) in combination with 0.1 mm layer height, 200°C printing temperature, 40 mm/s printing speed, and 55°C bed temperature, and for minimum number, the combination is 0.15 mm layer height, 200°C printing temperature,30 mm/s printing speed, and 65°C bed temperature. For modulus of toughness, the maximum outcome is observed at DOE (E-4) with the combination of 0.10 mm layer height, 210°C printing temperature,60 mm/s printing speed 65°C bed temperature. In comparison, the minimum values are found at DOE (E-1) with the combination of 0.10 mm layer height, 195°C printing temperature,30 mm/s printing speed 50°C, and bed temperature. The elaborations and possible reasons for each maximum and minimum outcome have been explained onward.

Table 10: Detailed experimental outcomes based on DOE

DOE SL.	Modulus of elasticity (E)	Compressive strength	Fracture strain (%)	Modulus of toughness (KJ/m^3)
E-1	160.409	4.301	54.222	670.056*
E-2	168.617	4.605	60.058*	954.956
E-3	177.089*	4.613*	54.142	994.135
E-4	161.576	3.986	59.739	1104.528*
E-5	160.693	4.281	53.479	769.913
E-6	150.166	4.140	53.165*	872.231
E-7	162.139	4.296	54.226	1075.484
E-8	165.122	4.460	53.281	1009.099
E-9	124.026	3.485	54.133	914.194
E-10	134.046	3.681	59.611	1052.974
E-11	138.613	3.924	55.955	845.610
E-12	132.436	3.834	57.683	921.473
E-13	107.750	3.229	55.698	754.068
E-14	100.721*	3.222*	59.230	748.912
E-15	121.079	3.296	58.157	675.589
E-16	124.241	3.791	56.10	913.628

4.2.2. Comparison with responses in PLA-based SC lattice

As discussed earlier, the modulus of elasticity has a correlation with compressive strength, which is also apparent from **Figure 14**. As the modulus of elasticity increases, the compressive strength also increases.

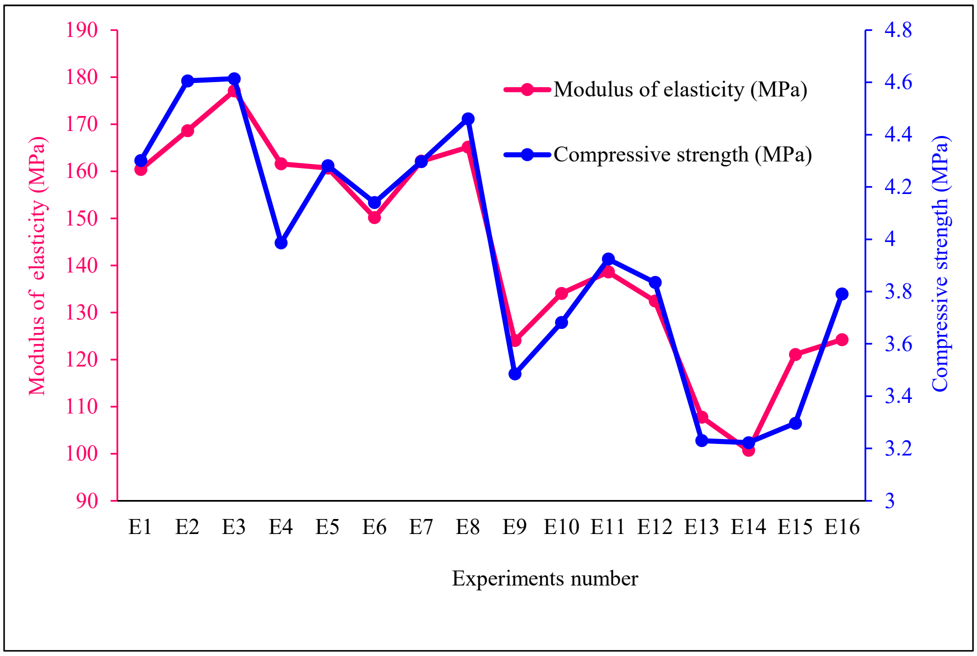

Figure 14: Modulus of elasticity vs. compressive strength.

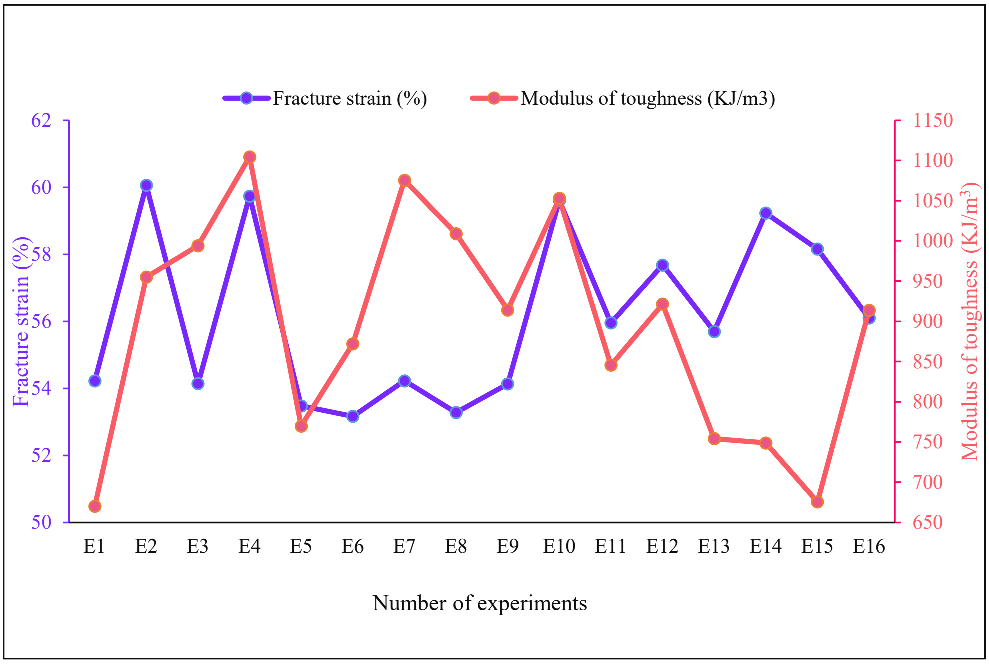

Figure 15: Fracture strain (%) vs. modulus of toughness.

However, in the comparison **Figure 15**, we can not establish a co-relationship between fracture strain (%) and modulus of toughness. For, DOE numbers (E-1, E-2, E-4, E-5, E-7, E-8, E-10, E-11, E-12, E-13, E-15) as fracture strain (%) increases the modulus of toughness also increase. Similarly, with the decrement of fracture strain (%) in these DOE, the modulus of toughness also decreases. On the other hand, in these five DOE numbers (E-3, E-6, E-9, E-14, E-16), the outcomes increment and decrement trends are vice versa.

4.2.3. ANOVA analysis in PLA-based SC lattice

ANOVA analysis has been generated to investigate the percentage of contribution (PC) to each parameter of the responses. In this research, the confidence level of ANOVA analysis was set as 95%. As a result, any parameter providing P_{values} less than or equal to 0.05 (α-alpha value) will be considered a significant parameter in this study. Significant parameters for this analysis (those with P_{values} less than or equal to 0.05) are marked with (*). ANOVA analysis with PC of each parameter for elasticity, compressive strength, fracture strain, and toughness modulus is described in the table below;

Table 11: PC and P_{values} from ANOVA analysis.

Parameters	**Modulus of elasticity**		**Compressive strength**		**Fracture strain**		**Modulus of toughness**	
	P_{values}	**PC**	P_{values}	**PC**	P_{values}	**PC**	P_{values}	**PC**
Layer height	0.000*	86.748%	0.000^{*}	75.34%	0.521	0.09%	0.039^{*}	15.468%
Printing temperature	0.103	2.883%	0.186	2.96%	0.474	4.3248%	0.010^{*}	26.79%
Printing speed	0.617	0.2416%	0.145	3.66%	0.413	5.689%	0.013^{*}	25.045%
Bed temperature	0.806	0.05%	0.316	1.6442%	0.931	0.06%	0.459	1.6634%

Table 11 shows that the layer height is the most influential parameter for modulus of elasticity with P_{values} less than 0.05 and PC 86.748%. However, other parameters such as printing temperature, printing speed, and bed temperature provided insignificant P_{values} with PC 2.883%,0.2416%, and 0.05%, respectively.

In the case of compressive strength, layer height is also the most crucial parameter with P_{values} less than 0.05 and PC 75.34%. The other parameters have no significant role in compressive strength. Moreover, the PC for printing temperature, printing speed, and bed temperature is 2.96%, 3.66%, and 1.64%, respectively.

Although, in other responses (modulus of elasticity and compressive strength), the layer height showed a satisfactory PC and P_{values} (in Table 11); however, there is no significant parameter in the range of 0.05 (α-alpha value) in terms of fracture strain (%). Moreover, the most important parameters according to PC for fracture strain (%) are followed by printing speed 5.689%, printing temperature 4.3248%, layer height 0.09%, and bed temperature 0.06%.

Interestingly, three parameters provide satisfactory P_{values} with less than 0.05 for modulus of toughness. The significant parameters are followed by printing temperature with PC 26.79%, printing speed with PC 25.045%, and layer height with PC 15.468%. However, bed temperature showed a negligible contribution to the modulus of toughness with PC 1.6634%.

4.2.4. Parameters optimizations in PLA-based SC lattice

In order to estimate and optimize the better responses for printing parameters, the obtained outcomes are further analyzed through signal-to-noise ratio (S/N). For the current calculation, it is determined for all responses, larger is better. Higher values of modulus of elasticity and compressive strength reflect better material stiffness. Likewise, higher fracture strain values and toughness modulus induce large deflection rates and maximum energy absorption capacity in the material. The equation for the S/N ratio (considering larger is better) is presented below;

$$S / N = -10\log_{10}[\frac{1}{n}\Sigma(\frac{1}{y_{ij}^{2}})] \tag{1}$$

Here, y_{ij} is the mean of the response values, and n is the number of responses. The predicted and optimal responses are listed in Table 12 (larger responses are marked with a * symbol).

Table 12: S/N ratios for all parameters and outcomes

	Modulus of elasticity					**Compressive strength**				
Factors	**Level1**	**Level2**	**Level3**	**Level4**	**Delta and Rank**	**Level1**	**Level2**	**Level3**	**Level4**	**Delta and Rank**
Layer height	44.44*	44.05	42.42	41.06	3.38,1	12.81*	12.66	11.43	10.57	2.24,1
Printing temperature	42.69	42.67	43.41*	43.21	0.75,2	11.58	11.77	12.04	12.06*	0.48,4
Printing speed	43.09	43.19*	42.81	42.89	0.38,4	12.12*	11.98	11.82	11.55	0.57,3
Bed temperature	42.70	43.09	43.38*	42.81	0.68,3	11.79	12.08	12.20*	11.39	0.81,2
	Fracture strain (%)					**Modulus of toughness**				

Factors	**Level1**	**Level2**	**Level3**	**Level4**	**Delta and Rank**	**Level1**	**Level2**	**Level3**	**Level4**	**Delta and Rank**
Layer height	35.11	34.57	35.09	35.16*	0.59,1	59.23	59.31	59.38*	57.71	1.66,2
Printing temperature	34.71	35.26*	34.90	35.06	0.55,2	57.76	59.09	58.93	59.86*	2.11,1
Printing speed	34.78	35.16*	34.83	35.16*	0.38,3	58.27	58.30	59.18	59.87*	1.60,3
Bed temperature	35.01*	34.99	34.93	35.00	0.08,4	58.48	58.94	59.34*	58.87	0.85,4

According to the S/N ratio analysis in **Table 12**, the modulus of elasticity can be best achieved when the combination is 0.1 mm layer height, 205 °C printing temperature, 40 mm/s printing speed, and 60°C bed temperature. After combining these parameters, 3d printed samples (five) are again made, and compression tests are performed to compare the results further. In this study, the best outcomes from DOE, software prediction (SP), and experimental results (S/N predicted parameter-based experimental results) are compared in Table 13. Interestingly, there is a negligible difference (0.49%) between the S/N prediction and the S/N predicted parameter-based experimental result. However, this study also compares experimental results (based on S/N combination) with the best outcomes (for modulus of elasticity) from DOE, and the difference is also insignificant (2.38%). This means that the prediction of the modulus of elasticity has provided satisfactory outcomes. Likewise, S/N predictions for compressive strength yield the best results at 0.1 mm layer height, 210 °C printing temperature, 30 mm/s printing speed, and 60 °C bed temperature. Similar predicted parameters (compared to the modulus of elasticity) are also observed for layer height and bed temperature. After considering these parameters and performing the experiment, the results reveal that the difference between the software calculation and the experimental result is 6.74%. However, the difference between the DOE (E-3) and software-predicted results is about 1.5%, which is significantly smaller. Regarding fracture strain (%), S/N ratio analysis predicts the best combination at 0.25 mm layer height, 200°C printing temperature, and 50°C bed temperature. However, the software provides two estimates for printing speed such as 40mm/s and 60mm/s. Later, based on these two combinations, the compression test is carried out. Overall, these two combinations provide an expected result similar to the software prediction with negligible differences (5.08% and 3.63%) for print speeds of 40 and 60 mm/s, respectively. As illustrated in **Table 12**, the best-optimized parameters of S/N analysis for modulus of toughness are 0.20 mm layer height, printing temperature 210 °C, printing speed 60 mm/s, and bed temperature 60 °C. After calculating the modulus of toughness based on these parameters, it is evident in **Table 13** that the experimental results have significantly decreased by 21.15% compared to the software's predicted results. Such deviations are sometimes observed in this type of analysis, as discussed in this study[122] .However, if we compare this experimental result (based on the S/N predicted parameter) with the DOE (E-4) result in **Table 13**, the difference is negligible (6.04%) and in satisfactory condition.

Table 13: Comparison in DOE, software prediction and experimental outcomes

Results	DOE	Software prediction	Experimental
Modulus of elasticity	177.09 MPa (E-3)	182.24 MPa	181.36 MPa
Compressive strength	4.61 MPa (E-3)	4.69 MPa	4.38 MPa
Fracture strain (%)	60.06% (E-2)	60.46 % (at printing speed 40 and 60 mm/s)	57.46% at (40 mm/s) 58.3023% at (60 mm/s)
Modulus of toughness	1104.53 KJ/m^3 (E-4)	1173.26 KJ/m^3	948.8625 m^3

4.2.5. Stress-strain curve analysis in PLA-based SC lattice

The stress-strain curves based on the optimized parameters for each response are plotted in **Figure 16**. In the optimized stress-strain graph, E represents the modulus of elasticity, CS for compressive strength, MT for the modulus of toughness, and FS for fracture strain percentage. Moreover, FS-40 and FS-60 describe the fracture strain when the printing speed is 40 mm/s and 60 mm/s, respectively.

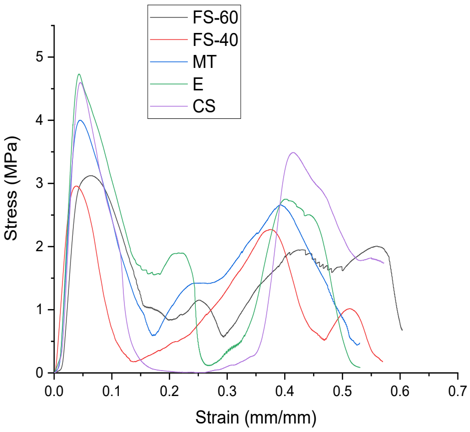

Figure 16: Stress-strain curves for optimized responses.

4.2.6. SEM analysis in PLA-based SC lattice

The microstructure of the lattice structures has significant contributions to the mechanical properties. Therefore, SEM analysis has been conducted in this research to find out possible reasons and to clarify the dissimilarities between the responses. In addition, to reduce the defects and enhance the mechanical properties, SEM analysis also plays a crucial role[48]. Hence, SEM analysis is carried out on the responses of modulus of elasticity, compressive strength, and modulus of toughness and compared between DOE maximum and minimum outcomes with optimized responses. However, this work did not consider the fracture strain (%) for the SEM analysis because fracture strain (%) does not change remarkably with printing parameters (ranging from 53% to 60%). **Figure 17** (a-d) represents the DOE (E-3), which exhibits the maximum outcomes, and **Figure 17** (e-h) represents the DOE (E-14), which shows the minimum results in modulus of elasticity and compressive strength, respectively. In SEM Figure 17 (a-d), DOE (E-3) with low layer height (0.10 mm), medium printing temperature (205°C), printing speed (50 mm/s), and bed temperature (60°C) shows low manufacturing defects such as small gaps between two adjacent layers, and fewer holes.

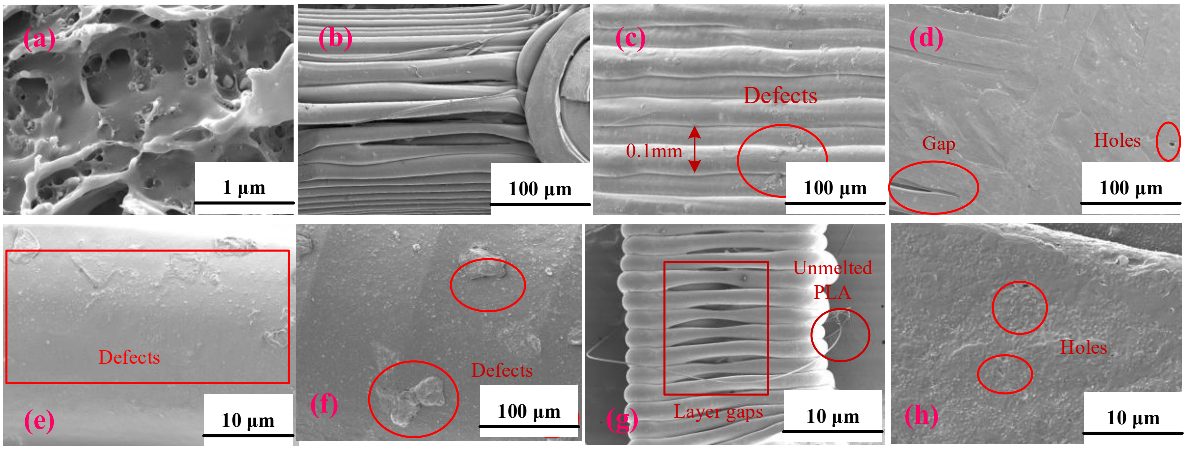

Figure 17 SEM micrographs of the 3d printed lattice surface, **(a-d)** for DOE (E-3), **(e-h)** for DOE (E-14) at different magnification and resolution scales.

However, it is visible in DOE (E-14) that there are major manufacturing defects such as unmelted filaments, improper extruded material on the surface, many holes, and especially excessive gaps between layers, which might be responsible for giving minimum outcomes in modulus of elasticity and compressive strength. This is particularly true for most of the AM fabricated parts. For example, as the number of holes increased in the AM-manufactured parts, the parts experienced the earliest catastrophic failure[123,124].

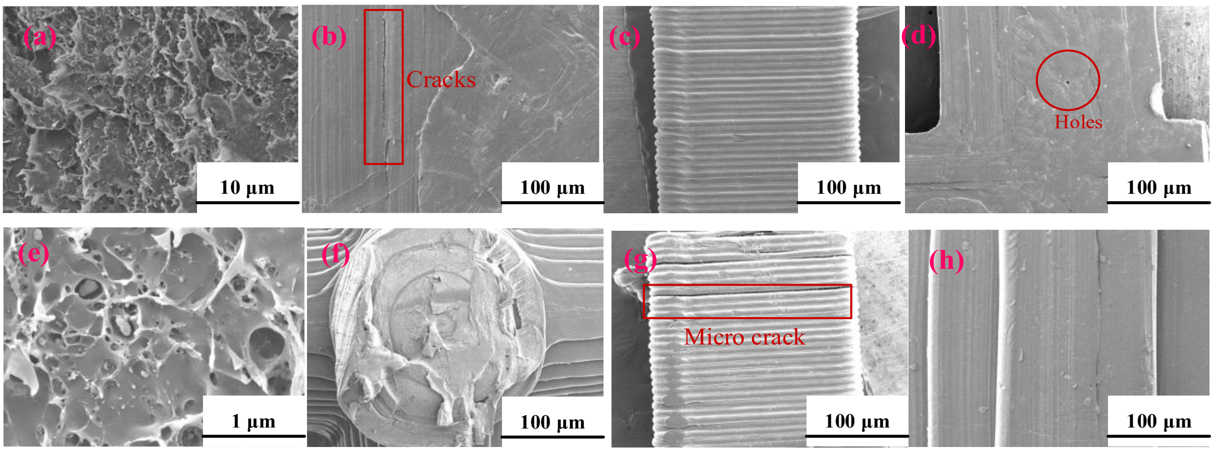

Figure 18 SEM micrographs of the 3d printed lattice surface, **(a-d)** optimized modulus of elasticity, **(e-h)** optimized compress strength at different magnification and resolution scales.

Moreover, a possible explanation would be (for DOE (E-14)) the high layer height (0.25 mm), with moderate printing temperature (200°C), printing speed (50 mm/s), and bed temperature (50°C) make this unsatisfactory and undesirable manufacturing defects, which lead to minimal results in modulus of elasticity and compressive strength.

As shown in **Figure 18** (a–d), the optimized responses provide fewer manufacturing defects (fewer voids, holes, and gaps between two layers) than DOE (E-3). Although the software estimates (S/N analysis) similar parameters to obtain better results than DOE (E-3) in modulus of elasticity, for example, layer height (0.1 mm), printing temperature (205 °C), bed temperature (60 °C), however, the only exception found at printing speed (50 mm/s and 40 mm/s for DOE (E-3) and optimized modulus of elasticity, respectively). SEM analysis indicates that the lowest printing speed (40 mm/s) can provide better results with fewer manufacturing defects for the modulus of elasticity than the highest printing speed (50 mm/s). In terms of compressive strength, SEM analysis shows similar characteristics in optimized response and DOE (E-3). Interestingly, similar parameters have been found in layer height and bed temperature. However, the exceptions are printing temperature (205°C for DOE (E-3) and 210°C for the optimized response, respectively) and printing speed (50 mm/s for DOE (E-3) and 30 mm/s for the optimized response, respectively). The main reason for this better outcome in compressive strength would be the maximum printing temperature (210°C) and low printing speed (30 mm/s), which provide fewer manufacturing defects (holes, voids and layer gaps) and better extrusion. Similar observations (in results) were found and demonstrated in this literature for 3D-printed parts of PLA and PTEG materials[125].

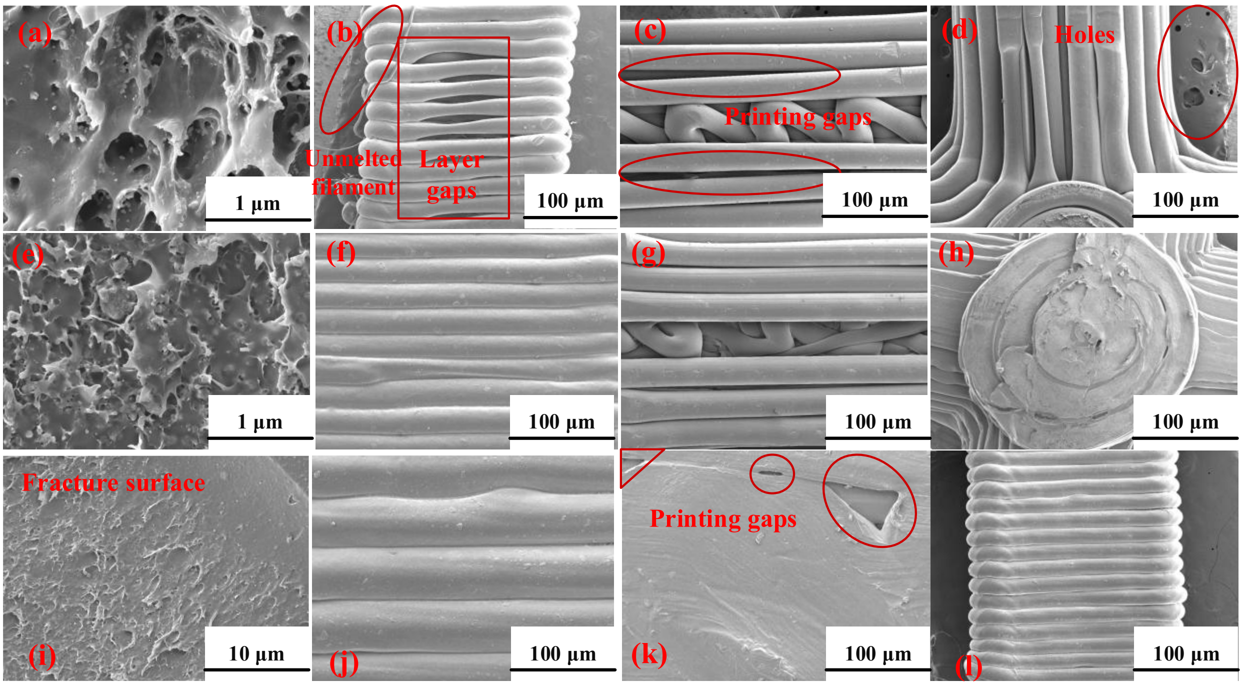

Figure 19 SEM micrographs of the 3d printed lattice surface, **(a-d)** minimum modulus of toughness DOE (E-1), DOE (E-4) **(e-h)** maximum modulus of toughness, **(i-l)** optimized modulus of toughness at different magnification and resolution scales.

Furthermore, a comparison is also performed by SEM analysis between DOE (E-1) (minimum modulus of toughness), DOE (E-4) (maximum modulus of toughness), and optimized responses for modulus of toughness in **Figure 19**. Although the optimized responses in modulus of elasticity and compressive strength give satisfactory and expected behavior (less manufacturing defects such as voids, holes, and gaps) compared to DOE, however, an exceptional phenomenon is observed for modulus of toughness. For example, DOE (E-4) performs better than the optimized response. Most likely, the small layer height (0.1 mm) on the DOE (E-4) is the main factor that makes this difference with the optimized response. However, if we compare DOE (E-1) and DOE (E-4), the logical explanation would be lower printing temperature (195°C) and bed temperature (50°C) cause many defects such as excessive gaps, unmelted filaments, a lot of holes, which prevent the structure from carrying excessive loads. As a result, the lattice structure collapses earlier and provides less energy absorption capacity in DOE (E-1).

4.2.7. Application of PLA-based SC lattice

This section designs a lattice scaffold and prints with optimized parameters of layer height 0.1mm, printing temperature (210°C), printing speed (40 mm/s), and bed temperature (60°C) to remove the manufacturing defects. Moreover, an SEM analysis is conducted on the 3D printed scaffold (application), where minimal manufacturing defects have been observed. The printed scaffold and SEM analysis have been presented in **Figure 20**. Since PLA is non-toxic, biodegradable, and biocompatible (with better body fluid interaction), this proposed design and optimized parameters can be used for future investigation in biomedical applications such as in rapid prototyping, educational purpose, bone regeneration and bone replacement, especially in fracture zones, etc.

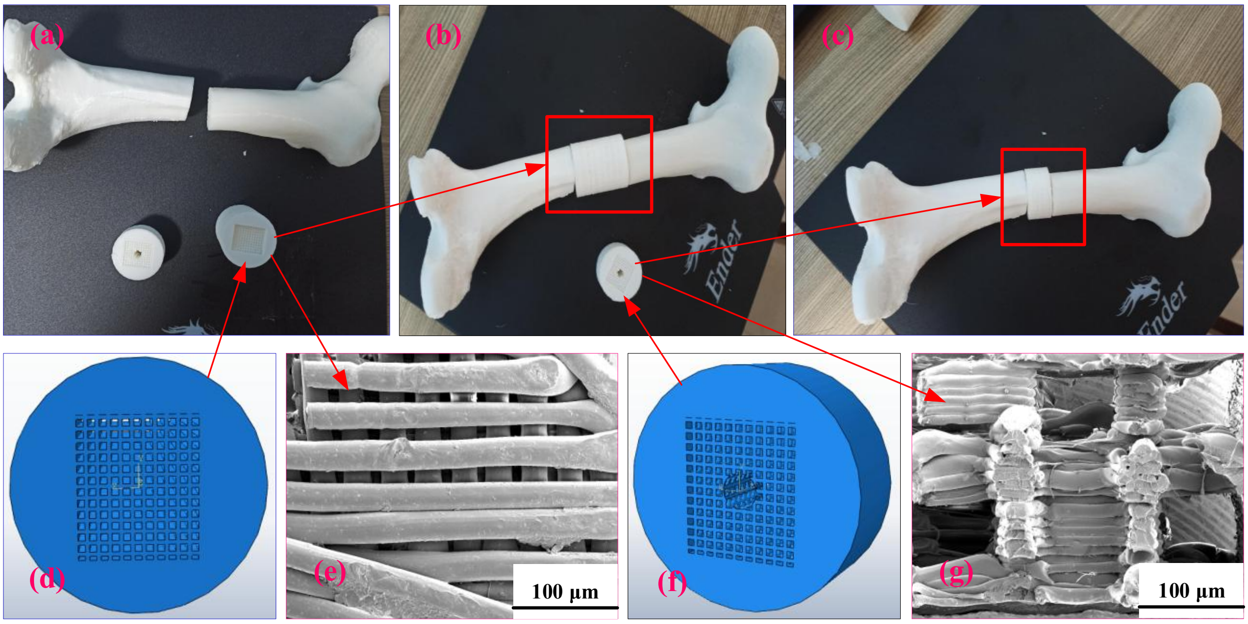

Figure 20 (a-c) 3d printed PLA scaffold from normal lattice cube structure with hole and without hole, designed scaffold in ABAQUS (d) without hole and (f) with hole, (e) and (g) SEM analysis on the 3d printed scaffold.

4.2.8. Chapter summary

PLA filament is a widely adopted FDM printing material in biomedical and clinical applications. In this chapter, a set of experiments have been conducted to determine the influences of manufacturing parameters on the compressive behavior of a PLA lattice cubic structure. The results revealed that manufacturing parameters could significantly influence mechanical properties. Aside from this, a correlation has been developed among considered outcomes. Additionally, this study also generates different statistical simulations and SEM analyses to improve the mechanical properties with fewer manufacturing defects. Moreover, a prototype of the lattice bone scaffold is designed and fabricated from PLA based SC lattice structures which can be used in educational purpose, bone implantation and other biological investigations.

4.3. Effect of manufacturing parameters on the wood -PLA-based SC lattice scaffold

4.3.1 Stress-strain curve analysis on wood-PLA composite lattice scaffold

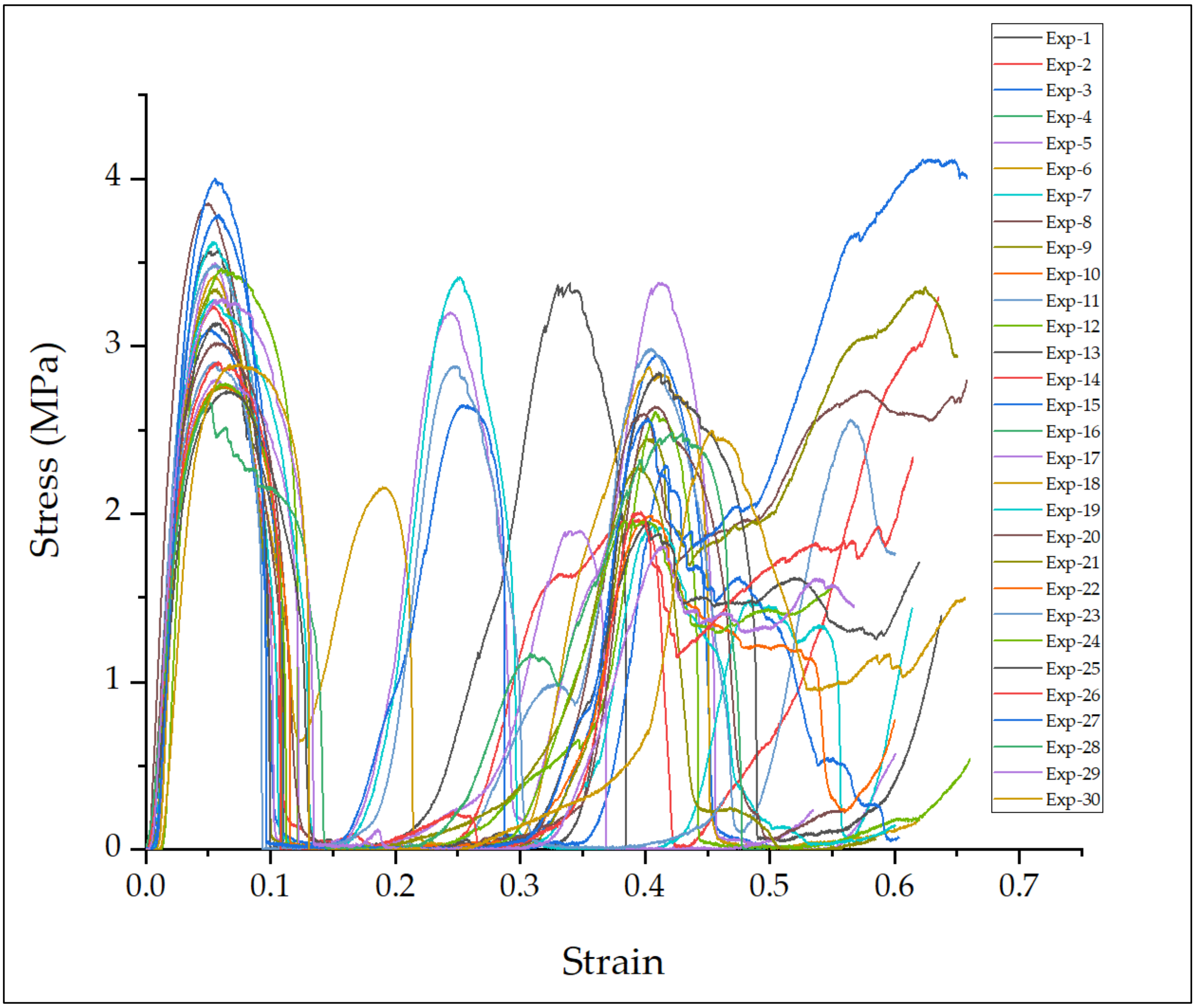

Figure 21: Stress–strain curve analysis for DOE-1 to DOE-30.

In **Figure 21**, the stress–strain behaviour of wood–PLA composite lattice structures is depicted based on the Design of Experiments from DOE-1 to DOE-30. The variations observed among the thirty curves clearly demonstrate that the stress–strain response of the wood–PLA composite largely depends on the processing parameters. In the stress–strain curve, the region up to the first peak stress represents the elastic region, the peak stress corresponds to the compressive strength, while the post-peak region represents failure after the peak stress.

Experiments such as DOE-1, DOE-4, DOE-10, DOE-14, DOE-16, and DOE-18, with moderate layer height (0.2 mm) and minimum infill density (85%), provide a stable elastic region and a balanced peak stress in the stress–strain curve shown in **Figure 21**. On the other hand, DOE-2, DOE-3, DOE-6, DOE-7, DOE-9, and DOE-15, printed with a lower layer height (0.1 mm) and higher nozzle temperatures (up to 215°C), show an improved initial slope in the elastic region, mainly due to enhanced interlayer bonding and better filament fusion.

Particularly, the influence of infill density is observed in DOE-5, DOE-6, DOE-9, DOE-17, DOE-26, and DOE-28, where 100% infill density provides higher peak stress and delayed collapse compared to lower infill densities such as DOE-2, DOE-7, DOE-22, and DOE-29. For example, DOE-29, with 55% infill density, exhibits earlier collapse despite having moderate layer height (0.2 mm), moderate printing speed, and nozzle temperature. This specimen could not support the overall lattice structure due to a lack of internal support.

However, nozzle temperature also significantly affects the stress–strain behaviour of the wood–PLA lattice composite. For instance, DOE-1 was printed at 185°C compared to DOE-20 at 225°C. Higher temperature promotes stronger interlayer adhesion in the composite, reduces voids in the structure, and results in smoother transitions in the stress–strain response. However, excessively high temperatures may also cause unintentional difficulties such as imperfect bonding, poor adhesion, and distortion of the intended structure.

In terms of printing speed effectiveness, it can be observed that moderate speeds (40 mm/s), such as in DOE-5, DOE-15, DOE-17, and DOE-24, provide more stable stress–strain curves than DOE-11 and DOE-12, which were printed at higher speeds of 60–70 mm/s. This is possibly because increased printing speed reduces bonding time, which may introduce slight inconsistencies in the internal structure and earlier drops in the stress–strain curve.

Larger layer heights (0.3 mm) generally reduce stiffness due to thicker filament deposition and comparatively weaker bonding between layers, as seen in DOE-17 and DOE-26. Although these two experiments consist of high infill density (100%), the thicker layers imbalance the overall structure. On the other hand, lower layer height may improve mechanical integrity; however, residual stresses may increase depending on the temperature, speed, and infill density combinations.

4.3.2. Compressive strength and compressive modulus analysis of wood-PLA composite lattice scaffold

Table 14 presents the 30 Design of Experiments (DOE) trials conducted to evaluate the effect of key FDM process parameters on the compressive strength and compressive modulus of wood–PLA composite lattice structures. The reported results represent the average values obtained from three tested samples. Among the experimental runs, the highest compressive strength of 4.11 MPa was achieved at a layer height of 0.1 mm, nozzle temperature of 215°C, printing speed of 40 mm/s, and infill density of 70%. Similarly, the maximum compressive modulus of 157 MPa was obtained at a layer height of 0.1 mm, nozzle temperature of 195°C, printing speed of 40 mm/s, and infill density of 70%. In contrast, the lowest compressive strength of 2.66 MPa and compressive modulus of 76 MPa were observed at a layer height of 0.3 mm, printing speed of 60 mm/s, nozzle temperature of 195°C, and infill density of 100%. The highest and lowest values of compressive strength and modulus are highlighted in Table 4 using an asterisk (*) for clarity.

Table 14: Experimental design and corresponding compressive strength and compressive modulus results.

Sl no.	Layer height (mm)	Printing speed mm/s	Nozzle temperature (°C)	Infill Density (%)	Compressive strength (MPa)	Compressive modulus (MPa)
1	0.2	50	185	85	3.56 MPa	110 MPa
2	0.1	60	215	70	3.23 MPa	124 MPa
3	0.1	60	215	100	3.06 MPa	113 MPa
4	0.2	50	205	85	3.27 MPa	111 MPa
5	0.1	40	195	100	3.48 MPa	117 MPa
6	0.1	60	195	100	3.42 MPa	112.66 MPa
7	0.1	60	195	70	3.62 MPa	139 MPa
8	0.06	50	205	85	3.85 MPa	140 MPa
9	0.1	40	215	100	3.35 MPa	125 MPa
10	0.2	50	205	85	3.27 MPa	111 MPa
11	0.2	70	205	85	3.48 MPa	132 MPa
12	0.2	30	205	85	3.46 MPa	139 MPa
13	0.2	50	205	50	3.13 MPa	108 MPa
14	0.2	50	205	85	3.27 MPa	111 MPa
15	0.1	40	195	70	**4.00* MPa**	**157* MPa**
16	0.2	50	205	85	3.27 MPa	111 MPa
17	0.3	40	195	100	2.80 MPa	91.44 MPa
18	0.2	50	205	85	3.27 MPa	111 MPa
19	0.2	50	205	85	3.27 MPa	111 MPa

20	0.2	50	225	85	3.02 MPa	85 MPa
21	0.3	40	215	100	2.76 MPa	93 MPa
22	0.3	60	215	70	2.77 MPa	83 MPa
23	0.3	40	195	70	2.9 MPa	102 MPa
24	0.3	40	215	70	2.77 MPa	80.66 MPa
25	0.3	60	195	70	2.72 MPa	79.66 MPa
26	0.3	60	215	100	2.9 MPa	80 MPa
27	0.1	40	215	70	**4.11* MPa**	**139* MPa**
28	0.3	60	195	100	**2.66* MPa**	**76* MPa**
29	0.2	50	205	55	3.2 MPa	120 MPa
30	0.32	50	205	85	2.89 MPa	84 MPa

It is clearly evident from **Table 14** that layer height produces the strongest effect on the compressive performance of the wood–PLA lattice composite. Experimental results show that lower layer heights in the range of 0.06–0.1 mm significantly improved compressive strength, reaching the maximum value of 4.11 MPa. A similar trend was observed for compressive modulus, as the highest modulus values among the 30 DOE trials were also obtained at low layer heights. This improvement can be attributed to enhanced interlayer fusion, reduced void formation, and stronger bonding between deposited filaments. Conversely, increasing the layer height to 0.3–0.32 mm substantially reduced compressive strength to approximately 2.6–2.9 MPa and compressive modulus to around 76–80 MPa. This reduction reflects poorer interlayer adhesion, insufficient fusion, weaker fiber–matrix interaction, reduced load-bearing capacity, and earlier structural failure during compression.

In terms of printing speed, lower speeds generally provided better compressive strength and stiffness compared to higher speeds. For example, DOE-15 and DOE-27 achieved the highest compressive strength (4.11 MPa) and modulus (157 MPa) when the printing speed was 40 mm/s. However, when the printing speed increased to 60–70 mm/s, compressive strength and modulus decreased to approximately 3.23–3.62 MPa and 111–139 MPa, respectively. This reduction is mainly due to faster cooling rates at higher speeds, which limit polymer diffusion and weaken interlayer bonding. Nevertheless, this trend is not strictly uniform across all cases. An exception is observed in DOE-11, where despite the highest speed of 70 mm/s, the lattice exhibited moderate compressive strength (3.48 MPa) and modulus (132 MPa). This behavior may be because of the combined influence of a moderate nozzle temperature (205°C) and an infill density of 85%, which likely promoted improved material fusion and interfacial bonding.

With respect to nozzle temperature, most DOE's conducted within a moderate temperature range of 195–205°C produced relatively stable and higher modulus values, reaching up to 140–157 MPa. However, when the nozzle temperature increased to 225°C, the compressive modulus dropped significantly to approximately 85 MPa. This decline suggests that excessive thermal input may cause degradation of the wood–PLA composite, reduce dimensional stability, and over-soften the PLA matrix, ultimately weakening the lattice structure. A similar influence of nozzle temperature on the mechanical performance of NFRC composites has also been reported in previous studies [126].

Finally, infill density also influenced compressive behavior by controlling the internal structural support of the lattice. Specimens fabricated with 100% infill demonstrated moderate compressive strength and modulus in the range of 3.35–3.48 MPa and 117–125 MPa, respectively. However, intermediate infill levels such as 85% often provided improved stiffness and strength compared to full infill, likely due to an optimized balance between internal support and structural flexibility. Interestingly, lower infill density of 70% produced the highest compressive strength and modulus in several cases, particularly in DOE-15 and DOE-27. A similar phenomenon regarding infill density was observed in this research, where the 50% infill density exhibited higher fatigue performance than the 90% and 100% infill configurations in lattice structures [127].This indicates that an optimal infill level may exist where the lattice geometry effectively distributes compressive loads while maintaining efficient bonding and reduced stress concentration.

Overall, the DOE results confirm that compressive performance in FDM-printed wood–PLA lattice composites is governed by the combined effects of layer height, printing speed, nozzle temperature, and infill density, with layer height being the most dominant parameter affecting both compressive strength and stiffness.

4.3.3. ANOVA analysis on wood-PLA SC lattice composite scaffold

In this research, analysis of variance (ANOVA) was performed to evaluate the influence of the printing parameters on compressive strength. A confidence level of 95% was selected; therefore, any parameter with a P-value less than 0.05 was considered statistically significant for the investigated responses, including compressive strength and elastic modulus. Furthermore, the percentage contribution (PC) of each parameter to the response was determined using the ratio of the sum of squares of each factor to the total sum of squares, multiplied by 100. This method is commonly used to quantify the relative influence of each parameter on the response, as reported in previous studies [122]. Table 15 presents the ANOVA results for compressive strength along with the calculated percentage contributions of the investigated parameters.

Table 15: ANOVA analysis for compressive strength.

Source	Sum of squares	df	Mean Square	F-value	P-value	Significance	Percentage of contributions
Model	3.11	4	0.7785	20.12	< 0.0001	significant	
A-Layer Height	2.72	1	2.72	70.36	< 0.0001	significant	66.67%
B-Printing	0.1276	1	0.1276	3.30	0.0814		3.13%

speed							
C-Extrusion temperature	0.1247	1	0.1247	3.22	0.0847		3.06%
D-Infill density	0.1395	1	0.1395	3.61	0.0691		3.42%
Residual	0.9672	25	0.0387				
Lack of Fit	0.9672	20	0.0484				
Pure Error	0.0000	5	0.0000				
Cor Total	4.08	29					

From **Table 15**, it can be observed that layer height is the only parameter with a P-value less than 0.0001, indicating that it has a highly significant influence on the compressive strength of the wood-PLA lattice composite scaffold. Furthermore, layer height shows the highest percentage contribution of 66.67% toward the variation in compressive strength. In contrast, printing speed, extrusion temperature, and infill density exhibit minimal influence on compressive strength since their P-values are greater than 0.05. The percentage contributions of these parameters are relatively small, with printing speed contributing 3.13%, extrusion temperature 3.06%, and infill density 3.42%. Based on the contribution percentages, the order of influence on compressive strength for the wood-PLA lattice composite can be ranked as follows: layer height > infill density > printing speed > extrusion temperature.

Table 16: ANOVA analysis for compressive modulus.

Source	Sum of Squares	df	Mean Square	F-value	p-value	Significance	Percentage of contributions
Model	12704.14	14	907.44	23.92	< 0.0001	significant	
A-Layer Height	8953.79	1	8953.79	236.00	< 0.0001	significant	67.45%
B-Printing speed	526.78	1	526.78	13.88	0.0020	significant	3.97%
C-Extrusion temperature	311.33	1	311.33	8.21	0.0118	significant	2.35%
D-Infill density	608.83	1	608.83	16.05	0.0011	significant	4.29%
Residual	569.09	15	37.94				
Lack of Fit	569.09	10	56.91				
Pure error	0.000	5	0.0000				
Cor total	13273.23	29					

Table 16 presents the ANOVA results for the compressive modulus of the wood-PLA lattice scaffolds. A trend similar to that observed for compressive strength is also evident for compressive modulus. It can be seen that layer height exhibits the most significant influence, with a P-value less than 0.0001 and the highest percentage contribution of 67.45%. Although the other parameters, namely printing speed, extrusion temperature, and infill density, also show statistically significant effects with P-values lower than 0.05, their percentage contributions are comparatively small, accounting for 3.97%, 2.35%, and 4.59%, respectively. Based on the contribution analysis, the order of influence of the printing parameters on the compressive modulus of the wood-PLA lattice composite scaffold can be ranked as follows: layer height > infill density > printing speed > extrusion temperature.

4.3.4. Contour graph analysis on wood-PLA SC lattice scaffold

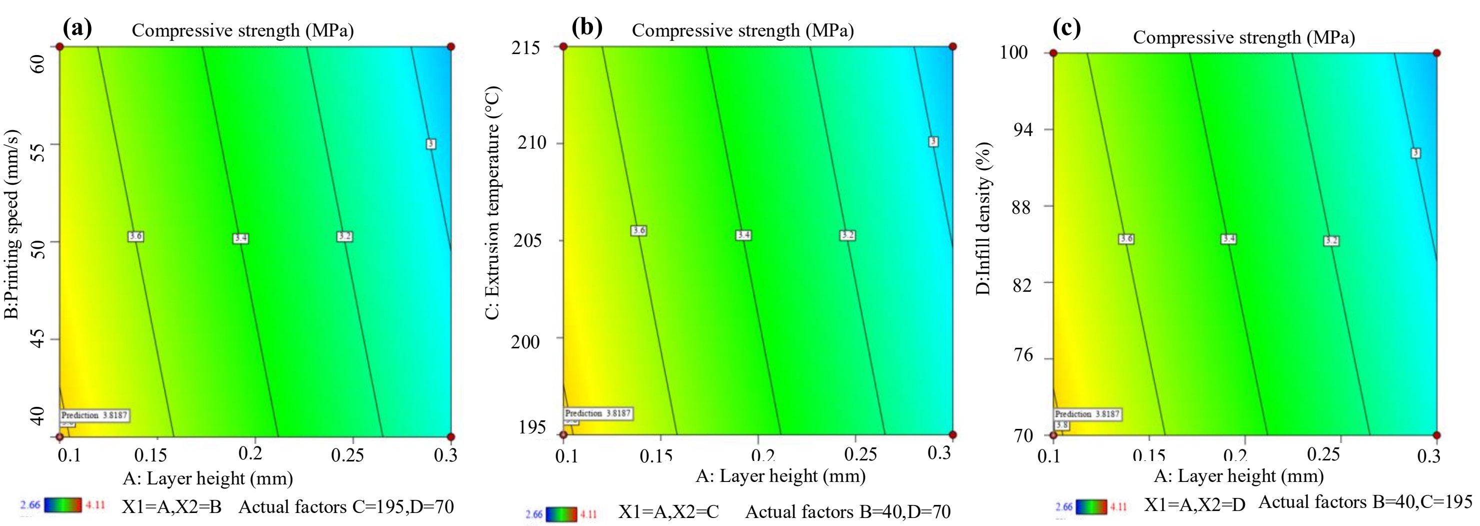

Figure 22: Contour graph analysis showing the interaction effects on compressive strength between (a) printing speed and layer height, (b) extrusion temperature and layer height, and (c) infill density and layer height.

From the ANOVA analysis , it is clearly evident that layer height is the most dominant parameters that showed significant influence on the compressive strength and compressive modulus about 66-67% of the wood-PLA composite lattice scaffolds. Therefore, in the contour graph analysis the interaction between layer height vs other parameters like printing speed, extrusion temperature and infill density are discussed for the compressive strength and compressive modulus. The color gradients in Figure 5 (a-c) representing the magnitudes of the compressive strength, where yellow indicated the higher values regions and blue indicating the lower values.

From **Figure 22** (a), the interaction between layer height and printing speed for compressive strength is illustrated. The results indicate that compressive strength decreases as the layer height increases from 0.1 mm to 0.3 mm. However, higher compressive strength is observed at lower layer heights and lower printing speeds. Increasing the printing speed slightly reduces the compressive strength because the higher speed affects the proper deposition of material in the lattice scaffolds, resulting in poor interfacial bonding between layers [122].

In **Figure 22** (b), the combined effect of layer height and extrusion temperature on compressive strength is illustrated. From the figure, it can be observed that a lower layer height with a moderate extrusion temperature results in better compressive strength. However, as the extrusion temperature increases, the compressive strength of the lattice scaffold gradually decreases. This reduction may be attributed to the over-extrusion of the material at higher temperatures, which can lead to material degradation. Moreover, Figure 22 (c) illustrates the interaction between infill density and layer height on compressive strength. Although, in most cases, higher infill density improves structural support and results in better mechanical performance[122], in this study the combination of lower infill density and lower layer height exhibited higher compressive strength. This reverse phenomenon has also been reported in previous studies on lattice-based structures during fatigue prediction analyses[127].

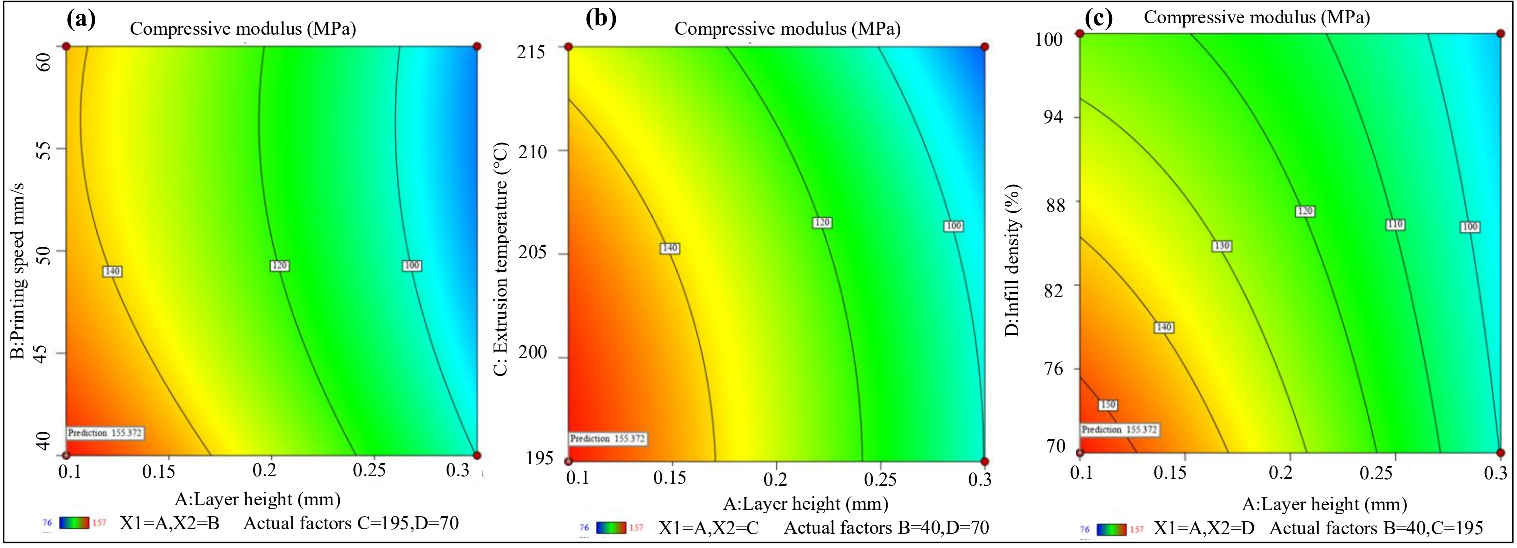

Figure 23: Contour graph analysis showing the interaction effects on compressive modulus between (a) printing speed and layer height, (b) extrusion temperature and layer height, and (c) infill density and layer height.

Figures 23 (a–c) present the contour plots of layer height with printing speed, extrusion temperature, and infill density for compressive modulus. In the contour plots, the red and yellow regions represent the highest compressive modulus values, whereas the green and blue regions indicate comparatively lower compressive modulus values. A trend similar to that observed for compressive strength is also evident for compressive modulus in the lattice wood–PLA scaffold. From Figure 23 (a), it can be observed that lower printing speed combined with lower layer height results in higher compressive modulus. Similarly, Figure 23 (b) shows that a moderate extrusion temperature combined with lower layer height produces the highest compressive modulus region, which follows a pattern similar to the compressive strength results.

Furthermore, **Figure 23** (c) illustrates that lower infill density combined with lower layer height leads to the highest compressive modulus region. These observations indicate that compressive strength and compressive modulus are correlated, as both exhibit nearly identical trends under varying process parameters.

4.3.5. 3D surface analysis on wood-PLA SC lattice scaffold

To further understand the correlation between the manufacturing parameters and the compressive properties, 3D surface analysis was generated for the wood–PLA lattice scaffolds. Figures 6 and 7 present the interaction plots for compressive strength and compressive modulus, respectively. Similar to the contour plot analysis, the 3D surface plots were generated by considering layer height as a key variable, since this parameter influenced compressive strength and modulus by approximately 66–67%, as revealed in the ANOVA analysis.

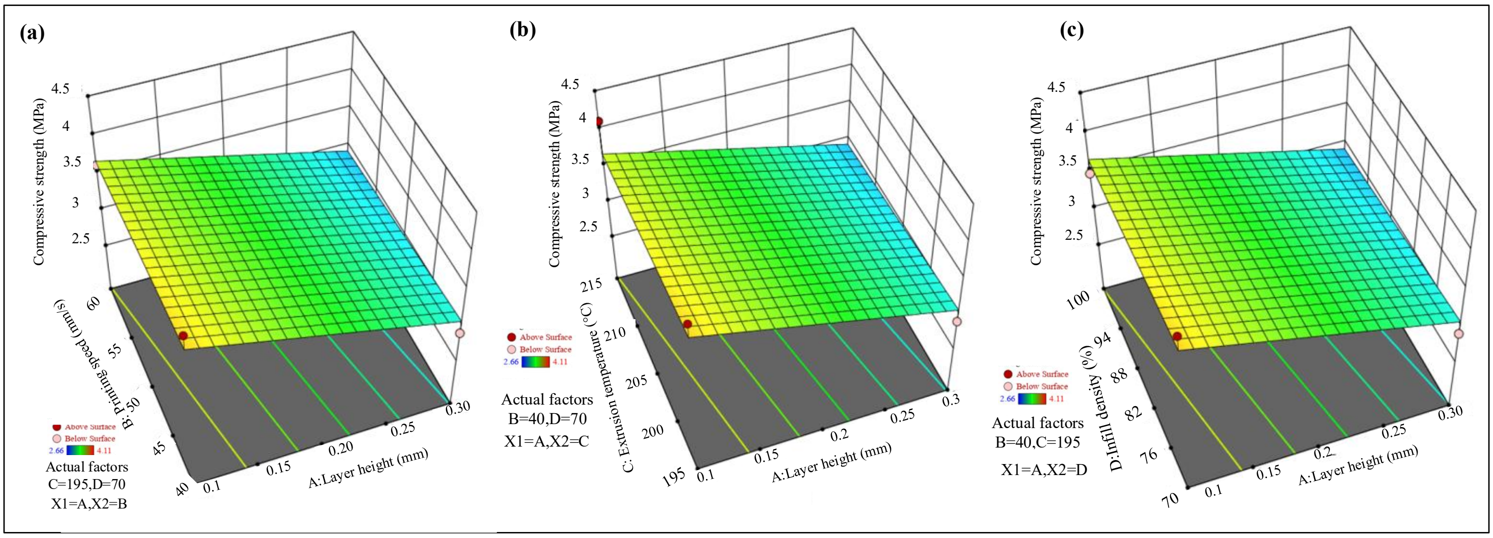

Figure 24: 3D Surface analysis showing the interaction effects on compressive strength between (a) printing speed and layer height, (b) extrusion temperature and layer height, and (c) infill density and layer height.

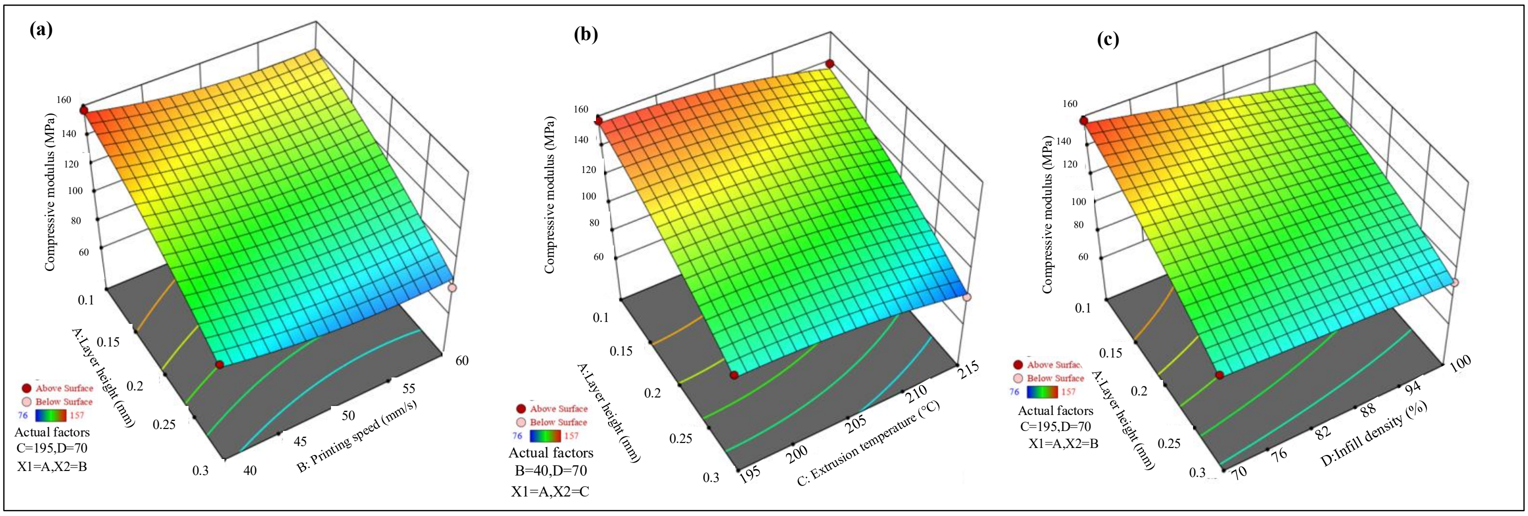

Figure 25: 3D Surface analysis showing the interaction effects on compressive strength between (a) printing speed and layer height, (b) extrusion temperature and layer height, and (c) infill density and layer height.

In **Figure 24**(a) and **Figure 25**(a), the interaction between layer height and printing speed shows that as the layer height increases, both compressive strength and compressive modulus significantly decrease. The highest compressive strength and modulus were obtained at a layer height of 0.1 mm and a printing speed of 40 mm/s. An increase in printing speed slightly reduces both responses, which may be attributed to reduced bonding time between deposited layers and poor interlayer adhesion within the lattice scaffold.

In **Figure 24**(b) and **Figure 25** (b), the interaction between layer height and extrusion temperature is illustrated with respect to compressive strength and compressive modulus. The results indicate that lower layer height combined with a moderate nozzle temperature provides improved compressive strength and modulus. However, when the extrusion temperature increases beyond the moderate range, a slight deterioration in mechanical performance is observed. This behavior may be associated with over-extrusion, excessive thermal softening, and insufficient material consolidation within the lattice structure[30,65,122].

Similarly, **Figure 24** (c) and **Figure 25** (c) illustrate the interaction between layer height and infill density. The 3D surface plots show that lower layer height combined with lower infill density results in higher compressive strength and compressive modulus, whereas increasing both parameters leads to a gradual reduction in the responses. This phenomenon may occur because excessive infill density in lattice structures can distort the designed geometry and introduce stress concentration, which ultimately leads to premature structural collapse of the lattice scaffold.

Overall, the results confirm that layer height is the most influential parameter affecting both compressive strength and compressive modulus. Furthermore, both responses exhibit very similar trends and interaction patterns, indicating a strong correlation between compressive strength and compressive modulus in the wood–PLA composite lattice scaffolds.

4.3.6. Prediction and optimization

To further determine the optimal combination of parameters for improving compressive strength and compressive modulus, an optimization process was performed for the wood–PLA lattice composite scaffold. The optimization criteria were defined based on the results obtained from the ANOVA, contour plots, and 3D surface analyses. Accordingly, the optimization objectives were set as minimizing layer height and printing speed, maintaining the extrusion temperature within a specified range, and minimizing infill density. In contrast, both compressive strength and compressive modulus were set to be maximized. Using these conditions, the software predicted the optimal parameter combination and the corresponding response values. The predicted results were subsequently validated through experimental testing. **Table 17** presents the optimized parameters, predicted outcomes, and experimentally obtained results. The comparison shows that the predicted and experimental values are in good agreement, with deviations ranging from 1–3%, indicating the reliability and accuracy of the developed optimization model.

Table 17: Point prediction and validation of the parameters and outcomes.

Prediction and model validation							
Layer height (mm)	Printing speed (mm/s)	Extrusion temperature (°C)	Infill density (%)	Compressive strength (MPa) predicted	Compressive strength (MPa) experimental	Compressive modulus (MPa) predicted	Compressive modulus (MPa) experimental
0.1	40	205	70	3.75	3.65	149.77	152
				Deviation (%)		Deviation (%)	
				2.67%		1.49%	

However, when compared with the experimental results obtained from the DOE runs, DOE-27 exhibited slightly higher mechanical performance than the optimized prediction. Specifically, DOE-27 produced a compressive strength of 4.11 MPa and a compressive modulus of 139 MPa, whereas the optimized condition predicted slightly lower values. The primary difference between the DOE-27 and the optimized parameters was observed in the extrusion temperature, which was 195 °C in DOE-27 and 205 °C in the optimized prediction. Therefore, in terms of achieving the highest compressive strength and compressive modulus, DOE-27 outperformed the optimized results predicted by the model. This difference suggests that the experimental DOE run captured a slightly better parameter combination within the studied range than the statistically predicted optimum.

4.3.7. Hyperparameter Optimization and Model Generalization

To accurately capture the highly non-linear stress-strain behavior of the 3D-printed structures, an eXtreme Gradient Boosting (XGBoost) regression model was employed. Initially, a base XGBoost model was trained using a standard parameter configuration(n_estimators=200, learning_rate=0.1, max_depth=6). Evaluating the base model revealed a degree of overfitting: while it achieved a near-perfect training R^2 of 0.9999, the testing R^2 was 0.9368 with a Root Mean Square Error (RMSE) of 0.2937 MPa. Although the test score indicated strong generalization to unseen specimens, the extreme gap between the training and testing metrics suggested the base model was memorizing noise within the training data.

To mitigate this memorization and explore potential improvements in predictive accuracy, a randomized hyperparameter tuning approach was executed using 5-fold cross-validation. The optimized hyperparameters for the XGBoost algorithm are summarized in **Table 18**. By constraining the maximum tree depth and introducing randomization through subsampling, the model was mathematically prevented from over-relying on specific training artifacts.

Table 18: Optimized Hyperparameters for XGBoost.

ML Model	Hyperparameters	Best Values
XG Boost	Learning Rate	0.1228
	Max Depth	4
	Subsample	0.8586
	Colsample Bytree	0.8061
	N Estimators	58

As presented in **Table 19**, the hyperparameter tuning process successfully reduced the model's overfitting. The training R^2 was lowered to 0.9972 and the training RMSE increased to 0.0586 MPa, indicating the model was no longer memorizing the data perfectly. On the unseen testing set, the tuned model achieved an R^2 of 0.9290, an RMSE of 0.3113 MPa, and a Mean Absolute Error (MAE) of 0.1847 MPa. While the tuning successfully narrowed the gap between the training and testing metrics proving the regularization worked the overall predictive accuracy remained highly comparable to the base model. This confirms that XGBoost configurations are highly robust, successfully capturing approximately 93% of the variance in the unseen experimental stress-strain curves across the relevant testing regimes.

Table 19: Performance Evaluation of Base vs. Tuned XGBoost Models.

MODEL	**Train R^2**	**Test R^2**	**Train RMSE**	**Test RMSE**	**Train MAE**	**Test MAE**
Base Model	0.9999	0.9368	0.012	0.2937	0.0082	0.1788
Hyperparameter Tuning	0.9972	0.929	0.0586	0.3113	0.0435	0.1847

4.3.8. Validation of Key Mechanical Properties

To see how well the machine learning framework actually works in practice, we tested its predictions against the real-world experimental results of three completely unseen specimens (Specimens 1, 9, and 17).

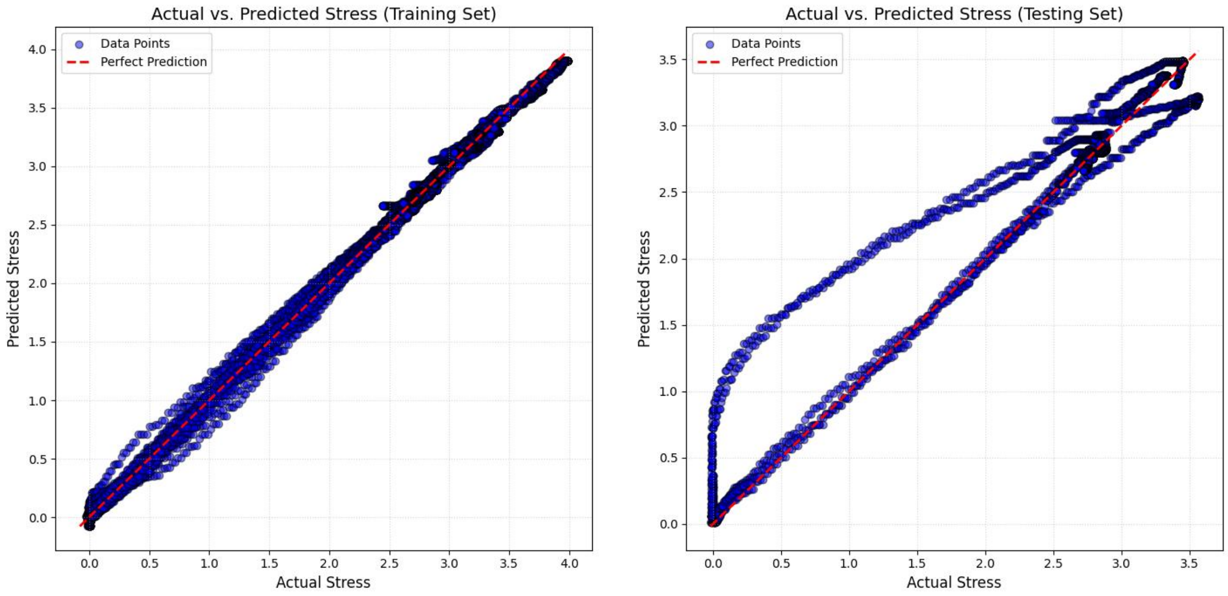

(a) (b)

Figure 26: Actual vs Predicted curve for XGBoost tuned model for (a) train data and, (b) test data.

As shown by the tight clustering in the parity plots in **Figure 26.** and the exact values in **Table 20**, the XGBoost model proved highly capable of predicting macro-mechanical properties using nothing but the initial 3D printing parameters. When predicting compressive strength, the model's estimates were remarkably close to the physical tests, keeping the error margin strictly between 2.14% and 6.74%. It was just as precise when predicting the compressive modulus, with error rates staying extremely low, between 1.82% and 8.14%.

These low error rates are a strong indicator that the model hasn't just memorized the training data it has genuinely learned the physical relationship between the printing parameters and the mechanical behavior of the material. Ultimately, this proves our framework can serve as a highly reliable, non-destructive tool. It can confidently predict how well an additively manufactured lattice will perform and absorb energy, which could drastically cut down the time, material waste, and cost of physical testing.

Table 20: Comparison of Experimental vs. ML-Predicted Mechanical Properties.

Specimen No.	Compressive Strength (Exp)	Compressive Strength (ML)	Error(%)	Compressive Modulus (Exp)	Compressive Modulus (ML)	Error(%)
1	3.56	3.32	6.74	110	112	1.82
9	3.35	3.26	2.69	125	116	7.2
17	2.80	2.86	2.14	91.44	84	8.14

4.3.9. Microscopic analysis on Wood-PLA composite lattice scaffold

A comparative study was conducted among different design of experiments (DOE) considerations. To further correlate the manufacturing parameters with the compressive strength and compressive modulus, microscopic analysis was performed. **Figure 27 (a–c)** represents DOE-1, whereas **Figure 27 (d–f)** corresponds to DOE-20. The primary difference between these two DOE conditions is the printing temperature.

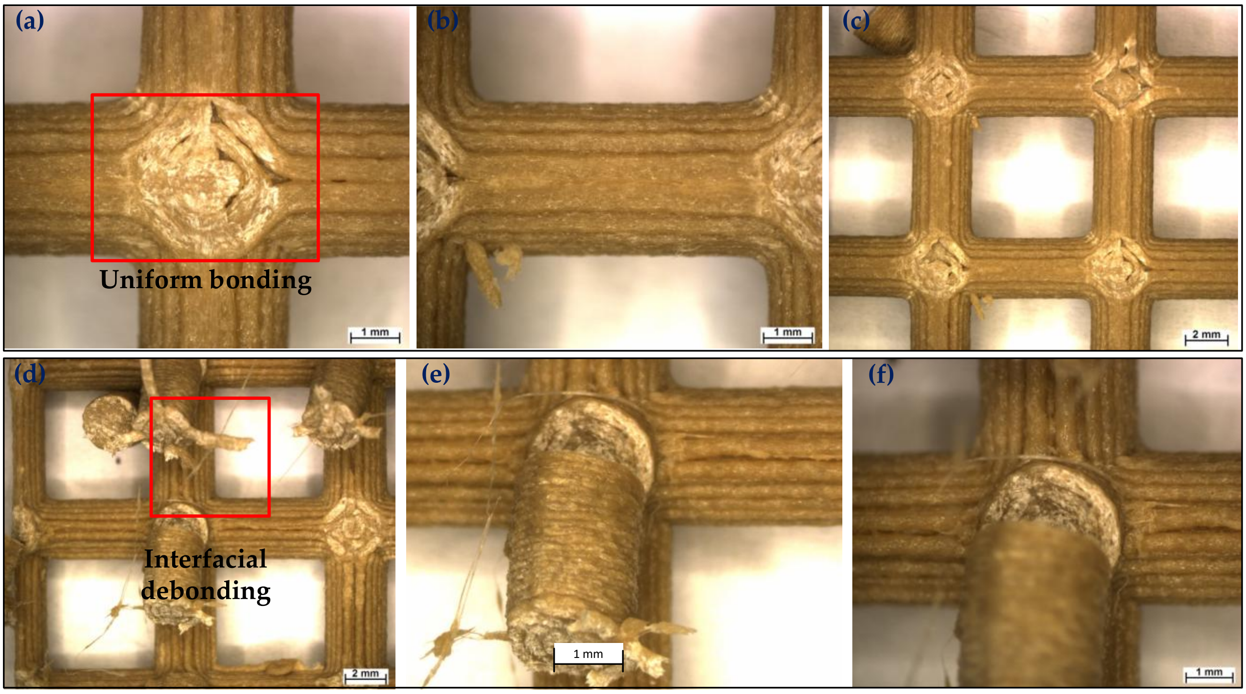

Figure 27: (a-c) Microscopic analysis of DOE-1 and (d-f) DOE-20 at magnifications of 6.5× and 16×.

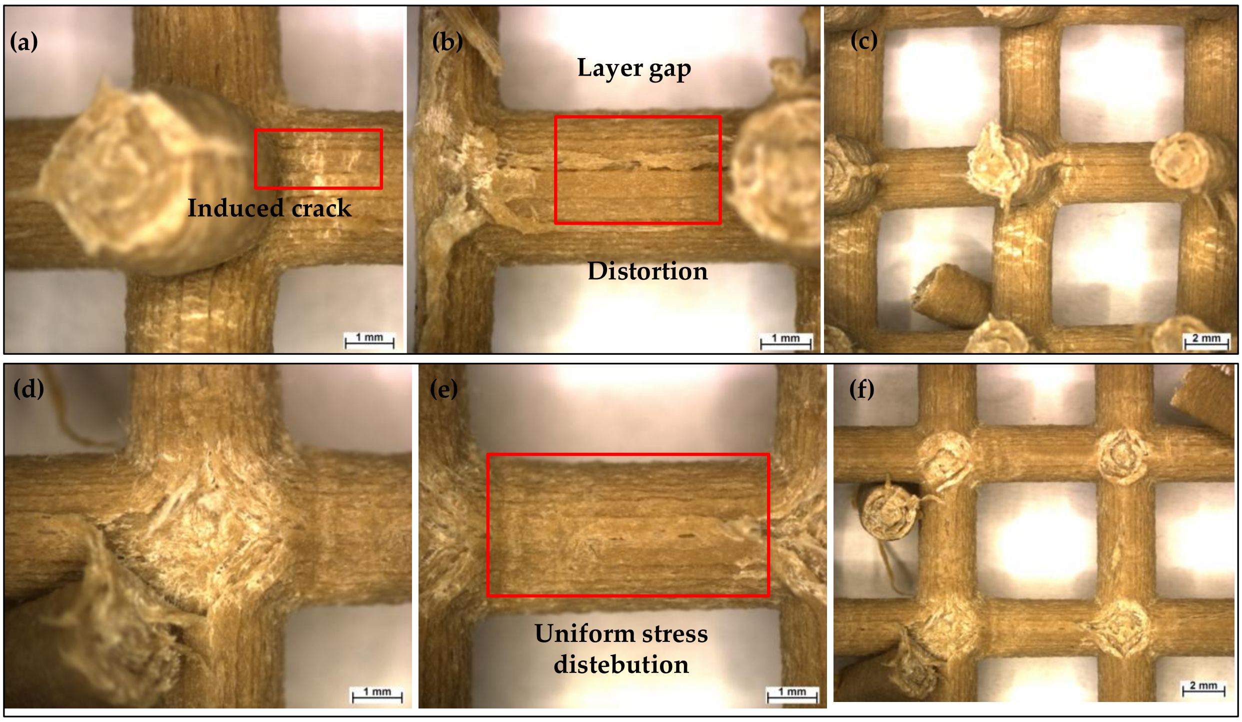

Figure 28: (a-c) Microscopic comparison of DOE-3 and (d-f) DOE-9 at magnifications of 6.5× and 16×.

As observed in Figure **27 (a–c),** the lower printing temperature of 185°C resulted in improved interfacial bonding at the strut junctions, promoting more effective load transfer within the lattice structure compared to DOE-20. In contrast, the higher printing temperature of 225°C, shown in **Figure 27 (d–f),** exhibited noticeable fiber pull-out, indicating weaker adhesion between the wood fibers and the PLA matrix. This behavior is likely associated with thermal degradation or matrix softening at elevated temperatures. Therefore, excessively high printing temperatures are not suitable for natural fiber–reinforced wood–PLA composite lattice structures. To enhance mechanical performance, low to moderate printing temperatures are more appropriate, as they help preserve interfacial bonding and maintain desirable compressive strength and modulus.

In **Figure 28 (a–c),** a comparison was also conducted between two printing speeds, 40 mm/s and 60 mm/s. As observed in **Figure 28 (a–c),** the specimen printed at the higher speed of 60 mm/s (DOE-3) exhibited lower compressive strength and compressive modulus. This reduction can be attributed to irregular material deposition and the presence of interlayer gaps, which weaken the structural integrity of the lattice. In contrast, the sample fabricated at the lower printing speed of 40 mm/s (DOE-9) showed more uniform filament deposition and improved interlayer bonding. Consequently, the lower printing speed resulted in enhanced compressive strength and overall mechanical performance.

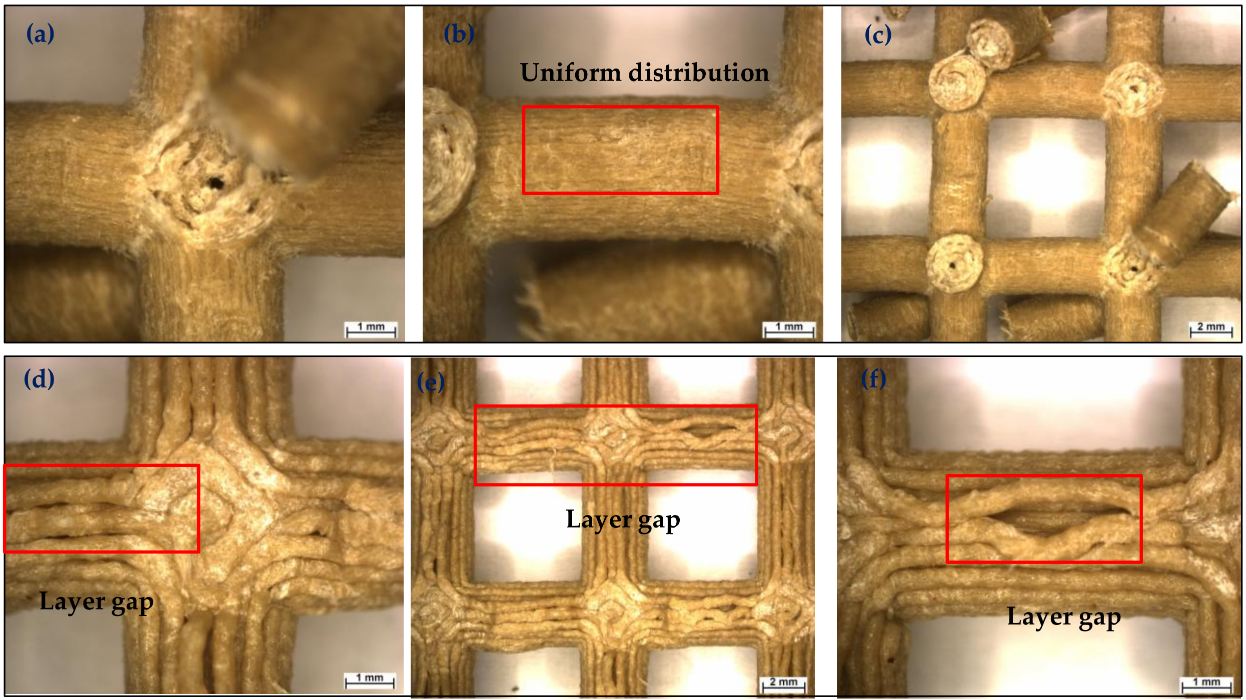

Figure 29: (a-c) Microscopic comparison of DOE-8 and (d-f) DOE-30 at magnifications of 6.5× and 16×.

To evaluate the effect of layer height, a comparison was conducted between DOE-8 and DOE-30. In DOE-8, the layer height was 0.06 mm, whereas in DOE-30 it was 0.32 mm. All other printing parameters, including nozzle temperature, printing speed, and infill density, were kept constant to isolate the influence of layer height. As shown in **Figure 29 (a–c)**, the specimen fabricated with a 0.06 mm layer height exhibits more uniform material distribution and minimal interlayer gaps, resulting in improved interfacial bonding and more efficient load transfer throughout the lattice structure. This enhanced structural integrity leads to higher compressive strength and compressive modulus. In contrast, the sample printed with a 0.32 mm layer height **Figure 29 (d–f)** demonstrates noticeable interlayer gaps and irregular filament deposition, which create structural discontinuities and stress concentration sites. These microstructural defects weaken the overall lattice architecture, resulting in reduced compressive strength and compressive modulus compared to the specimen printed with the lower layer height.

To understand the role of infill density, a comparison was conducted between DOE-2 and DOE-3. The primary difference between these two experimental conditions is the infill density, which was 70% for DOE-2 and 100% for DOE-3, while all other printing parameters remained constant. As shown in **Figure 30** (a–c), the specimen fabricated with a lower infill density of 70% exhibits a smoother surface morphology and more uniform material distribution within the lattice structure. This improved deposition promotes effective load transfer, resulting in higher compressive strength and compressive modulus.

In contrast, the sample printed with 100% infill density (**Figure 30** (d–f)) demonstrates excessive material accumulation, overlapping filament layers, and irregular deposition at the junction regions. Such congestion introduces stress concentration sites and reduces structural uniformity, leading to lower compressive strength and compressive modulus. These findings suggest that a moderate infill density (70%) provides a more optimized microstructure and comparatively better mechanical performance for wood–PLA lattice structures.

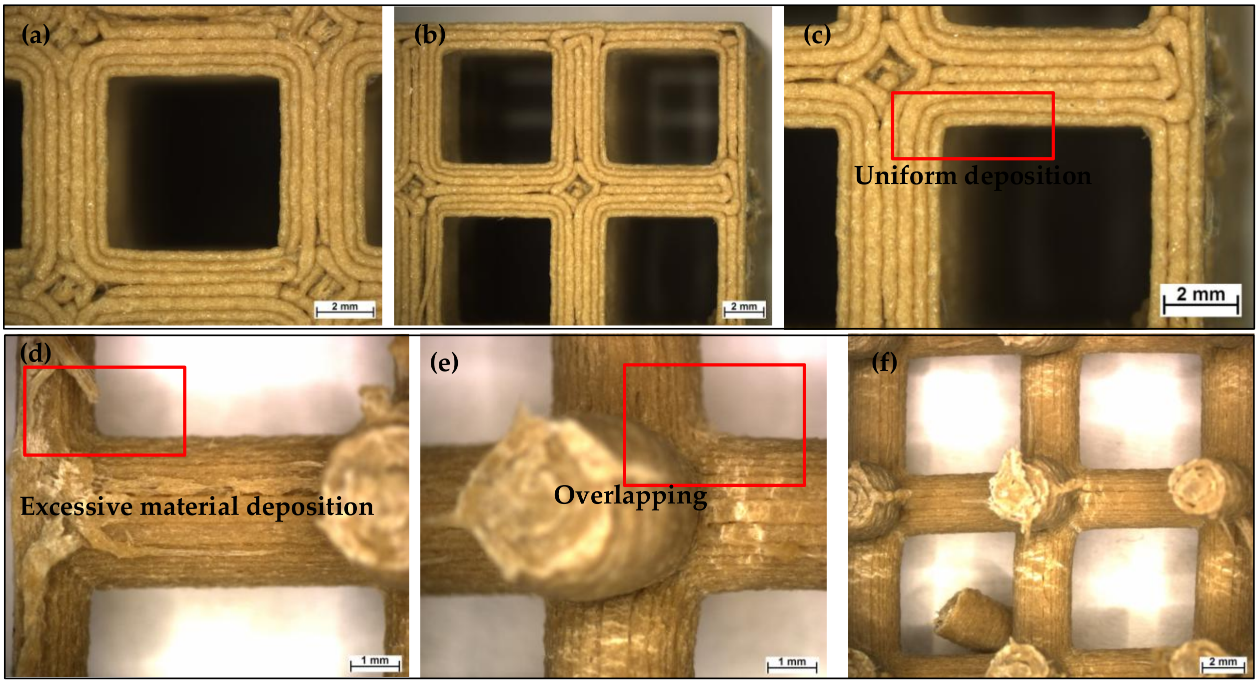

Figure 30: (a-c) Microscopic comparison of DOE-2 and (d-f) DOE-3 at magnifications of 6.5× and 16×.

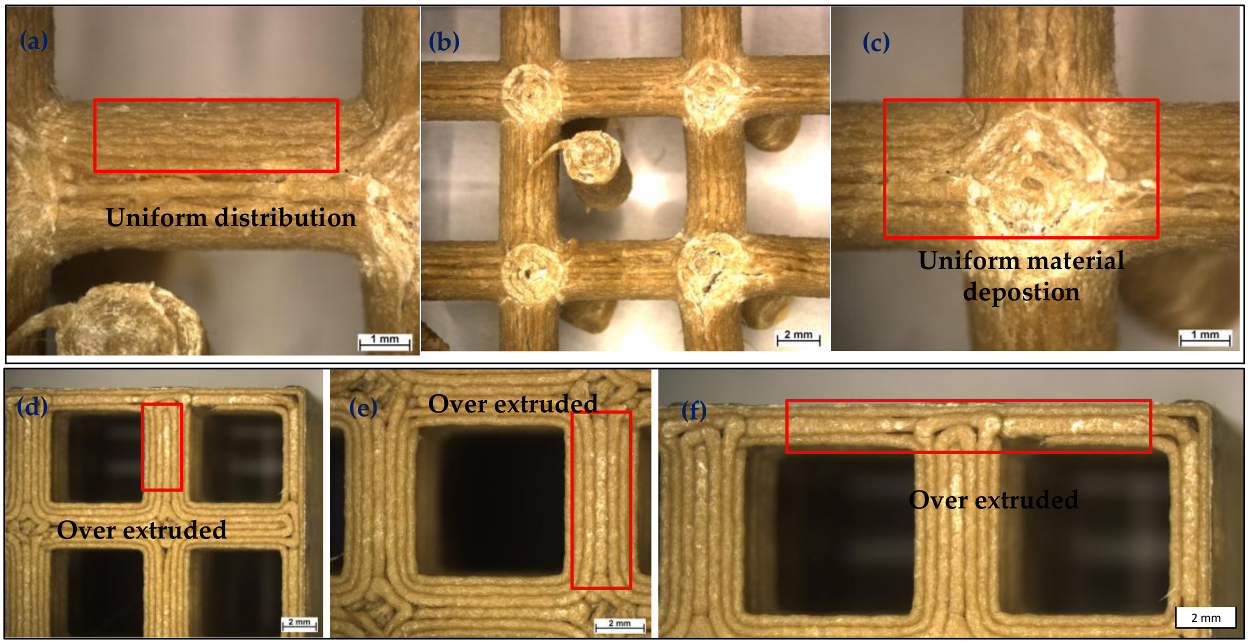

Figure 31: (a-c) Microscopic comparison of DOE-27 and (d-f) DOE-28 at magnifications of 6.5× and 16×.

Finally, a comparison was conducted between DOE-27 and DOE-28, representing the highest and lowest compressive strength values, respectively. As shown in **Figure 31** (a–c), DOE-27, fabricated with a lower layer height (0.1 mm), higher nozzle temperature (215°C), lower printing speed (40 mm/s), and moderate infill density (70%), exhibits uniform material distribution and well-defined node formation within the lattice structure. The improved interlayer bonding and controlled filament deposition promote efficient load transfer, resulting in the highest compressive strength (4.11 MPa) and compressive modulus (139 MPa).

In contrast, DOE-28, produced with a higher layer height (0.3 mm), higher printing speed (60 mm/s), lower printing temperature (195°C), and 100% infill density, shows signs of over-extrusion, irregular filament stacking, and less consolidated junction regions in **Figure 31** (d-f). The combination of thicker layers, insufficient thermal bonding, and excessive material accumulation leads to structural discontinuities and stress concentration sites within the lattice. Consequently, DOE-28 demonstrates significantly lower compressive strength (2.66 MPa) and compressive modulus (76 MPa).

4.3.10. SEM analysis on wood-PLA SC lattice scaffold

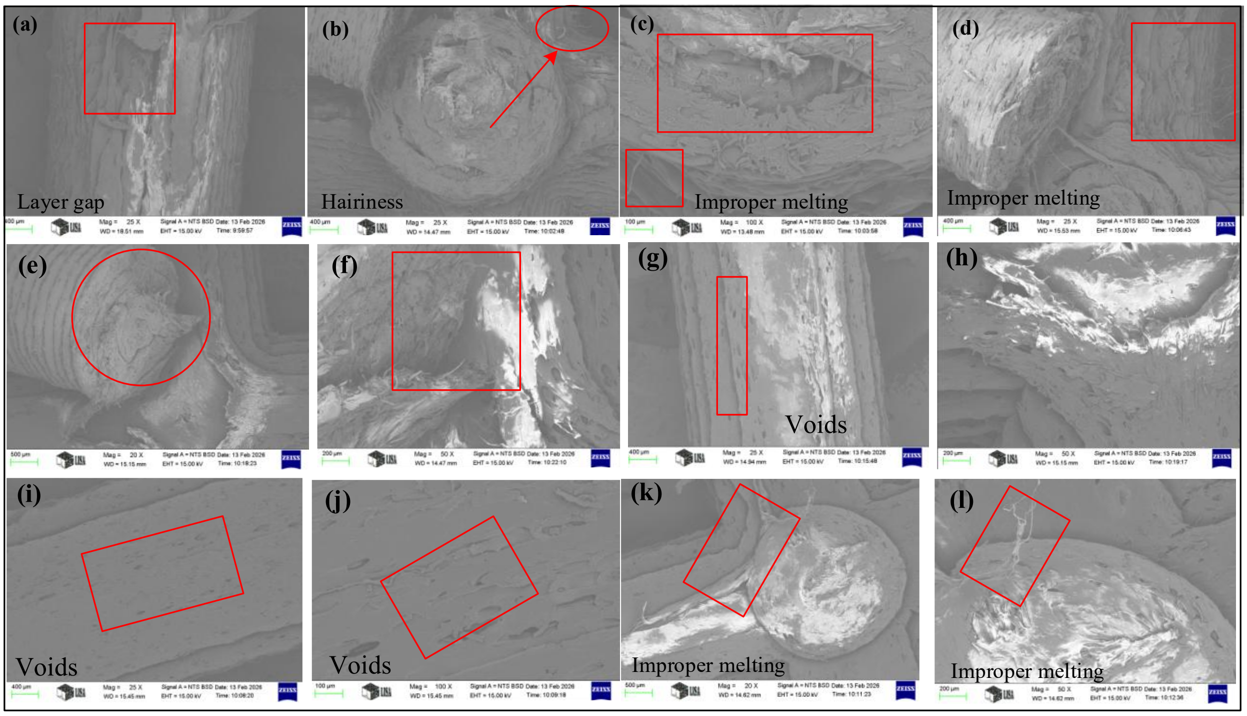

Figure 32: SEM analysis of (a–d) DOE-8, (e–h) DOE-20, and (i–l) DOE-30 at different magnifications ranging from 100 µm to 500 µm.

To further understand the influence of manufacturing parameters on the compressive properties of the wood–PLA lattice scaffold, scanning electron microscopy (SEM) analysis was performed. For this analysis, three different layer heights (0.06 mm, 0.20 mm, and 0.32 mm) were selected, corresponding to DOE-8, DOE-20, and DOE-30, respectively. These samples were chosen because the previous ANOVA, contour, and 3D surface analyses revealed that layer height had a significant influence on both compressive strength and compressive modulus.

Therefore, SEM observations were conducted to examine the microstructural differences and printing defects associated with varying layer heights. In addition, a comparative analysis was carried out between DOE-27, which exhibited the highest compressive strength, and DOE-15, which showed the highest compressive modulus, along with the sample exhibiting the lowest compressive strength and modulus (DOE-28). This comparison was performed to investigate how the processing parameters influence the formation of printing-induced defects, interlayer bonding, and structural integrity within the lattice composite scaffold.

In **Figure 32**, the SEM micrographs corresponding to DOE-8, DOE-20, and DOE-30 are illustrated to analyze the microstructural characteristics of the wood–PLA lattice scaffold. Figures 9 (a–d) represent the microstructure of DOE-8, fabricated with a low layer height of 0.06 mm. Although the layer height is relatively small, interlayer gaps between successive layers and filament hairiness are clearly observed. These defects indicate insufficient fusion and improper bonding between the deposited filaments, which may result from unstable extrusion or inadequate thermal bonding during the printing process. Such imperfections weaken the structural integrity of the scaffold and consequently reduce the compressive strength and compressive modulus, despite the smaller layer height compared to DOE-15 and DOE-27.

For DOE-20, produced with a layer height of 0.20 mm, the microstructure appears comparatively more consolidated than that of DOE-8. However, localized void regions and imperfect bonding between successive layers are observed within the strut sections, as shown in **Figures 32**(e–h). These defects can act as stress concentration points during compressive loading, which may negatively influence the mechanical performance of the scaffold. As a result, although the structure shows improved consolidation, the presence of voids and imperfect bonding can still lead to reduced compressive performance compared with DOE-8.

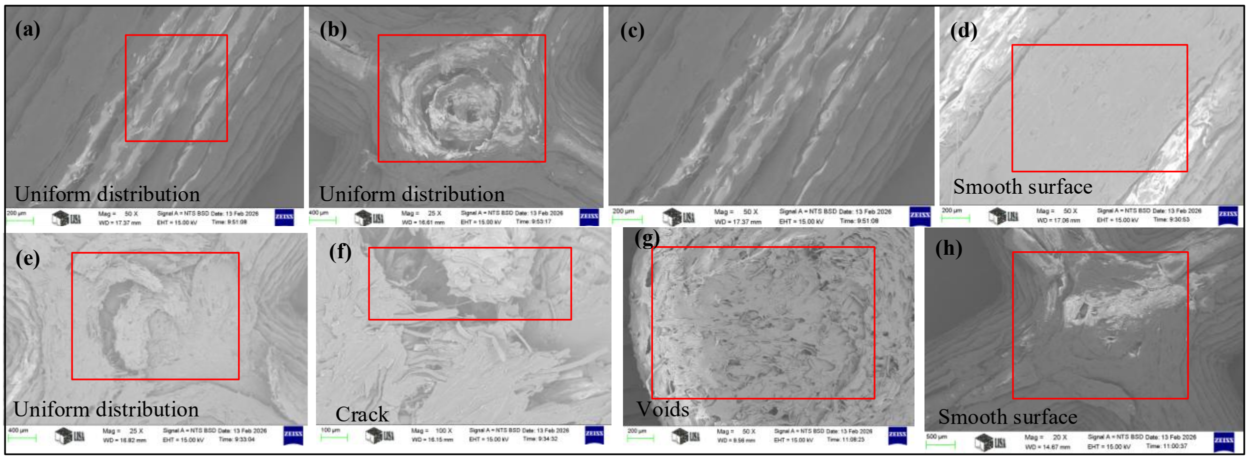

Figure 33: SEM analysis of (a–c) DOE-15, (d–f) DOE-27, (g) DOE-28, and (h) the optimized lattice scaffold at different magnifications ranging from 100 μm to 500 μm.

In contrast, DOE-30, fabricated with the highest layer height of 0.32 mm, exhibits more pronounced void formation and regions of improper melting, as shown in **Figures 32** (i–l). The larger layer height reduces the degree of filament fusion between deposited layers, resulting in significant micro-voids and irregular filament morphology. These microstructural defects reduce the interlayer bonding strength and structural stability of the lattice scaffold, ultimately leading to deterioration in compressive strength and compressive modulus compared with DOE-8 and DOE-20.

Furthermore, this research investigated the set of processing parameters corresponding to the highest compressive modulus (DOE-15), highest compressive strength (DOE-27), and lowest compressive strength and modulus (DOE-28), along with the optimized parameters obtained through the RSM method, in order to understand the influence of the considered variables. In **Figure 33** (a–c), the SEM images of DOE-15 are presented. The micrographs indicate that the lattice scaffold fabricated with a lower layer height (0.1 mm), low printing speed (40 mm/s), lower printing temperature (195 °C), and 70% infill density exhibits a relatively uniform material distribution with fewer manufacturing defects. This improved structural uniformity contributes to a higher compressive modulus.

Similarly, **Figure 33** (d–f) illustrates the microstructure of DOE-27, where relatively good manufacturing accuracy and fewer defects are also observed, leading to improved compressive strength comparable to DOE-15. The main difference between DOE-15 and DOE-27 is the higher nozzle temperature (215 °C) used in DOE-27, which may enhance interlayer bonding and thus improve compressive strength. In contrast, DOE-28, shown in **Figure 33** (g), exhibits significant void formation within the lattice scaffold. These voids indicate poor material consolidation, which results in the lowest compressive strength and modulus. This behavior can be attributed to the processing conditions used in DOE-28, including a higher layer height (0.3 mm), higher printing speed (60 mm/s), moderate printing temperature, and 100% infill density, which negatively affect material bonding and structural integrity.

Moreover, the optimized sample shown in **Figure 33** (h) demonstrates a smooth and relatively defect-free surface morphology. The optimized compressive modulus and compressive strength were achieved with similar printing parameters, with the only notable difference being the moderate nozzle temperature of 205 °C, which contributes to improved manufacturing quality and mechanical performance.

4.4. Comparison in response for biological evaluations

To further understand the biological performance, the physical properties of the wood–PLA composite lattice scaffold were investigated in this study prior to in vitro evaluation. The physical and physiochemical properties considered include contact angle, water absorption, and thickness swelling ratio. In addition, the influence of manufacturing parameters on these properties was also examined. To systematically investigate this effect, selected design of experiments (DOE) conditions were adopted, in which three parameters were constant while one parameter was varied to evaluate its individual influence.

4.4.1.Contact angle

The surface wettability of the wood–PLA lattice scaffold is measured through the contact angle. Table 6 illustrates the contact angles obtained under different DOE conditions and parameters. As mentioned earlier, hydrophilic lattice scaffolds are more suitable for bone tissue engineering and biological applications, where the contact angle is less than 90°. The contact angle values presented in Table 6 are the average of three samples.

From **Table 21**, it can be observed that increasing the nozzle temperature from 185°C (DOE-1) to 225°C (DOE-20) slightly enhances the contact angle from 99° to 103°, maintaining hydrophobicity in the wood–PLA lattice composite scaffold. However, when comparing DOE-15 and DOE-27, where the nozzle temperatures are 195°C and 215°C, respectively, it is observed that the increase in nozzle temperature reduces the contact angle from 97° to 75°. Similarly, when comparing the optimized combination at a nozzle temperature of 205°C with DOE-27 at 215°C, the lower temperature (205°C) in the optimized parameters results in a higher contact angle of 87°, whereas DOE-27 shows a lower contact angle of 75°. This indicates that nozzle temperature has a significant influence on the contact angle. A moderate range of nozzle temperature, combined with a lower layer height of 0.1 mm, lower printing speed of 40 mm/s, and infill density of 70%, results in improved surface energy and wettability. This leads to hydrophilic behavior with a lower contact angle, which is more desirable for biological or tissue engineering applications, as it enhances protein adsorption, cell attachment, and cell migration [128].

Table 21: Contact angle comparison across different DOE and parameters.

Comparison parameter	Experiments	Layer height (mm)	Printing speed (mm/s)	Nozzle temperature (°C)	Infill Density (%)	Contact angle	Surface wettability
Nozzle temperature (°C)	DOE-1	0.2	50	**185**	85	99°>90°	Hydrophobic
	DOE-20	0.2	50	**225**	85	103°>90°	Hydrophobic
Highest modulus	DOE-15	0.1	40	**195**	70	97°>90°	Hydrophobic
Highest strength	DOE-27	0.1	40	**215**	70	75°<90°	Hydrophilic
Optimize	Optimize	0.1	40	205	70	87°<90°	Hydrophilic
Infill density (%)	DOE-27	0.1	40	215	**70**	75°<90°	Hydrophilic
	DOE-9	0.1	40	215	**100**	87°<90°	Hydrophilic
Printing speed (mm/s)	DOE-3	0.1	**60**	215	100	83°<90°	Hydrophilic
	DOE-9	0.1	**40**	215	100	87°<90°	Hydrophilic
Layer height (mm)	DOE-8	**0.06**	50	205	85	107°>90°	Hydrophobic
	DOE-30	**0.32**	50	205	85	92°>90°	Hydrophobic

However, the effect of printing speed was also evaluated by comparing DOE-3 (60 mm/s) and DOE-9 (40 mm/s). From this comparison, it is observed that printing speed has only a slight influence on the contact angle. The lower printing speed of 40 mm/s, due to better fusion and bonding between successive layers, shows a slightly higher contact angle of 87° compared to 83°

at 60 mm/s. Nevertheless, both conditions exhibit hydrophilic characteristics. On the other hand, the effect of layer height was also analyzed. By comparing DOE-8 (0.06 mm layer height) and DOE-30 (0.32 mm layer height), it is found that DOE-30 produces a lower contact angle of 92°. This indicates that a finer layer height increases surface roughness, promoting hydrophobic behavior compared to thicker layers, which may not be suitable for biomedical applications. However, both cases still fall within hydrophobic characteristics. Moreover, in terms of infill density, the comparison was conducted between DOE-27 (70%) and DOE-9 (100%). The lower infill density of 70% provides a better (lower) contact angle of 75° compared to 87° at 100% infill. This may be due to higher infill density causing voids or irregular deposition, which can affect surface energy and increase the contact angle. However, both conditions exhibit hydrophilic characteristics.

Overall, it is observed that manufacturing parameters have a significant influence on the contact angle of FDM-printed wood–PLA composite scaffolds. However, wettability behavior depends more on the combination of parameters rather than individual parameter variations. The best combination, with a contact angle of 75°, is achieved in DOE-27, which is particularly suitable for bone tissue engineering and biological applications [129].

4.4.2.Water absorption and thickness swelling ratio

For bone tissue engineering applications, lower water absorption (%) and thickness swelling ratio are generally more preferable[129]. The main reason is that excessive water absorption and swelling may degrade the mechanical properties, particularly strength, which is one of the predominant requirements in bone tissue engineering, hard tissue replacement, and post-implantation performance. Moreover, excessive degradation may also reduce the overall load-bearing capacity of the lattice scaffold.

Table 22: water absorption and thickness swelling comparison across different DOE and parameters.

Comparison parameter	**Experiments**	**Layer height (mm)**	**Printing speed (mm/s)**	**Nozzle temperature (°C)**	**Infill Density (%)**	**Water absorption (%)After 24 Hours**	**Water absorption (%)After 48 Hours**	**Thickness swelling (%) After 24 Hours**	**Thickness swelling (%)After 48 Hours**
Nozzle temperature (°C)	DOE-1	0.2	50	**185**	85	1.51%	2.88%	0.0%	1.22%
	DOE-20	0.2	50	**225**	85	1.77%	3.18%	5.59%	5.59%
Highest modulus	DOE-15	0.1	40	**195**	70	1.59%	3.17%	2.07%	4.13%

Highest strength	DOE-27	0.1	40	**215**	70	0.91%	2.59%	5.69%	5.69%
Optimize	Optimize	0.1	40	205	70	1.89%	2.68%	1.26%	3.35%
Infill density (%)	DOE-27	0.1	40	215	**70**	0.91%	2.59%	5.69%	5.69%
	DOE-9	0.1	40	215	**100**	4.12%	6.70%	4.05%	4.05%
Printing speed (mm/s)	DOE-3	0.1	**60**	215	100	1.59%	2.98%	0.91%	13.64%
	DOE-9	0.1	**40**	215	100	4.12%	6.70%	4.05%	4.05%
Layer height (mm)	DOE-8	**0.06**	50	205	85	1.67%	2.89%	0.85%	4.68%
	DOE-30	**0.32**	50	205	85	4.04%	3.73%	0.39%	1.55%

However, when comparing DOE-15 and DOE-27, DOE-27 exhibits lower water absorption, with 0.91% at 24 hours and 2.59% at 48 hours. In contrast, DOE-27 shows a relatively higher thickness swelling ratio, with 5.69% at both 24 and 48 hours, compared to DOE-15, which shows 2.07% at 24 hours and 4.13% at 48 hours. On the other hand, the optimized combination provides more controlled water absorption, with 1.89% at 24 hours and 2.68% at 48 hours, while the thickness swelling is 1.26% at 24 hours and 3.35% at 48 hours. Therefore, overall, it is found that limiting the printing temperature, together with a lower layer height of 0.1 mm, printing speed of 40 mm/s, and 70% infill density, may induce better structural support in the lattice composite scaffold under body fluid environments.In terms of infill density, the lower infill density of 70% provides lower water absorption, with 0.91% at 24 hours and 2.59% at 48 hours, compared to the higher infill density of 100%. However, the thickness swelling ratio at 100% infill density is slightly lower, at 4.05% at both 24 and 48 hours, compared to 5.69% at 70% infill density. Overall, although there are slight deviations, the lower infill density of 70% is considered slightly better for biological environments than the higher infill density of 100%.

According to **Table 22**, in terms of layer height, the thicker layer of 0.32 mm shows higher water absorption than the thinner layer of 0.06 mm. However, the thickness swelling ratio of the thicker layer is relatively better, with 0.39% at 24 hours and 1.55% at 48 hours, compared to the 0.06 mm layer height. In terms of printing speed, the lower printing speed of 40 mm/s provides higher water absorption than the printing speed of 60 mm/s. However, the 60 mm/s printing speed in DOE-3 results in a thickness swelling ratio of 13.64%, which is extremely high and may negatively affect the geometry and dimensional stability of the lattice scaffold. Therefore, to achieve balanced physicochemical performance of the wood–PLA lattice composite scaffold, the lower printing speed is more preferable.

Overall, it is observed that different manufacturing parameters may provide different outcomes in terms of water absorption and thickness swelling ratio. DOE-27 appears to be more suitable for biological applications because it provides the lowest water absorption, 0.91% at 24 hours and 2.59% at 48 hours, which is highly desirable. Although the thickness swelling ratio is comparatively higher, this parameter combination would still be suitable for biomedical applications, particularly in bone tissue engineering, due to its overall physicochemical performance, as well as its previously discussed strength and contact angle performance.

4.4.3. Biological evaluations

Considering the compressive strength (4.11 MPa), contact angle (75°), and water absorption performance, the lattice composite scaffold was re-fabricated using an FDM printing machine with the DOE-27 material combination, as it demonstrated superior performance compared to other DOE conditions and optimized parameters. Cytotoxicity evaluation was performed using the human buccal carcinoma cell line (TR146) via the Neutral Red uptake assay. Three extract concentrations (16.6 mg/mL, 50 mg/mL, and 100 mg/mL) were selected to investigate the dose-dependent cytotoxic response of the developed wood-PLA composite lattice scaffold. These concentrations represent low, medium, and high exposure conditions.

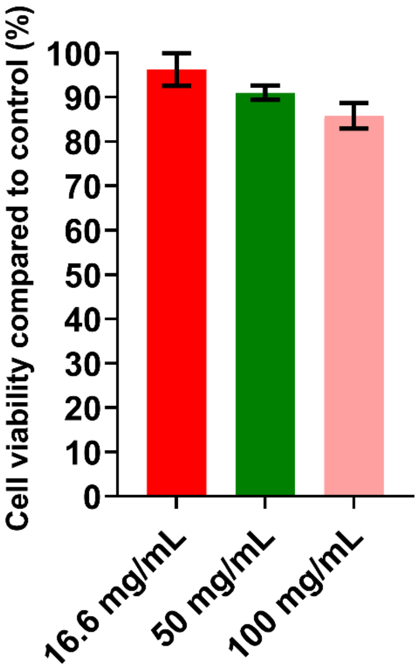

Figure 34: TR-146 cell viability comparison at different concentrations levels of wood-PLA lattice composite scaffold.

As shown in **Figure 34**, cell viability results indicate that at the lowest concentration (16.6 mg/mL), cell viability reached approximately 98%, suggesting negligible or no cytotoxic effect. At the medium concentration (50 mg/mL), cell viability decreased slightly to around 90%. A further reduction was observed at the highest concentration (100 mg/mL), where cell viability was approximately 85%. Although a gradual decrease in cell viability was observed with increasing concentration, all values remained above the 70% threshold, which is widely accepted as the criterion for non-cytotoxic materials [130]. Overall, the findings demonstrate that the wood-PLA lattice scaffold exhibits low cytotoxicity and good biocompatibility toward TR146 cells, even after 7 days of exposure.

4.4.5. Applications of the wood-PLA composite lattice scaffold

Bone tissue is the second most transplanted tissue after blood, with over 2.2 million procedures performed annually to address various complications, including fractures, tumors, cancer, infections, congenital defects, and osteogenesis-related conditions [131]. According to previous reports, approximately USD 4.3 billion was spent on bone graft materials in 2015, and this value is projected to reach USD 6.6 billion by 2026. In addition, the demand for maxillofacial and oral tissue engineering, including dental replacements, has significantly increased in recent years, leading to a growing need for cost-effective biomaterials and bioimplantation solutions [132]. However, the high cost of materials and fabrication techniques remains a major limitation in many clinical applications.

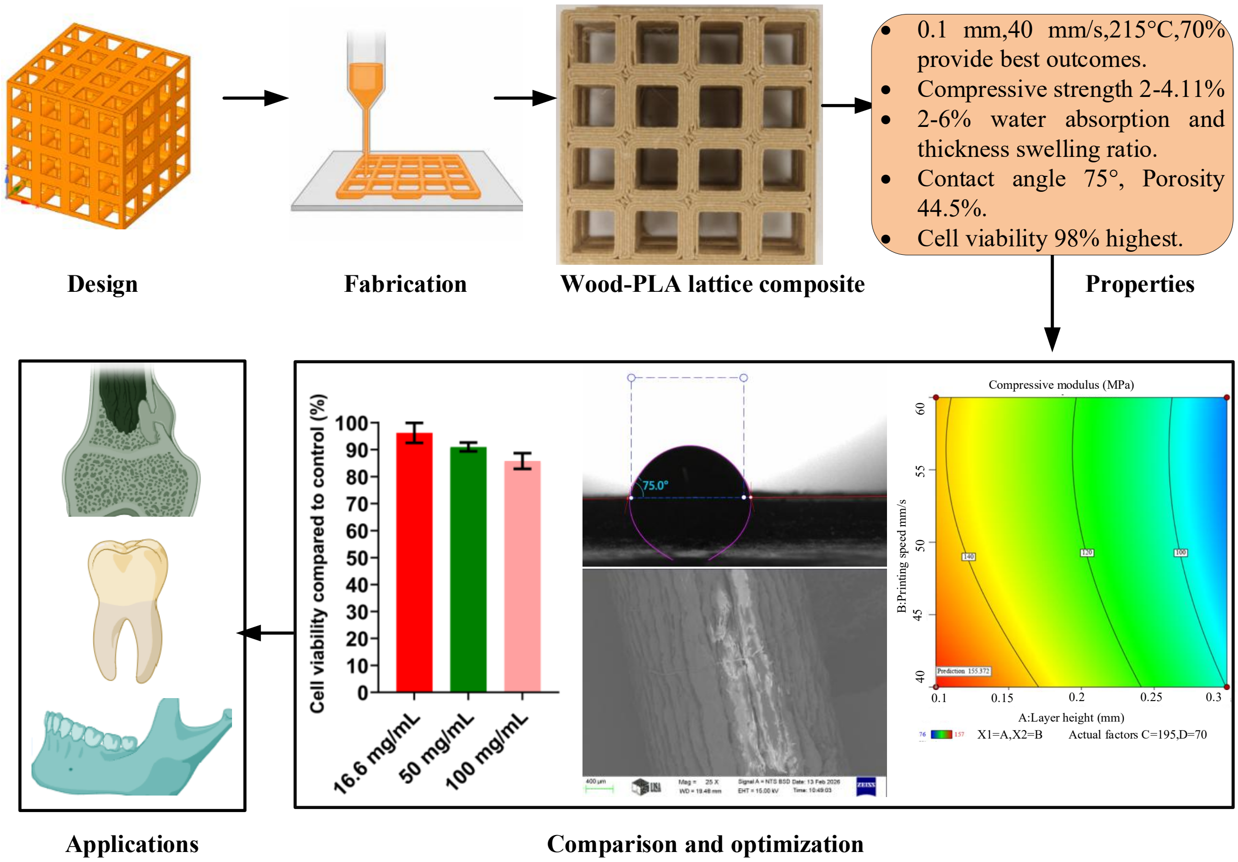

- 0.1 mm,40 mm/s,215°C,70% provide best outcomes.
- Compressive strength 2-4.11%
- 2-6% water absorption and thickness swelling ratio.
- Contact angle 75°, Porosity 44.5%.
- Cell viability 98% highest.

Figure 35: Overall framework fabrication to applications of wood-PLA lattice scaffold.

In this study, the lattice scaffold fabricated using the optimized DOE-27 parameter combination exhibited a compressive strength of 4.11 MPa, a contact angle of 75°, porosity of 44.57%, and controlled water absorption and thickness swelling in the range of 2–6%, along with high cell viability of up to 98%. These properties indicate that the developed scaffold possesses a favorable balance of mechanical strength, surface characteristics, structural porosity, and cytocompatibility.

Based on these findings, the proposed wood–PLA lattice scaffold is particularly suitable for non-load-bearing biomedical applications, where high mechanical strength is not the primary requirement. Potential applications include cancellous bone repair, maxillofacial and oral tissue engineering, and temporary biodegradable scaffolds that support tissue regeneration during the healing process. Although the obtained results demonstrate promising performance for non-load-bearing applications, the authors acknowledge that further studies are required to fully validate its suitability for bone tissue engineering. In particular, future work should include investigations using osteogenic cell lines and in vivo studies prior to clinical or bioimplantation applications. In **Figure 35**, an overall framework fabrication to applications of wood-PLA lattice scaffold is demonstrated. From both material and manufacturing perspectives, the developed scaffold also offers significant advantages, as the fabrication cost is less than USD 1, making it a highly cost-effective alternative compared to conventional bone graft materials.

4.4.6 Chapter summary

FDM-based 3D printing has gained significant popularity in recent years due to its versatility in applications and the use of diverse materials. Currently, there is a growing global demand for cost-effective materials that also offer enhanced structural and biological performance. This chapter also comprehensively investigated the effect of FDM printing parameters on the compressive behavior of wood–PLA composite lattice structures, with particular emphasis on compressive strength and compressive modulus. In addition, machine learning model was employed to enhance the prediction of stress–strain behavior and improve the accuracy of mechanical performance estimation. The manufacturing parameters have substantially impact on the mechanical, physical, and biological properties of the wood-PLA composite lattice scaffold. The materials developed and proposed in this chapter follow a systematic approach, encompassing fabrication, physical, mechanical, and physicochemical evaluations, along with cell viability studies. These findings will be benefited the future researchers, industries, in understanding the performance of sustainable wood-PLA composite lattice scaffolds, also applicable in particularly for non-load-bearing applications.

5.Future perspectives and limitations of the thesis

This research investigated the compressive behavior of different types of lattice structures, comparing the effectiveness of simple cubic (SC) PLA lattices and SC lattice wood–PLA composites fabricated using an FDM 3D printing process. The study experimentally analyzed various factors to enhance mechanical properties. Although artificial intelligence techniques were incorporated to optimize material performance, and advanced characterization methods such as scanning electron microscopy (SEM), analysis of variance (ANOVA), and in vitro testing were employed, several scientific gaps remain. These gaps provide opportunities for future research to further improve the mechanical performance, structural optimization, and material reliability of such lattice systems.

This research focused on the compressive behaviour of PLA, wood–PLA composite simple cubic lattice structures, particularly compressive strength and compressive modulus. However, porosity is also an important parameter that can significantly influence the mechanical properties of lattice structures. Therefore, future studies will investigate the influence of manufacturing parameters on the porosity of wood–PLA composite lattice structures and its relationship with mechanical performance.

In addition to porosity, future research could focus on the tensile, flexural, impact, and fatigue resistance, as well as the surface roughness of PLA and wood–PLA composites, particularly for lattice structures. Different machine learning approaches could also be applied to further improve the mechanical properties and overall performance of these structures.

This research only focused on XGBoost model prediction of compressive properties. However, future research could be conducted by considering other machine learning models and comparing them with existing literature to improve prediction efficacy and to better understand the compressive performance of different types of materials particularly for lattice structures.

Although suitable mechanical strength was achieved, the applicability of this lattice composite for specific engineering fields remains unclear. Future studies should identify potential real-life applications, including the types of loads and environments in which this material can be effectively utilized.

In addition, the sustainability aspects of the wood–PLA lattice composite were not examined. Important factors such as recyclability, renewability, and environmental im-pact require further investigation before the material can be proposed for large-scale commercial applications.

This study was limited to experimental analysis; however, future work could integrate numerical approaches such as finite element modeling to better predict failure mechanisms and improve lattice design.

Finally, only one machine learning model was employed in this research. Further improvements could be achieved by implementing advanced deep learning techniques to optimize configuration, enhance service life prediction, and provide industries with a clearer understanding of how different processing parameters affect mechanical properties.

In this study, the potential applications were proposed based on in vitro analysis and physical–mechanical properties. However, future research should include in vivo evaluations to further validate these findings.

6.Conclusions

This thesis investigates various aspects of lattice structures through statistical analysis and the incorporation of machine learning methods to predict compressive properties. The research is organized into three main stages of investigation and optimization. First, different lattice designs, filament types commonly used in FDM (Fused Deposition Modeling) printing, and strut diameters are analyzed and optimized. Second, the compressive behavior of PLA simple cubic (SC) lattice structures fabricated via FDM is examined. In this stage, manufacturing parameters are optimized and their effects on mechanical performance are evaluated. Additionally, a prototype bone scaffold is developed based on the optimized design. Finally, wood–PLA composite SC lattice structures are fabricated using FDM to evaluate their mechanical performance. This stage includes the investigation of compressive, physical, and biological properties. Machine learning techniques are further applied to enhance the prediction of compressive properties. The summary of the thesis is presented below:

- In terms of the FEM analysis, main effect plot analysis shows that all the considered responses (modulus of elasticity, effective strength and surface area) increase significantly with increase in strut diameter. Additionally, lattice types can provide different results. During ANOVA analysis it is also observed that strut diameter provides higher POC (E-39.84%, ES-46.80%, A-72.54%) and lower P-values (E-0.042, ES-0.066, A-0.021) in all outcomes. In addition, different materials and lattice structures may also provide different outcomes in considered results.

- Among these three filaments (PLA, ABS and Nylon), PLA exhibits better mechanical properties than ABS and Nylon. Furthermore, according to all-statistical analysis the order can be arranged as PLA>Nylon>ABS. Moreover, in terms of the lattice structures the SC-BCC type lattice shows better outcomes compared to FCC and SC. However, in terms of surface area SC lattice is more suitable which can be used to avoid the complexity during manufacturing.

- In terms of PLA SC lattice, the maximum modulus of elasticity and compressive strength is obtained with a combination of 0.1 mm layer height, 205 °C printing temperature, 50 mm/s printing speed, and 60 °C bed temperature. Moreover, the highest fracture strain percentage (60.06%) is found for 0.1 mm layer height, 200 °C printing temperature, 40 mm/s printing speed, and 55 °C bed temperature. However, the highest outcome of modulus of toughness (1104.53KJ/m3) is obtained for 0.1mm layer height, 210°C printing temperature, 60 mm/s printing speed, and 65°C bed temperature.

- ANOVA analysis reveals that for PLA SC lattice layer height is the most crucial parameter with a significant effect on modulus of elasticity and compressive strength with percentage contributions of 86.75% and 75.34%, respectively. Additionally, for fracture strain percentage and modulus of toughness, printing speed and printing temperature are the most influential parameters, with contribution percentages of 5.69% and 26.79%, respectively.

•ANOVA analysis for wood-PLA SC lattice revealed that layer height significantly influences both compressive strength and compressive modulus, with contribution percentages of 66.67% and 67.45%, respectively. Other parameters contributed less than 5% in both cases. Contour and 3D surface analyses demonstrated the interaction of layer height with other manufacturing parameters such as infill density, printing speed, and nozzle temperature. In most cases, lower layer height combined with moderate nozzle temperature, low printing speed, and low infill density resulted in improved compressive strength and modulus.

•For PLA SC lattice, the best manufacturing parameters, such as the layer height, printing temperature, printing speed, and bed temperature as 0.1 mm, 210°C, 30 mm/s, and 60°C, respectively, for the highest compressive strength. For, wood-PLA SC lattice, optimization results suggested that a layer height of 0.1 mm, nozzle temperature of 205°C, printing speed of 40 mm/s, and infill density of 70% provide favorable outcomes. However, the best results were obtained from DOE-27, which showed a 12.6% improvement in compressive strength. Additionally, the prediction accuracy between simulation and experimental validation was satisfactory, with only 1–3% deviation.

•For wood-PLA SC lattice, validation using unseen test specimens confirmed the ML algorithm's practical re-liability. The prediction error for compressive strength ranged between 2.14%–6.74%, while compressive modulus errors ranged between 1.82%–8.14%. These low discrepancies demonstrate that the tuned XGBoost model can reliably estimate both strength and stiffness directly from printing parameters.

•Contact angle, water absorption, and thickness swelling ratio analyses indicated that these properties are strongly influenced by manufacturing parameters, as they directly affect the scaffold surface characteristics of wood-PLA SC lattice. DOE-27 exhibited the best contact angle (75°) along with controlled water absorption and swelling behavior, making it suitable for biological environments, particularly in terms of protein adsorption, cell migration, and proliferation.

• For both PLA and wood–PLA lattice structures, Scanning Electron Microscopy (SEM) investigations were conducted to compare results across the design of experiments (DOE) and optimized conditions. The SEM analysis provided validation of the observed trends by revealing microstructural features such as manufacturing defects, surface quality, and deformation patterns.

•TR-146 cell evaluation demonstrated cell viability ranging from 85% to 98% across different concentration levels. All results exceeded the acceptable threshold of 70% for biomedical applications particularly in cancellous bone repair, maxillofacial and oral tissue engineering, and temporary biodegradable scaffolds.

Based on the obtained outcomes, this systematic analysis provides valuable insights into the effectiveness of manufacturing parameters, supports informed decision-making, enhances understanding of PLA, cellulose-based FDM materials, and enables the direct fabrication of optimized components for biological applications.

7.Thesis- new scientific innovation

T1. I investigate the compressive properties of various lattice structures by examining the effects of lattice design, filament type, and strut diameter through FEM method. These parameters are systematically analyzed to understand, optimize, and evaluate their influence on compressive behavior. FEM analysis produced satisfactory results, demonstrating strong agreement with experimental observations and capturing the interactions between key parameters. The developed FEM approach provides reliable validation and predictive capability, enabling the assessment of lattice performance without the need for extensive fabrication trials. This approach reduces experimental complexity and cost while offering valuable insights for future filament development and aiding researchers in decision-making, performance evaluation, and comparative analysis of lattice structures. From this investigations, I also found the best lattice structures among the considered is PLA and SC Lattice. (**Refference -1**)

T2. I identified that the compressive properties of PLA lattice structures are highly dependent on FDM manufacturing parameters. The interactions between these parameters and the compressive performance of PLA simple cubic (SC) lattices were systematically analyzed using the Taguchi method. The incorporation of this method enabled effective optimization, leading to enhanced mechanical properties. In addition, a prototype lattice scaffold was developed using SC PLA structures, specifically designed for bone-related applications. This scaffold can be utilized for implantation and educational purposes, particularly in fracture-related studies. The use of PLA is advantageous due to its biocompatibility and FDA approval for certain biomedical applications. **(Refference -2)**

T3. I investigated simple cubic (SC) lattice structures fabricated using wood–PLA filament via FDM and examined the influence of manufacturing parameters on their compressive properties. The selected parameters and corresponding outcomes were analyzed using the Response Surface Methodology (RSM), which demonstrated significant interactions and strong relevance in predicting mechanical performance. Furthermore, an artificial intelligence (AI)-based framework was developed to enhance the prediction process. The model achieved high prediction accuracy, demonstrating its effectiveness in capturing complex relationships between processing parameters and compressive behavior. This advanced approach provides a reliable tool for understanding and predicting the performance of such composite lattice materials. **(Refference -3)**

T4. An integrated validation approach was developed using Scanning Electron Microscopy (SEM) and microscopic analysis to explain the variations in mechanical properties. This approach enabled the identification of underlying reasons for both improvements and deterioration in the performance of lattice structures. Through detailed microstructural investigations, the relationship between manufacturing defects and mechanical behavior was systematically established. The findings provide clear evidence of how defects, surface characteristics, and structural integrity influence compressive performance. This validation framework offers valuable guidance for future researchers, helping them better understand the linkage between manufacturing-induced defects and the mechanical properties of lattice scaffolds. **(Refference -4 and 3)**

T5. Through a systematic investigation, I determined that manufacturing parameters significantly influence the physical properties of lattice structures, particularly for wood–PLA materials. Key properties such as contact angle, thickness swelling, and water absorption were found to be highly sensitive to processing conditions. Furthermore, the study demonstrated how and why these physical properties are closely linked to biomedical performance, especially in bone and tissue engineering applications. This relationship was established through a combination of comprehensive literature review and rigorous experimental validation, highlighting the importance of optimizing manufacturing parameters to achieve desirable functional and biological characteristics.(**Refference –4)**

T6. Based on the optimized outcomes of the wood–PLA lattice structures, a scaffold I designed for tissue engineering applications. The biological performance of the scaffold was evaluated using the TR146 cell line, where the results demonstrated that the optimized manufacturing parameters significantly enhanced cell viability, achieving approximately 98% compatibility after 7 days of exposure. Moreover, the estimated fabrication cost of the developed wood–PLA lattice scaffold is less than 1 USD, making it a highly cost-effective solution. This presents a promising alternative to conventional bone graft materials, particularly for non-load-bearing applications such as cancellous bone repair, maxillofacial and oral tissue engineering, and temporary biodegradable scaffolds. **(Refference -4)**

ACKNOWLEDGEMENTS

REFERENCES

[1] J. Sultana, S. Bin Rayhan, G. Varga, A scientometric review using CiteSpace : Progress , challenges , and applications of natural fiber-reinforced composite and hybrid composites in engineering applications (2015 – 2025), Results Eng. 28 (2025). https://doi.org/10.1016/j.rineng.2025.107670.

[2] D. Schuhmann, M. Rupp, M. Merkel, D.K. Harrison, Additive vs. Conventional Manufacturing of Metal Components: Selection of the Manufacturing Process Using the AHP Method, Processes. 10 (2022). https://doi.org/10.3390/pr10081617.

[3] M. Elbadawi, A. Basit, S. Gaisford, Energy consumption and carbon footprint of 3D printing in pharmaceutical manufacture, Int. J. Pharm. 639 (2023) 122926. https://doi.org/10.1016/j.ijpharm.2023.122926.

[4] D. Ling, D. Wang, P. Wang, X. Guo, L. Liu, B. He, L. Hu, G. Jiang, Life Cycle Assessment of 3D Printing for Precision Analytical Instrument Components: Carbon Emission Reduction Potential in ICP-MS Spray Chamber Manufacturing, ACS Sustain. Resour. Manag. 2 (2025) 1731–1741. https://doi.org/10.1021/acssusresmgt.5c00238.

[5] M.M. Rahman, S. Bin Rayhan, J. Sultana, M.Z. Rahman, Additive manufacturing techniques, their challenges, and additively manufactured composites for advanced engineering applications, 2nd ed., Elsevier Ltd., 2023. https://doi.org/10.1016/b978-0-323-96020-5.00118-7.

[6] A.H. Alami, A. Ghani Olabi, A. Alashkar, S. Alasad, H. Aljaghoub, H. Rezk, M.A. Abdelkareem, Additive manufacturing in the aerospace and automotive industries: Recent trends and role in achieving sustainable development goals, Ain Shams Eng. J. 14 (2023) 102516. https://doi.org/10.1016/j.asej.2023.102516.

[7] K. Kanishka, B. Acherjee, Revolutionizing manufacturing: A comprehensive overview of additive manufacturing processes, materials, developments, and challenges, J. Manuf. Process. 107 (2023) 574–619. https://doi.org/10.1016/j.jmapro.2023.10.024.

[8] M.M. Rahman, J. Sultana, S. Bin Rayhan, A. Ahmed, Optimization of FDM manufacturing parameters for the compressive behavior of cubic lattice cores: an experimental approach by Taguchi method, Int. J. Adv. Manuf. Technol. 129 (2023) 1329–1343. https://doi.org/10.1007/s00170-023-12342-9.

[9] G. veiw Reserach, U.S. Additive Manufacturing Market (2023 - 2030), 2022. https://www.grandviewresearch.com/industry-analysis/us-additive-manufacturing-market-report.

[10] P. Research, Additive Manufacturing Market Revenue, Top Companies, Report 2033, Preced. Res. (2022). https://www.precedenceresearch.com/press-release/additive-

manufacturing-market.

[11] GRAND VIEW RESEARCH, Healthcare Additive Manufacturing Market (2023 - 2030), (2022). https://www.grandviewresearch.com/industry-analysis/healthcare-additive-manufacturing-market.

[12] GRAND VIEW RESEARCH, U.S. Additive Manufacturing Market (2023 - 2030), (2022). https://www.grandviewresearch.com/industry-analysis/us-additive-manufacturing-market-report (accessed December 28, 2025).

[13] and M.M. Fares Mami, Jean-Pierre Rev´eret, Sophie Fallaha, Evaluating Eco-Efficiency of 3D Printing in the Aeronautic Industry, J. Ind. Ecol. 21 (2017). https://doi.org/DOI: 10.1111/jiec.12693.

[14] W. Zhang, X. Zhang, H.Y. Chong, J. Li, Carbon Emission Insights From a Real 3D Printed Bus Station, Adv. Civ. Eng. 2025 (2025). https://doi.org/10.1155/adce/6743618.

[15] S. Zakaria, P. Mativenga, A scientific base for optimising energy consumption and performance in 3D printing, J. Clean. Prod. 482 (2024) 144227. https://doi.org/10.1016/j.jclepro.2024.144227.

[16] C. Pan, Y. Han, J. Lu, Design and optimization of lattice structures: A review, Appl. Sci. 10 (2020) 1–36. https://doi.org/10.3390/APP10186374.

[17] S. Bin Rayhan, M.M. Rahman, J. Sultana, S. Szávai, G. Varga, Finite Element and Machine Learning-Based Prediction of Buckling Strength in Additively Manufactured Lattice Stiffened Panels, Metals (Basel). 15 (2025) 1–18. https://doi.org/10.3390/met15010081.

[18] D. Mahmoud, M.A. Elbestawi, Lattice structures and functionally graded materials applications in additive manufacturing of orthopedic implants: A review, J. Manuf. Mater. Process. 1 (2017) 1–19. https://doi.org/10.3390/jmmp1020013.

[19] M.A. El-Sayed, K. Essa, M. Ghazy, H. Hassanin, Design optimization of additively manufactured titanium lattice structures for biomedical implants, Int. J. Adv. Manuf. Technol. 110 (2020) 2257–2268. https://doi.org/10.1007/s00170-020-05982-8.

[20] Q. Shi, J. Chen, J. Chen, Y. Liu, H. Wang, Application of additively manufactured bone scaffold: a systematic review, Biofabrication. 16 (2024). https://doi.org/10.1088/1758-5090/ad35e8.

[21] N. Sultana, Mechanical and biological properties of scaffold materials, Elsevier Ltd, 2018. https://doi.org/10.1016/B978-0-08-100979-6.00001-X.

[22] S. Polo, A. García-Domínguez, E.M. Rubio, J. Claver, Lattice Structures in Additive Manufacturing for Biomedical Applications: A Systematic Review, Polymers (Basel). 17 (2025). https://doi.org/10.3390/polym17172285.

[23] X. Yue, J. Shang, M. Zhang, B. Hur, X. Ma, Additive manufacturing of high porosity magnesium scaffolds with lattice structure and random structure, Mater. Sci. Eng. A. 859 (2022) 144167. https://doi.org/10.1016/j.msea.2022.144167.

[24] J. Hulme, A.H. Sakhaei, M. Shafiee, Mechanical analysis and additive manufacturing of 3D-printed lattice materials for bone scaffolds, Procedia Struct. Integr. 63 (2024) 30–37. https://doi.org/10.1016/j.matpr.2023.02.278.

[25] B.I. Oladapo, S.O. Ismail, A. V. Adebiyi, F.T. Omigbodun, M.A. Olawumi, D.B.

Olawade, Nanostructural interface and strength of polymer composite scaffolds applied to intervertebral bone, Colloids Surfaces A Physicochem. Eng. Asp. 627 (2021) 127190. https://doi.org/10.1016/j.colsurfa.2021.127190.

[26] S. Murchio, M. Benedetti, A. Berto, F. Agostinacchio, G. Zappini, D. Maniglio, Hybrid Ti6Al4V/Silk Fibroin Composite for Load-Bearing Implants: A Hierarchical Multifunctional Cellular Scaffold, Materials (Basel). 15 (2022). https://doi.org/10.3390/ma15176156.

[27] M. Mahmoudi, M. Dargahi, S. Mashayekhan, R. Jahanmardi, H. Baniasadi, Structure–property–function relationships in 3D-printed gelatin/cellulose nanocrystals/n-HAP scaffolds for bone tissue repair, Int. J. Biol. Macromol. 328 (2025) 147790. https://doi.org/10.1016/j.ijbiomac.2025.147790.

[28] R. McMullan, A. Golbang, K. Salma-Ancane, J. Ward, K. Rodzen, A.R. Boyd, Review of 3D Printing of Polyaryletherketone/Apatite Composites for Lattice Structures for Orthopedic Implants, Appl. Sci. 15 (2025) 1–28. https://doi.org/10.3390/app15041804.

[29] K.K. Alaneme, S.A. Kareem, J.L. Olajide, R.E. Sadiku, M.O. Bodunrin, Computational biomechanical and biodegradation integrity assessment of Mg-based biomedical devices for cardiovascular and orthopedic applications: A review, Int. J. Light. Mater. Manuf. 5 (2022) 251–266. https://doi.org/10.1016/j.ijlmm.2022.02.003.

[30] Y. Wang, J. Sultana, M.M. Rahman, A. Ahmed, A. Azam, R.T. Mushtaq, M. Rehman, A Sustainable and Biodegradable Building Block: Review on Mechanical Properties of Bamboo Fibre Reinforced PLA Polymer Composites and Their Emerging Applications, Fibers Polym. 23 (2022) 3317–3342. https://doi.org/10.1007/s12221-022-4871-z.

[31] B.I. Oladapo, S.A. Zahedi, S.O. Ismail, F.T. Omigbodun, O.K. Bowoto, M.A. Olawumi, M.A. Muhammad, 3D printing of PEEK–cHAp scaffold for medical bone implant, Bio-Design Manuf. 4 (2021) 44–59. https://doi.org/10.1007/s42242-020-00098-0.

[32] W. Wang, L. Wang, B. Zhang, S. Shang, C. Zhao, W. Zhang, J. Chen, C. Zhou, H. Zhou, S. Feng, 3D printing of personalized magnesium composite bone tissue engineering scaffold for bone and angiogenesis regeneration, Chem. Eng. J. 484 (2024) 149444. https://doi.org/10.1016/j.cej.2024.149444.

[33] M. Mohammadi-Zerankeshi, R. Alizadeh, 3D-printed PLA-Gr-Mg composite scaffolds for bone tissue engineering applications, J. Mater. Res. Technol. 22 (2023) 2440–2446. https://doi.org/10.1016/j.jmrt.2022.12.108.

[34] H.Y. Kim, B.H. Kim, M.S. Kim, Amine Plasma-Polymerization of 3D Polycaprolactone/β-Tricalcium Phosphate Scaffold to Improving Osteogenic Differentiation In Vitro, Materials (Basel). 15 (2022). https://doi.org/10.3390/ma15010366.

[35] L. Gong, J. Li, J. Zhang, Z. Pan, Y. Liu, F. Zhou, An interleukin-4-loaded bi-layer 3D printed scaffold promotes osteochondral regeneration, Acta Biomater. 117 (2020) 246–260. https://doi.org/10.1016/j.actbio.2020.09.039.

[36] M.P. Bernardo, F. V Ferreira, L.F. Oliveira, L.H.C. Mattoso, J.H. Lopes, Revolutionizing bone regeneration : 3D printing of PLA / MFBG composites with advanced healing properties, Mater. Today Chem. 43 (2025).

[37] F. Alam, V.R. Shukla, K.M. Varadarajan, S. Kumar, Microarchitected 3D printed

polylactic acid (PLA) nanocomposite scaffolds for biomedical applications, J. Mech. Behav. Biomed. Mater. 103 (2020) 103576. https://doi.org/10.1016/j.jmbbm.2019.103576.

[38] S. Liu, Y. Zheng, Z. Wu, J. Hu, R. Liu, Preparation and characterization of aspirin-loaded polylactic acid/graphene oxide biomimetic nanofibrous scaffolds, Polymer (Guildf). 211 (2020) 123093. https://doi.org/10.1016/j.polymer.2020.123093.

[39] Q. Wei, G. Wang, M. Lei, Y. Guo, Y. Song, T. Lu, Y. Wang, Multi-scale investigation on the phase miscibility of polylactic acid/o-carboxymethyl chitosan blends, Polymer (Guildf). 176 (2019) 159–167. https://doi.org/10.1016/j.polymer.2019.05.030.

[40] D. Jiang, F. Ning, Y. Wang, Additive manufacturing of biodegradable iron-based particle reinforced polylactic acid composite scaffolds for tissue engineering, J. Mater. Process. Technol. 289 (2021) 116952. https://doi.org/10.1016/j.jmatprotec.2020.116952.

[41] Y. Wang, M. Lei, Q. Wei, Y. Wang, J. Zhang, Y. Guo, J. Saroia, 3D printing biocompatible l-Arg/GNPs/PLA nanocomposites with enhanced mechanical property and thermal stability, J. Mater. Sci. 55 (2020) 5064–5078.

[42] S. Sharma, Polylactic Acid (PLA) and Its Composites: An Eco-friendly Solution for Packaging, Sustain. Food Packag. Technol. (2021) 107–132.

[43] M.H. Kudzin, Z. Mrozińska, Biofunctionalization of Textile Materials. 2. Antimicrobial Modification of Poly (lactide)(PLA) Nonwoven Fabricsby Fosfomycin, Polymers (Basel). 12 (2020) 768.

[44] A.P. Morales, A. Güemes, A. Fernandez-Lopez, V.C. Valero, S. de La Rosa Llano, Bamboo-polylactic acid (PLA) composite material for structural applications, Materials (Basel). 10 (2017) 1–22. https://doi.org/10.3390/ma10111286.

[45] C. Ciofu, S.-N. Mazurchevici, D. Maldonado-Cortes, L. Pena-Paras, D.I.Q. Correa, D. Nedelcu, Tribological behavior of PLA biodegradable materials used in the automotive industry, Int. J. Mod. Manuf. Technol. 11 (2019) 83–88.

[46] N. Iqbal, A.S. Khan, A. Asif, M. Yar, J.W. Haycock, I.U. Rehman, Recent concepts in biodegradable polymers for tissue engineering paradigms: a critical review, Int. Mater. Rev. 64 (2019) 91–126. https://doi.org/10.1080/09506608.2018.1460943.

[47] M. Murariu, P. Dubois, PLA composites: From production to properties, Adv. Drug Deliv. Rev. 107 (2016) 17–46. https://doi.org/10.1016/j.addr.2016.04.003.

[48] C. Tang, J. Liu, Y. Yang, Y. Liu, S. Jiang, W. Hao, Effect of process parameters on mechanical properties of 3D printed PLA lattice structures, Compos. Part C Open Access. 3 (2020). https://doi.org/10.1016/j.jcomc.2020.100076.

[49] V. Tuninetti, S. Narayan, I. Ríos, B. Menacer, R. Valle, M. Al-lehaibi, M.U. Kaisan, J. Samuel, A. Oñate, G. Pincheira, A. Mertens, Lattice Structures Design and Manufacturing for High Stress , Deformation , and Energy Absorption Performance, Biomimetic. 10 (2025) 1–37.

[50] C. Peng, P. Tran, H. Nguyen-Xuan, A.J.M. Ferreira, Mechanical performance and fatigue life prediction of lattice structures: Parametric computational approach, Compos. Struct. 235 (2020) 111821. https://doi.org/10.1016/j.compstruct.2019.111821.

[51] S. Paul, Finite element analysis in fused deposition modeling research: A literature

review, Meas. J. Int. Meas. Confed. 178 (2021) 109320. https://doi.org/10.1016/j.measurement.2021.109320.

[52] R. Alkentar, F. Máté, T. Mankovits, Investigation of the Performance of Ti6Al4V Lattice Structures Designed for Biomedical Implants Using the Finite Element Method, Materials (Basel). 15 (2022). https://doi.org/10.3390/ma15186335.

[53] N. Sakthivel, J. Bramsch, P. Voung, I. Swink, S. Averick, H.D. Vora, Investigation of 3D-printed PLA – stainless-steel polymeric composite through fused deposition modelling-based additive manufacturing process for biomedical applications, Med. Devices Sensors. (2020) 1–21. https://doi.org/10.1002/mds3.10080.

[54] P.V. Kumar, A. Kumar, B. Nelson, Multi - response optimization of FDM parameters for high - performance PLA / MgTiO 3 TPMS gyroid scaffolds : a Taguchi - based VIKOR – TOPSIS approach for biomedical applications, Prog. Addit. Manuf. 10 (2025) 8445–8463. https://doi.org/10.1007/s40964-025-01130-4.

[55] F. Alam, P. Verma, W. Mohammad, J. Teo, K.M. Varadarajan, Architected poly (lactic acid)/ poly (e -caprolactone)/ halloysite nanotube composite scaffolds enabled by 3D printing for biomedical applications, J. Mater. Sci. 56 (2021) 14070–14083. https://doi.org/10.1007/s10853-021-06145-0.

[56] S. Li, T. Wang, S. Chen, Y. Li, Y. Zou, B. Cao, J. Hu, X. Tan, B. Wang, Thin-Walled Structures Compressive properties and biocompatibility of additively manufactured lattice structures by using bioactive materials, Thin-Walled Struct. 205 (2024) 112469. https://doi.org/10.1016/j.tws.2024.112469.

[57] B.I. Oladapo, J.F. Kayode, P. Karagiannidis, N. Naveed, H. Mehrabi, K.O. Ogundipe, S. Development, Polymeric composites of cubic-octahedron and gyroid lattice for biomimetic dental implants, Mater. Chem. Phys. 289 (2022) 126454. https://doi.org/10.1016/j.matchemphys.2022.126454.

[58] M. Bolan, M. Dean, A. Bardelcik, The Energy Absorption Behavior of 3D-Printed Polymeric Octet-Truss Lattice Structures of Varying Strut Length and Radius, Polymers (Basel). 15 (2023).

[59] X. Yang, Q. Yang, Y. Shi, L. Yang, S. Wu, C. Yan, Y. Shi, Effect of volume fraction and unit cell size on manufacturability and compressive behaviors of Ni-Ti triply periodic minimal surface lattices, Addit. Manuf. 54 (2022) 102737. https://doi.org/10.1016/j.addma.2022.102737.

[60] S. Bin Rayhan, M. Rahman, Effect of micromechanical properties on the critical buckling load of woven composite plate : A multiscale analysis, Procedia Struct. Integr. 28 (2020) 1901–1908. https://doi.org/10.1016/j.prostr.2020.11.013.

[61] K.M.F. Hasan, M.M. Rahman, F.K. Rima, J. Sultana, M.A. Taher, P.G. Horváth, J. Garab, L. Bejó, T. Alpár, Sustainable prospects of lignocellulosic wood and natural fiber-based materials in 3D and 4D printing, Adv. Compos. Hybrid Mater. 8 (2025) 189. https://doi.org/10.1007/s42114-025-01273-6.

[62] M.M.A. Nassar, R. Arunachalam, K.I. Alzebdeh, Machinability of natural fiber reinforced composites : a review, Int. J. Adv. Manuf. Technol. 88 (2017) 2985–3004. https://doi.org/10.1007/s00170-016-9010-9.

[63] H. Cheung, M. Ho, K. Lau, F. Cardona, D. Hui, Natural fibre-reinforced composites for bioengineering and environmental engineering applications, Compos. Part B. 40 (2009) 655–663. https://doi.org/10.1016/j.compositesb.2009.04.014.

[64] J. Rojas, M. Bedoya, Y. Ciro, Current Trends in the Production of Cellulose Nanoparticles and Nanocomposites for Biomedical Applications, Cellul. - Fundam. Asp. Curr. Trends. (2015) 194–228. https://doi.org/http://dx.doi.org/10.5772/61334.

[65] F. Luzi, D. Puglia, L. Torre, Natural fiber biodegradable composites and nanocomposites: A biomedical application, Elsevier Ltd, 2019. https://doi.org/10.1016/B978-0-08-102426-3.00010-2.

[66] K. Markstedt, A. Mantas, I. Tournier, D. Ha, P. Gatenholm, 3D Bioprinting Human Chondrocytes with Nanocellulose − Alginate Bioink for Cartilage Tissue Engineering Applications, Biomacromolecules. 16 (2015) 1489−1496. https://doi.org/10.1021/acs.biomac.5b00188.

[67] E. Diabor, P. Funkenbusch, E.E. Kaufmann, Characterization of Cassava Fiber of Different Genotypes as a Potential Reinforcement Biomaterial for Possible Tissue Engineering Composite Scaffold Application, Fibers Polym. 20 (2019) 217–228. https://doi.org/10.1007/s12221-019-8702-9.

[68] J.G. Torres-rendon, T. Femmer, L. De Laporte, T. Tigges, K. Rahimi, F. Gremse, S. Zafarnia, W. Lederle, S. Ifuku, M. Wessling, J.G. Hardy, A. Walther, Bioactive Gyroid Scaffolds Formed by Sacrificial Templating of Nanocellulose and Nanochitin Hydrogels as Instructive Platforms for Biomimetic Tissue Engineering, Adv. Mater. (2015) 2989–2995. https://doi.org/10.1002/adma.201405873.

[69] A. Cernencu, L. Balahura, S. Dinescu, M. Balas, G. Mihail, H. Iovu, M. Costache, Cellulose Nanofiber-Based Hydrogels Embedding 5-FU Promote Pyroptosis Activation in Breast Cancer Cells and Support Human Adipose-Derived Stem Cell Proliferation , Opening New Perspectives for Breast Tissue Engineering, Pharm. Res. 13 (2021).

[70] D.M. Catori, E.H. Fragal, I. Messias, F.P. Garcia, C. V Nakamura, A.F. Rubira, Development of composite hydrogel based on hydroxyapatite mineralization over pectin reinforced with cellulose nanocrystal, Int. J. Biol. Macromol. 167 (2021) 726–735. https://doi.org/10.1016/j.ijbiomac.2020.12.012.

[71] R. Goyal, S. Nikhilesh, R. Yadav, S. Mitra, A. Samanta, A. Kumar, B. Lochab, 3D printed cellulose nanofiber-reinforced and iron-crosslinked double network hydrogel composites for tissue engineering applications : Mechanical properties and cellular viability, Bioprinting. 46 (2025) e00392. https://doi.org/10.1016/j.bprint.2025.e00392.

[72] R. Chen, C. Huang, S. Hsu, Composites of waterborne polyurethane and cellulose nanofibers for 3D printing and bioapplications, Carbohydr. Polym. 212 (2019) 75–88. https://doi.org/10.1016/j.carbpol.2019.02.025.

[73] M. M. Kanjou, H. Abdulhakim, G.M. de Olyveira, P. Basmaji, 3-D Print Celulose Nanoskin: Future Diabetic Wound Healing, J. Biomater. Nanobiotechnol. 10 (2019) 190–195. https://doi.org/10.4236/jbnb.2019.104011.

[74] L. Kothandaraman, N.K. Balasubramanian, Optimization of FDM printing parameters for square lattice structures : Improving mechanical characteristics, Mater. Today Proc.

(2024). https://doi.org/10.1016/j.matpr.2024.04.033.

[75] J.R. Stojkovi, An Experimental Study on the Impact of Layer Height and Annealing Parameters on the Tensile Strength and Dimensional Accuracy of FDM 3D Printed Parts, Materials (Basel). 16 (2023).

[76] N. Dixit, P.K. Jain, Effect of Fused Filament Fabrication Process Parameters on Compressive Strength of Thermoplastic Polyurethane and Polylactic Acid Lattice Structures, J. Mater. Eng. Perform. 31 (2022) 5973–5982. https://doi.org/10.1007/s11665-022-06664-0.

[77] C. Tang, J. Liu, Y. Yang, Y. Liu, S. Jiang, W. Hao, Effect of process parameters on mechanical properties of 3D printed PLA lattice structures, Compos. Part C Open Access. 3 (2020). https://doi.org/10.1016/j.jcomc.2020.100076.

[78] M.K. Poddar, R. Kumar, S.K. Sarangi, Optimizing FDM 3D printing parameters for enhanced compressive strength in PLA fluorite lattice structures : a Taguchi design and finite element analysis approach Optimizing FDM 3D printing parameters for enhanced compressive strength in PLA fluorite latt, Eng. Res. Express. 7 (2025).

[79] H. Bakhtiari, A. Nouri, M. Tolouei-rad, Impact of 3D printing parameters on static and fatigue properties of polylactic acid (PLA) bone scaffolds, Int. J. Fatigue. 186 (2024) 108420. https://doi.org/10.1016/j.ijfatigue.2024.108420.

[80] Q. Tanveer, G. Mishra, S. Mishra, R. Sharma, Effect of infill pattern and infill density on mechanical behaviour of FDM 3D printed Parts- a current review, Mater. Today Proc. 62 (2022) 100–108. https://doi.org/10.1016/j.matpr.2022.02.310.

[81] S. Garg, A. Singh, Q. Murtaza, Measuring the Impact of Infill Pattern and Infill Density on the Properties of 3D-Printed PLA via FDM, J. Mater. Eng. Perform. 34 (2025) 22597–22610. https://doi.org/10.1007/s11665-025-10837-y.

[82] Q. Ma, M.R.M. Rejab, A.P. Kumar, H. Fu, N.M. Kumar, J. Tang, Effect of infill pattern , density and material type of 3D printed cubic structure under quasi-static loading, J. Mech. Eng. Sci. 235 (2020). https://doi.org/10.1177/0954406220971667.

[83] S. Perween, M. Fahad, M.A. Khan, Systematic experimental evaluation of function based cellular lattice structure manufactured by 3d printing, Appl. Sci. 11 (2021). https://doi.org/10.3390/app112110489.

[84] T.C. Yang, C.H. Yeh, Morphology and mechanical properties of 3D printed wood fiber/polylactic acid composite parts using Fused Deposition Modeling (FDM): The effects of printing speed, Polymers (Basel). 12 (2020) 1334. https://doi.org/10.3390/POLYM12061334.

[85] H. Ye, Z. Zhang, Study on Effects of FDM 3D Printing Parameters on Mechanical Properties of Polylactic Acid Study on Effects of FDM 3D Printing Parameters on Mechanical Properties of Polylactic Acid, in: IOP Conf. Ser. Mater. Sci. Eng., 2019: p. 033026. https://doi.org/10.1088/1757-899X/688/3/033026.

[86] O. Tunçel, Optimizing printing parameters for enhanced mechanical properties of 3D printed PLA octet lattice structures, Eur. Mech. Sci. 7 (2023) 278–284.

[87] I. Mahapatra, N. Chikkanna, K. Shanmugam, Evaluation of tensile properties of 3D-printed lattice composites : Experimental and machine learning-based predictive

modelling ☆, Compos. Part A. 193 (2025) 108823. https://doi.org/10.1016/j.compositesa.2025.108823.

[88] C. Fetecau, F. Stan, D. Boazu, Artificial Neural Network Modeling of Mechanical Properties of 3D-Printed Polyamide 12 and Its Fiber-Reinforced Composites, Polymers (Basel). 17 (2025) 1–28. https://doi.org/https://doi.org/10.3390/polym17050677.

[89] P. Anerao, A. Kulkarni, Y. Munde, N. Kharate, A Comparative Study of Machine Learning Techniques for Predicting Mechanical Properties of Fused Deposition Modelling (FDM) -Based 3D-Printed Wood / PLA Biocomposite, Mech. Adv. Compos. Struct. 12 (2025) 261–270.

[90] K. Vijayananth, G. Pudhupalayam, A. Raju, Integrated optimization and prediction of mechanical properties in FDM printed polyamide / carbon fiber composites using PSI – VIKOR and ANN, Next Mater. 8 (2025) 100932. https://doi.org/10.1016/j.nxmate.2025.100932.

[91] S. Hussain, C. Ka, M. Lee, Y.P. Tsang, S. Waqar, A machine learning-based recommendation framework for material extrusion fabricated triply periodic minimal surface lattice structures, J. Mater. Sci. Mater. Eng. 20 (2025) 1–20. https://doi.org/10.1186/s40712-025-00229-4.

[92] M.J. Hooshmand, C. Sakib-Uz-Zaman, M.A.H. Khondoker, Machine Learning Algorithms for Predicting Mechanical Stiffness of Lattice Structure-Based Polymer Foam, Materials (Basel). 16 (2023) 1–19. https://doi.org/10.3390/ma16227173.

[93] F.T. Omigbodun, B.I. Oladapo, AI-Optimized Lattice Structures for Biomechanics Scaffold Design, Biomimetics. 10 (2025) 1–19.

[94] S. Liu, S. Qin, M. He, D. Zhou, Q. Qin, H. Wang, Current applications of poly (lactic acid) composites in tissue engineering and drug delivery, Compos. Part B. 199 (2020) 108238. https://doi.org/10.1016/j.compositesb.2020.108238.

[95] R. Fajarani, E. Septia, Y. Siti, H. Yudan, S.F. Rahman, Development of King Cobia Collagen / hydroxypropyl Methylcellulose / polyvinyl Alcohol-Based Carbon Scaffolds for Potential Bone Tissue Engineering Applications, J. Polym. Environ. 33 (2025) 4526–4545.

[96] A. Abusabir, M.A. Khan, M. Asif, K.A. Khan, Effect of Architected Structural Members on the Viscoelastic Response of 3D Printed Simple Cubic Lattice Structures, Polymers (Basel). 14 (2022). https://doi.org/10.3390/polym14030618.

[97] A.K. Mishra, H. Chavan, A. Kumar, Effect of material variation on the uniaxial compression behavior of FDM manufactured polymeric TPMS lattice materials, Mater. Today Proc. 46 (2021) 7752–7759. https://doi.org/10.1016/j.matpr.2021.02.276.

[98] K. Monkova, P.P. Monka, O. Šuba, M. Žaludek, D. Kozak, J. Vanca, Influence of the material volume of a lattice structure on bending properties, MATEC Web Conf. 349 (2021) 04003. https://doi.org/10.1051/matecconf/202134904003.

[99] M. Kaur, T.G. Yun, S.M. Han, E.L. Thomas, W.S. Kim, 3D printed stretching-dominated micro-trusses, Mater. Des. 134 (2017) 272–280. https://doi.org/10.1016/j.matdes.2017.08.061.

[100] T.A. Alwattar, A. Mian, Development of an elastic material model for bcc lattice cell

structures using finite element analysis and neural networks approaches, J. Compos. Sci. 3 (2019). https://doi.org/10.3390/jcs3020033.

[101] N. Jin, F. Wang, Y. Wang, B. Zhang, H. Cheng, H. Zhang, Effect of structural parameters on mechanical properties of Pyramidal Kagome lattice material under impact loading, Int. J. Impact Eng. 132 (2019). https://doi.org/10.1016/j.ijimpeng.2019.06.002.

[102] M.R. Karamooz Ravari, M. Kadkhodaei, M. Badrossamay, R. Rezaei, Numerical investigation on mechanical properties of cellular lattice structures fabricated by fused deposition modeling, Int. J. Mech. Sci. 88 (2014) 154–161. https://doi.org/10.1016/j.ijmecsci.2014.08.009.

[103] R.A. Hamid, F.H. Hamezah, J. Abd Razak, Influence of Humidity on the Tensile Strength of 3D Printed PLA Filament, Springer Singapore, 2022. https://doi.org/10.1007/978-981-16-8954-3_47.

[104] M. Algarni, The influence of raster angle and moisture content on the mechanical properties of pla parts produced by fused deposition modeling, Polymers (Basel). 13 (2021) 1–12. https://doi.org/10.3390/polym13020237.

[105] R.G. Silva, C.S. Estay, G.M. Pavez, J.Z. Viñuela, M.J. Torres, Influence of geometric and manufacturing parameters on the compressive behavior of 3d printed polymer lattice structures, Materials (Basel). 14 (2021). https://doi.org/10.3390/ma14061462.

[106] Qidi, Qidi-PLA wood filament, (n.d.). https://eu.qidi3d.com/products/pla-wood-filament (accessed February 11, 2026).

[107] M. Kariz, M. Sernek, M.K. Kuzman, E ffect of wood content in FDM fi lament on properties of 3D printed parts, Mater. Today. 14 (2018) 135–140. https://doi.org/10.1016/j.mtcomm.2017.12.016.

[108] M.K. Poddar, R. Kumar, S.K. Sarangi, Optimizing FDM 3D printing parameters for enhanced compressive strength in PLA fluorite lattice structures : a Taguchi design and finite element analysis approach, Eng. Res. Express. 7 (2025) 045556.

[109] C. Tang, J. Liu, Y. Yang, Y. Liu, S. Jiang, W. Hao, Effect of process parameters on mechanical properties of 3D printed PLA lattice structures, Compos. Part C Open Access. 3 (2020) 1–14. https://doi.org/10.1016/j.jcomc.2020.100076.

[110] P. Lohmuller, J. Favre, P. Laheurte, Stress Concentration and Mechanical Strength of Cubic Lattice Architectures, Materials (Basel). 11 (2018) 1–12. https://doi.org/10.3390/ma11071146.

[111] K. Park, K. Min, Y. Roh, Design Optimization of Lattice Structures under Compression : Study of Unit Cell Types and Cell Arrangements, Materials (Basel). 15 (2022). https://doi.org/https://doi.org/10.3390/ma15010097.

[112] V. Mahesh, ANN based prediction of the absorption characteristics of additive manufactured glycol-modified polyethylene terephthalate nanocomposites reinforced with short-carbon fibers and nanoclay fillers, Polym. Compos. 44 (2023) 8223–8239. https://doi.org/10.1002/pc.27337.

[113] M.A. Alsmael, S.W. Ibrahim, M.H.M. Alsharbaty, S.S. Ali, M. Schagerl, Enhanced Mechanical and Surface Performance of Three-Dimensionally Printed Denture Base Resin via Zinc Oxide and Samarium Oxide Nanoparticle Reinforcement, Materials (Basel). 19

(2026) 1–25.

[114] G. Repetto, A. Peso, J.L. Zurita, Neutral red uptake assay for the estimation of cell viability / cytotoxicity, Nature. 3 (2008) 1125–1131. https://doi.org/10.1038/nprot.2008.75.

[115] Ensemble learning, (2026). https://www.academia.edu/2813351/Ensemble_learning (accessed January 9, 2026).

[116] T. Chen, T. He, XGBoost: A Scalable Tree Boosting System, in: Proc. 22nd ACM SIGKDD Int. Conf. Knowl. Discov. Data Min., San Francisco California,USA Aug 2016, 2022: pp. 785–794. https://doi.org/10.1145/2939672.2939785.

[117] F.F. lee Bryan clark, What is Gradient Boosting?, IBM. (n.d.). https://www.ibm.com/think/topics/gradient-boosting (accessed February 9, 2026).

[118] B.D.M. Marc Claesen, Hyperparameter Search in Machine Learning, (2016). https://doi.org/doi: 10.48550/arXiv.1502.02127.

[119] H.Z. Tong Yu, Hyper-Parameter Optimization: A Review of Algorithms and Applications, ArXiv:2003.05689. (n.d.). https://doi.org/https://doi.org/10.48550/arXiv.2003.05689.

[120] J. Bergstra, Y. Bengio, Random Search for Hyper-Parameter Optimization, J. Mach. Learn. Res. 13 (2012) 281–305.

[121] S. Pan, Z. Guan, G. Yao, J. Yuan, X. Li, Mo-enhanced chemical stability of TiC nanoparticles in molten Al, J. Alloys Compd. 856 (2021). https://doi.org/10.1016/j.jallcom.2020.158169.

[122] J. Sultana, M.M. Rahman, Y. Wang, A. Ahmed, C. Xiaohu, Influences of 3D printing parameters on the mechanical properties of wood PLA filament: an experimental analysis by Taguchi method, Prog. Addit. Manuf. 9 (2023) 1239–1251. https://doi.org/10.1007/s40964-023-00516-6.

[123] Q.C. Johnson, C.M. Laursen, A.D. Spear, J.D. Carroll, J. Noell, Materials Science & Engineering A Analysis of the interdependent relationship between porosity , deformation , and crack growth during compression loading of LPBF AlSi10Mg, Mater. Sci. Eng. A. 852 (2022) 143640. https://doi.org/10.1016/j.msea.2022.143640.

[124] S. Pan, J. Yuan, K. Jin, N. Murali, A. Gladstein, Y. Zeng, A. Taub, X. Li, A. Si, Materials Science & Engineering A Influence of Mg on reaction and properties of Al – Si / TiC nanocomposites, Mater. Sci. Eng. A. 840 (2022) 142992. https://doi.org/10.1016/j.msea.2022.142992.

[125] M.H. Hsueh, C.J. Lai, S.H. Wang, Y.S. Zeng, C.H. Hsieh, C.Y. Pan, W.C. Huang, Effect of printing parameters on the thermal and mechanical properties of 3d-printed pla and petg, using fused deposition modeling, Polymers (Basel). 13 (2021). https://doi.org/10.3390/polym13111758.

[126] P. Properties, U. Wood, T. Yang, Effect of Extrusion Temperature on the Fiber-Reinforced Polylactic Acid Composite (WFRPC), Polymers (Basel). 10 (2018). https://doi.org/10.3390/polym10090976.

[127] A. Milovanovi, Influence of Infill Density on the Fatigue Performance of FDM-Manufactured Orthopaedic Plates, Materials (Basel). 19 (2026) 1–20.

https://doi.org/https://doi.org/10.3390/ma19040816.

[128] B. Yao, Q. Zhu, L. Yao, J. Hao, Applied Surface ScienceFabrication of honeycomb-structured poly (ethylene glycol) -block-poly (lactic acid) porous films and biomedical applications for cell growth, Appl. Surf. Sci. 332 (2015) 287–294. https://doi.org/10.1016/j.apsusc.2015.01.170.

[129] G.A. Hutcheon, C. Messiou, R.M. Wyre, M.C. Davies, S. Downes, Water absorption and surface properties of novel poly (ethylmethacrylate) polymer systems for use in bone and cartilage repair, Biomaterials. 22 (2001) 667–676.

[130] K.J. Susanna, Acidic Hydrolytic Stability of the Lifitegrast : Degradation , Method Development , Validation , Synthesis , LC – MS / NMR Characterization , In Silico and In Vitro Cytotoxicity, Seperation Sci. Plus. 9 (2025). https://doi.org/https://doi.org/10.1002/sscp.70189 1of13.

[131] J. Zhang, W. Zhang, W. Yue, W. Qin, Y. Zhao, G. Xu, Research Progress of Bone Grafting : A Comprehensive Review, Int. Jouranl Nanomedicine. 20 (2025). https://doi.org/https://doi.org/10.2147/IJN.S510524.

[132] S.S. Anuj Dadhich, Kumar Nilesh, H. Saluja, Three - dimensional printing in maxillofacial surgery : A quantum leap in future, Case Rep. 13 (2022) 203–211. https://doi.org/10.4103/njms.NJMS.

LIST OF PUBLICATIONS RELATED TO THE TOPIC OF THE RESEARCH FIELD

(1)**M. M. Rahman** and J. Sultana, "Numerical and Statistical Analysis on Polymeric Lattice Structures via Taghuchi Method," 2023 International Conference on Engineering, Science and Advanced Technology (ICESAT), Mosul, Iraq, 2023, pp. 210-214, doi: 10.1109/ICESAT58213.2023.10347288.

(2) Rahman, M.M., Sultana, J., Rayhan, S.B. et al. Optimization of FDM manufacturing parameters for the compressive behavior of cubic lattice cores: an experimental approach by Taguchi method. Int J Adv Manuf Technol 129, 1329–1343 (2023). https://doi.org/10.1007/s00170-023-12342-9**.**

(3) Rahman MM, Israq MA, Szávai S, Bin Rayhan S, Varga G. Experimental Characterization and a Machine Learning Framework for FDM-Fabricated Biocomposite Lattice Structures. *Fibers*. 2026; 14(4):41. https://doi.org/10.3390/fib14040041.

(4) Rahman MM, Szávai S, Bin Rayhan S,Effect of Manufacturing Parameters on FDM-Printed Wood–PLA Lattice Composites scaffold: An In Vitro and Statistical Analysis for tissue engineering applications. (Submitted, Journal: Additive manufacturing)

(5) Rahman MM, Szávai S, Bin Rayhan, A current progress and application of composite and hybrid composite lattice scaffold in biomedical industries. (Submitted, Journal: Advanced composite and hybrid materials)

(6) Rahman, Md Mazedur, Saiaf Bin Rayhan, Jakiya Sultana, and Md Zillur Rahman. "Additive manufacturing techniques, their challenges, and additively manufactured composites for advanced engineering applications." (2024): 329-351DOI: 10.1016/B978-0-323-96020-5.00118-7.

(7) Rahman, M.M., Sultana, J., Rayhan, S.B., Rahman, M.Z.: Recent advances in nanomaterials, nanocomposite and nanohybrids for biomedical and biosensing applications. In: Comprehensive Materials Processing, 2nd edn. (2024). Elsevier. https://doi.org/10.1016/B978-0-323-96020-5.00119-9.

(8) Rahman, Md Mazedur, and Szávai Szabolcs. “Critical Buckling and Damage Analysis of Hybrid Composite Panels with Cutouts under Uniaxial Compression Loading.” Advances in Science and Technology. Trans Tech Publications Ltd, June 4, 2025. https://doi.org/10.4028/p-nji72q.

(9) M. M. Rahman and J. Sultana, "Design and Optimization of Natural Fiber Reinforced Hybrid Composite RVE: A Finite Element Analysis," 2023 International Conference on Engineering, Science and Advanced Technology (ICESAT), Mosul, Iraq, 2023, pp. 204-209, doi: 10.1109/ICESAT58213.2023.10347323.

(10) Sultana, J**., Rahman, M.M**., Wang, Y. et al. Influences of 3D printing parameters on the mechanical properties of wood PLA filament: an experimental analysis by Taguchi method. Prog Addit Manuf 9, 1239–1251 (2024). https://doi.org/10.1007/s40964-023-00516-6.

(11) K.M. Farid, **Rahman, M.M.**, Rima, F.K. et al. Sustainable prospects of lignocellulosic wood and natural fiber-based materials in 3D and 4D printing. Adv Compos Hybrid Mater 8, 189 (2025). https://doi.org/10.1007/s42114-025-01273-6.

(12) Khan, S., Rayhan, S. B., **Rahman, M. M.**, Sultana, J., & Varga, G. (2025). Optimized ANN Model for Predicting Buckling Strength of Metallic Aerospace Panels Under Compressive Loading. Metals, 15(6), 666. https://doi.org/10.3390/met15060666.

(13) S.B. Rayhan, C.J. Yu, **M.M. Rahman**, P. Xue Advances and future challenges in aircraft fuselage section crashworthiness: a critical review, Recent Pat. Mech. Eng., 16 (5) (2023), pp. 309-320. 10.2174/2212797616666230905161308.

(14) Rayhan SB, **Rahman MM**, Sultana J, Szávai S, Varga G. Finite Element and Machine Learning-Based Prediction of Buckling Strength in Additively Manufactured Lattice Stiffened Panels. Metals. 2025; 15(1):81. https://doi.org/10.3390/me